HVI-induced stress field and vibrations

Analysis by SPH-FEM coupled numerical method

Master degree in Aerospace Engineering

Lorenzo Esposito

Delft University of Technology

TU Delft

HVI-induced stress field and vibrations

Analysis by SPH-FEM coupled numerical method

by

Lorenzo Esposito

to obtain the degree of Master of Science
at the Delft University of Technology,
to be defended publicly on Thursday June 20, 2024 at 2:00 PM.

Student number:	5593921		
Project duration:	September, 2023 – April, 2024		
Thesis supervisors:	Prof. S.R. Turteltaub,	TU Delft,	Supervisor
	Prof. C. Bisagni,	TU Delft - Politecnico di Milano,	Co-supervisor
	Ing. T. Cardone,	TU Delft - European Space Agency,	Co-supervisor
Thesis committee:	Prof. R. Groves	TU Delft,	Chair
	Prof. D. Peeters	TU Delft,	Examiner
	Prof. S.R. Turteltaub,	TU Delft,	Supervisor
	Prof. C. Bisagni,	TU Delft - Politecnico di Milano,	Co-supervisor
	Ing. T. Cardone,	TU Delft - European Space Agency,	Co-supervisor

Cover: Space debris. Credit: European Space Agency

TU Delft

Abstract

Hyper-Velocity Impacts (HVI) from micrometeoroids and orbital debris pose a significant threat to satellites in low Earth orbit due to the higher density of sources and the resulting increased impact frequency. Understanding the stress field and dynamic behavior around impact points is critical for satellite design, structural integrity, and platform stability assessment. A coupled Finite Element and Smoothed Particle Hydrodynamics (SPH) methodology implemented in LS-DYNA explicit software is used to simulate HVI effects. Without compromising the reliability of the results and ensuring their continuity at the methodological interface, the aim is to take advantage of the strengths of both simulation methods. Although previous studies have used SPH-FEM coupling to model Hyper-Velocity Impacts, the focus of this thesis is on characterizing the stress field surrounding the impact zone. It has been observed that a portion of the stress wave is reflected at the interface between the two numerical methods within the plate. This reflection is not caused by a physical obstacle and is therefore numerical and artificial. A comparative analysis of stress signals collected near this numerical modeling discontinuity demonstrated that the implementation of a SPH-FEM hybrid elements interface exhibited superior performance in mitigating this effect in comparison with a tied type contact. Indeed, stress waves can smoothly move from the impacted region towards the external domain of the structure, exhibiting only minor internal reflection at the interface between the two numerical methodologies. Furthermore, the impact of the SPH lattice on stress wave propagation was explored. It was found that the default modeling approach had a detrimental effect on uniform stress propagation in the plate, as it introduced preferential directions of propagation. This issue was addressed by implementing a custom SPH lattice that ensures the isotropic properties of the material selected for modeling the plate. The propagation of impact-induced effects is ensured to be independent of the direction of study. Initial calibration and validation were conducted on a single flat plate system, followed by an extension to a full Whipple shield simulation. With regard to the latter, not only stress data, but also the HVI-induced vibration field within the plates was studied. This was achieved by collecting the out-of-plane velocity signal at variable distances from the impact site. Nevertheless, further studies are necessary for further refinement and validation.

Keywords: Hyper-Velocity Impacts, Smoothed Particle Hydrodynamics, Coupling SPH-FEM, Spacecraft Stability, Space Debris

Contents

List of Figures

List of Tables

Nomenclature

Abbreviations

Abbreviation	Definition
ALE	**A**rbitrary **L**agrangian-**E**ulerian
AV	**A**rtificial **V**iscosity
CEG	**C**entre d'**É**tudes de **G**ramat
CFRP	**C**arbon **F**iber **R**einforced **P**lastic
CPEM	**C**orrective **S**moothed **P**article **H**ydrodynamics
CSPH	**A**rtificial **V**iscosity
CST	**C**ollision **S**imulation **T**ool
EFG	**E**lement-**F**ree **G**alerkin
EMI	**E**rnst **M**ach **I**nstitute
EOS	**E**quation **o**f **S**tate
ESA	**E**uropean **S**pace **A**gency
FASTT	**F**ragmentation **A**lgorithms for **S**trategic and **T**heater **T**argets
FEM	**F**inite **E**lement **M**ethod
GAIA	**G**lobal **A**strometric **I**nterferometer for **A**strophysics
GOGE	**G**ravity field and steady-state **O**cean **C**irculation **E**xplorer
HPC	**H**igh **P**erformance **C**omputing
HVI	**H**yper-**V**elocity **I**mpact
LGG	**L**ight **G**as **G**un
LANL	**L**os **A**lamos **N**ational **L**aboratory
LEO	**L**ow **E**arth **O**rbit
MLSPH	**M**oving **L**east **S**quares **P**article **H**ydrodynamics
MM	**M**eshless **M**ethods
MMOD	**M**icro**M**eteoroids and **O**rbital **D**ebris
MPM	**M**aterial **P**oint **M**ethod
MPP	**M**assively **P**arallel **P**rocessing
OTM	**O**ptimal **T**ransportation **M**eshfree
RKPM	**R**eproducing **K**ernel **P**article **M**ethod
SBM	**S**tandard **B**reaking **M**odel

Abbreviation	Definition
SPH	**S**moothed **P**article **H**ydrodynamics

Symbols[1]

Symbol	Definition	Unit
a	Acceleration	[m/s^2]
b	Body Force per unit mass	[N/kg]
c_b	Material Bulk Speed of Sound	[m/s]
c_p	Material Specific Heat	[J/kgK]
E	Material Elastic Modulus	[GPA]
$E\ (e)$	Internal Energy (*per unit mass*)	[J] (*[J /kg]*)
F	Force acting on a FE Node or a Particle	[N]
G	Material Shear Modulus	[GPa]
g	Lagrange Multiplier Constrain	[ ]
h	SPH Smoothing Length	[mm]
K	Material Bulk Modulus	[GPa]
m	Mass	[kg]
N	FEM Shape Function	[ ]
p	Shock Pressure *(positive sign for compression)*	[GPa]
P_p	Projectile Momentum	[g m/s]
T	Temperature	[K]
T_0	Reference Temperature	[K]
T_m	Material Melting Temperature	[K]
v	Projectile Velocity	[m/s]
$V\ (v)$	Volume (*per unit mass*)	[m^3] (*[m^3/kg]*)
W_{AL}	Augmented Lagrange Multiplier Method Energy Function	[J]
W_L	Lagrange Multiplier Method Energy Function	[J]
W^{int}	Total Internal Potential Energy Function	[J]
W^{ext}	Total External Potential Energy Function	[J]
w	SPH Kernel Function	[ ]
U	Shock Speed within the Material	[m/s]
u	Particle Velocity within the Material	[m/s]
u	Nodes or Particles Displacement	[mm]

[1] Here only general symbols related to material properties and to the impact/penetration problem and thermodynamic definitions are given. Further notation, mainly related to models taken from the literature, is explained in the main text. For the sake of clarity, the notation for equations reported in this document reflects the definitions in the original works.

Symbol	Definition	Unit
$\Gamma_{Interface}$	Interface Boundary between Ω_{FEM} and Ω_{SPH}	[ ]
ϵ	Strain	[ ]
$\dot{\epsilon}$	Strain-rate	[1/s]
λ	Lagrange Multiplier	[ ]
Λ	Lagrange Multiplier Shape Function	[ ]
ν	Poisson's Ration	[ ]
Ω	Volumetric Domain	[ ]
Ω_B	SPH-FEM Blending Domain	[ ]
Ω^{int}	SPH-FEM Overlapping Domain	[ ]
Ω_{FEM}	Domain Modeled with FEM	[ ]
Ω_{SPH}	Domain Modeled with SPH	[ ]
Π	SPH Artificial Viscosity Coefficient	[Pa]
σ	Stress	[GPa]
σ_v	Von Mises Stress	[GPa]
σ_y	Material Yield Stress	[MPa]
ρ	Density	[g/cm^3]

1

Introduction

This chapter provides an overview of the thesis context and its associated challenges. It states the research objectives and the questions to be addressed. The chapter concludes by offering an outline of the thesis structure.

1.1. Problem Context

The near-Earth space has become an invaluable resource for addressing scientific and commercial challenges on Earth. Navigation, Earth observation, remote sensing, and communication are only a few examples of how space exploration has become a fundamental aspect of everyday life. Furthermore, more ambitious aspirations such as humanity's return to the Moon, travel to Mars, asteroid mining and even more exciting concepts are becoming a reality [3].

Nevertheless, as our dependence on space continues to increase, so does the quantity of debris orbiting the Earth. Despite current space policy considering Earth's orbital environment as a finite resource requiring safeguarding and careful planning [76], the forecast for space debris density is not optimistic. The sole solution remains implementing techniques to actively reduce the quantity of debris, particularly in Low Earth Orbit (LEO). In December 2019, Dr. Jan Wörner, the General Director of the European Space Agency (ESA), presented the initial space cleanup mission in partnership with the Swiss start-up CleanSpace. He emphasized the importance of removing debris from space to ensure safety and sustainability, saying, "*Imagine how dangerous sailing the high seas would be if all the ships ever lost in history were still drifting on top of the water. That is the current situation in orbit, and it cannot be allowed to continue*" [25].

Since the launch of the first Sputnik in 1957, humanity has continuously launched spacecrafts such as rockets, satellites, shuttles, and probes, and their fragments frequently remain abandoned in space. These assorted remnants, ranging in size from millimeter aluminum oxide particles to meter-long non-functioning satellites or launch vehicle upper stages, pose significant hazards to ongoing missions. According to ESA's space debris environment model MASTER there are approximately 34,000 debris objects greater than 10 cm in orbit, 900,000 objects between 1 cm and 10 cm and 128 million objects from 1 mm to 1 cm [24]. Therefore, it is highly

probable that all spacecraft will encounter space debris and micro-meteoroids during their operational lifespan.

Foreign object damage, defined as damage caused by any foreign article or substance to a spacecraft or system in general, including impacts from Micro-Meteoroids and Orbital Debris (MMOD), can result in substantial damage, potentially leading to mission failure. Such damage can range from localized craterization to subsystem failure or even complete loss of the vehicle [29]. The extent and the nature of damage rely on several elements, including the size, relative velocity of impact, angle of impact, density, and position of debris upon impact with the spacecraft.

Nonetheless, Hyper-Velocity Impacts (HVI) resulting from collisions at orbital velocities can have significant consequences, occurring at relative velocities higher than 7 km/s. Such impacts can generate a debris cloud, thereby increasing the amount of orbital debris. Potentially, the significant amount of space debris present could result in the *Kessler Syndrome*, a situation in which the density of objects in LEO due to space pollution is such that collisions between objects could lead to a cascade effect in which each collision creates debris, increasing the likelihood of further collisions [57]. The severity of the space debris issue shows no indications of improving in the near future. The cost to launch satellites into LEO is rapidly decreasing due to new innovations in launcher structures and propulsion technologies. As a result, space missions are becoming more frequent. Projections for the next few years predict a substantial increase in the number of objects orbiting the Earth (Fig. 1.1) [24]. Therefore, it is essential that spacecraft, whether manned or unmanned, are sufficiently shielded against the risk of HVI damage.

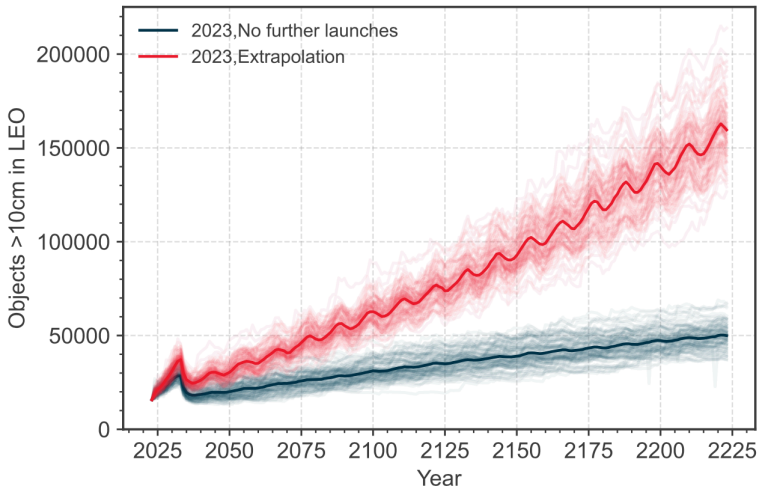

Figure 1.1: Number of objects in LEO in long-term environment evolution simulated scenarios [24].

Currently, engineering provides both active and passive defenses to address this issue. Active solutions, such as evasive maneuvers, are only applicable to trackable objects. For non-trackable objects with a main dimension less than 5 cm, space engineers must rely on passive systems [103]. Spacecraft shielding systems are effective passive means to protect against MMOD. The most commonly used and reliable solution is the *Whipple shield*, a dual-wall system proposed in 1947 [101]. The system typically comprises a single thin plate, called *bumper*,

that is positioned at a short distance from the spacecraft's primary structure. The shield's performance is dependent on many parameters (e.g., the bumper material, thickness and stand-off distance). Developments in shielding technology have led to the creation of new concepts that affect the number of bumpers and the materials used. Nevertheless, the working principle remains the same. The primary objective is to fragment and/or vaporize the projectile with the bumper, made of metal or composite material, which aims to disperse part of the impact energy. In fact, the initial impact results in the formation of a debris cloud that expands and distributes the energy and impulse load of the projectile over a larger area onto the rear wall, reducing the degree of damage of the spacecraft's primary structure [100].

On the other hand, with the increasing need for spacecraft stability to ensure the proper operation of increasingly precise instruments, perturbations encountered in orbital conditions, once considered negligible, have now become a problem [79, 87]. MMOD impacts can induce disturbance waves that propagate throughout the spacecraft structure, potentially leading to measurement inaccuracies that prevent successful mission fulfillment. Objective evaluation of impacts is necessary to prevent degradation of measurement accuracy. For the aforementioned reasons, comprehending the development of hyper-velocity impacts in orbit has become a significant matter of concern within the field of space engineering.

As mentioned above, most orbital impacts occur at speeds on the order of kilometers per second. Although experimental research is still needed, it can only offer a partial answer to meet the growing demand for more effective design solutions [100]. Furthermore, the intricate experimental procedures and high infrastructure costs make numerical simulation an appealing alternative. By simulating and testing, scientists can gain insight into the physics of such phenomena, model their effects, and aid in the development of dedicated protection systems and mitigation strategies. Additionally, numerical models can guide experimental design and provide solutions for unexplored scenarios that are not achievable in experiments. Therefore, simulations are a reliable, crucial and commonly used tool for HVI modeling [86].

Amidst these challenges, most numerical simulations for such events rely on *Smoothed Particle Hydrodynamics* (SPH) models [39]. This numerical methodology, unlike *Finite Element Method* (FEM), represents the most suitable for measuring phenomena characterized by substantial material deformations [109]. On the other hand, the computational cost of such modeling turns out to be particularly onerous. Additionally, given the prevalent practice of evaluating satellite dynamics using its FE model, a methodology capable of combining the two numerical techniques and exploiting both advantages is sought, guaranteeing accurate results while at the same time a sustainable computational cost [83]. In addition to the challenges posed by HVI simulations, meshless methods can also be advantageous in scenarios where certain regions of the domain undergo rapid changes in material parameters, loads, and/or boundary conditions. With this approach, it is possible to achieve a higher degree of accuracy in the results and to ensure reasonable simulation times by maintaining the use of FEM in regions away from critical areas.

1.2. Research Objective

The overall research objective that this thesis aims to achieve is to:

Develop a simulation methodology that exploits the strengths of SPH and FEM models to obtain accurate, yet computationally efficient, estimates of the stresses and accelerations transferred from the impacted zone to the rest of the structure as a consequence of hyper-velocity impacts.

1.3. Research Questions

To achieve the research objective, it is essential to formulate research questions that are supported by sub-questions. These sub-questions will highlight the main points of the thesis, including the advantages and shortcomings of the FEM and SPH modeling techniques, the challenges of the available coupling algorithms within the used software, and the importance of carefully selecting and choosing the methodology to evaluate simulation output and performance. The study will focus on flat plates as targets in simulations. Initially, a single plate configuration will be examined, followed by the use of a complete Whipple shield.

With this motivation outlined, this thesis aims to explore the following research questions as primary objectives:

Main Research Question:

"*What are the most relevant features of a simulation methodology able to integrate the strengths of SPH and FEM models and to transfer stress and acceleration information from the SPH modeled impact area to the FEM model of the entire satellite or surrounding area enabling efficient and accurate predictions of hypervelocity impacts effects in space?*"

Sub-questions:

- **Relevance of SPH & FEM:**
  - *What are the specific advantages of SPH in modeling hyper-velocity impacts and where are its shortcomings in terms of computational efficiency?*
  - *How do traditional FEM perform in comparison to SPH models in terms of accuracy and computational demands?*
- **Coupling Challenges:**
  - *What are the main challenges in coupling SPH models with FEM? What types of data need to be transferred from one environment to the other?*
  - *Are there existing methodologies or techniques that attempt such coupling (even in different research areas)? If so, how do they work and what are their limitations?*
- **Computational Efficacy and Accuracy:**
  - *How computational efficient is the SPH-FEM coupled method?*
  - *How can the accuracy of the proposed methodology be evaluated?*

- **Practical Applications:**
  - *How will the integrated SPH-FEM methodology improve the numerical assessment of stress fields induced by space debris and micro-meteoroids impacts?*
  - *In what ways can the developed methodology potentially aid in the advancement of satellite protection solutions?*

1.4. Structure of the Thesis

This thesis is structured as follows:

Chapter **1**. *Introduction* presents the context of the research topic and the threat of hyper-velocity impacts in space. The research objective is clearly stated, and the research questions are outlined. An overview of the thesis structure follows.

Chapter **2**. *Literature Review* provides a comprehensive understanding of the risk associated with the increasing density of space debris population and the associated threat of HVI to satellite functionality. It clearly states the limitations of both experimental research and numerical models. The most commonly used numerical models, FEM and SPH, are discussed. Additionally, a comprehensive review of coupling methods between meshless techniques and FEM has been conducted, filtering out the most relevant approaches. The chapter ends with some reflections on the current experimental and numerical methods to study the shock wave induced by HVI.

Chapter **3**. *Simulation Methodology for Single-Plate Hyper-Velocity Impacts* explains the methodological framework that is used to simulate HVI in a single-plate configuration. The iterative process and rationale behind the selection of specific models are outlined. Specifically, it examines how various factors, such as the shape of the SPH domain, the initial spatial SPH lattice configuration, and the coupling algorithm used to integrate SPH and FEM, affect the fidelity and accuracy of the simulations. To validate and benchmark these innovative simulation methodologies, the implemented models replicate the experimental tests conducted by Sibeaud et al. [88]. The evaluation encompasses a more comprehensive analysis than a mere comparison of post-impact geometric parameters. It includes an investigation of the energy evolution during the simulation and an examination of numerical reflection effects on stress wave propagation induced by the SPH-FEM interface. Initially, a quarter model of the experimental setup exploiting symmetry boundary condition is proposed, followed by the development and analysis of a full plate model.

Chapter **4**. *Simulation Methodology for Whipple Shield Hyper-Velocity Impacts* outlines the methodological framework for simulating HVI in a double-plate configuration, also known as a Whipple shield. Building upon the insights gained from the single-plate scenario discussed in the previous chapter, the proposed model incorporates a circular SPH domain, adaptive SPH/FEM contact algorithm, and quasi-isotropic SPH lattice for enhanced realism and accuracy. Validation of the model is conducted through simulation replication of experimental HVI tests conducted at the Ernst Mach Institute [18], with the experimental data courtesy of Airbus Defence and Space. First, the test to be reproduced and the implemented model geometry are described, simulation results are presented, a comparison between experimental and simulation results is made, and

finally an analysis of the HVI-induced stress and vibration propagation in the plates is performed.

Chapter **5**. *Conclusion and Recommendations* summarizes key findings and provides recommendations based on the research outcomes. It reviews the insights gained from the previous chapters and outlines potential research opportunities in the area of hyper-velocity impact simulation.

2

Literature Review

The investigation of hyper-velocity impacts can be considered to be of multidisciplinary interest. The development of the theories and knowledge necessary for an ever deeper understanding of this class of events finds its roots in fields that are only apparently distant. In this chapter, the reader is provided with the necessary tools for a clear and comprehensive understanding of the topic of this Master's thesis. First, in Section 2.1 the physical mechanisms related to HVI are discussed: hyper-velocity regime framework, phenomenology, material models, and equations of state. Subsequently, in Section 2.2 the most used numerical methods, through which the scientific community models HVI, are elucidated: the Smoothed-Particle Hydrodynamics and the Finite Element Method. Their formulation, attributes, strengths, and limitations are assessed. Additionally, various SPH/FEM coupling techniques, aimed at capturing the positive aspects of both, are presented. In conclusion, a brief look at the problem of shock waves induced by hyper-velocity impacts in space is treated in Section 2.3.

This comprehensive review not only lays the foundation for upcoming research questions, but also places this thesis within the broader academic discourse, clarifying its significance and potential contribution.

2.1. Physical fundamentals of Hyper-Velocity Impacts

Hyper-velocity impacts refer to high velocity collisions that occur at speeds typically exceeding several kilometers per second. Such impacts exhibit unique physical behaviors that differentiate them from collisions at lower velocities. In fact, the complex phenomenology arises from the interplay between kinetic energy, thermal energy and material properties. A deep understanding of the physical phenomena underlying HVI is crucial for numerical models. Indeed, accurate simulations hinge on faithfully replicating real-world dynamics, and any gaps or inaccuracies in knowledge can lead to significant discrepancies between simulated outcomes and actual events. This subsection delves into the fundamental physical principles governing hyper-velocity impacts and offers insights into their many implications.

The field of HVI physics originated in astronomy in the early 1930s [77], and gained traction in the context of metals as the Second World War approached [58]. The subsequent advent of spacecraft and satellite technology increased the interest in the field, with micro-meteoroids impacts becoming a significant concern [101]. By the mid-1960s, attention had shifted to the investigation of ceramics and fiber-polymer composites under these extreme conditions.

2.1.1. Hyper-Velocity Regime

To study the responses of materials to HVI, it is first necessary to establish the boundaries of what qualifies as "*Hyper-Velocity Impact*".

Impacts were traditionally classified by velocity. For high-strength metals, the upper limit to high-velocity impacts was set by impact speed around 1000 m/s [55]. This kind of impacts are often associated with the terminal ballistic regime. It includes a range of events, from rigid-body penetration to eroding projectiles, and strain rates that range from 10^2 to 10^5 1/s [55]. Despite the impact-induced pressure in this regime could potentially exceed the yield stress of the materials involved ($\rho v_0^2 \gg \sigma_y$), strength effects remain dominant, with thermal softening and melting playing only a secondary role [48].

By contrast, the hyper-velocity regime is characterized by strain rates greater than 10^7 1/s, exhibiting pronounced hydrodynamic behavior in which material strength becomes negligible and the focus shifts to material densities and pressure-volume relationships, captured by the Equation of State [55] (see Section 2.1.5). Here, shock wave generation and propagation become the dominant phenomena, potentially leading to melting or vaporization due to increased internal energy. The threshold to hyper-velocity was defined by impact speed around 3 km/s [55].

However, relying solely on velocity for impact classification is reductive, given the variance of related phenomena. Therefore, it is important to exercise some caution when using these general values to guide theoretical and numerical modeling, experimental design, and data interpretation.

Subsequent studies [89] have incorporated material properties into the classification of hyper-velocity impacts, leading to the "*sonic*" criterion, according to which the onset of the hydrodynamic regime can be roughly associated with the following condition regarding the impact velocity:

$$\frac{v_0}{\sqrt{K/\rho_0}} > 1 \tag{2.1}$$

where K is the material bulk modulus, ρ_0 the initial density, v_0 the projectile velocity, and $\sqrt{K/\rho_0}$ corresponding to the sound speed in the bulk. This method has been shown to be consistent with experimental results for impacts between projectiles and targets made of the same material.

Johnson et al. [48] extended this approach by proposing a non-dimensional parameter ($\rho {v_0}^2/\sigma_y$) as criterion for determining the impact regime. This parameter represents the ratio between the dynamic flow stress at the crater front and the material yield stress. A hyper-velocity threshold condition can be identified for values around 10^2–10^3. However, the use of material parameters from only one type of material hinders this approach and makes it difficult for it to be applied to

impacts involving heterogeneous materials. To address this limitation, a two-dimensional array of conditions based on parameters $\rho_p {v_0}^2/\sigma_{y,p}$ and $\rho_p v_0^2/\sigma_{y,t}$ has been developed [89], where the subscript p refers to the projectile material and t to the target.

2.1.2. Phenomenology

Ballistic velocity impacts can induce significant changes in pressure, density, and temperature within solids. When velocities are low, material yielding may occur in either the target or the projectile, which causes local plastic deformation. In such cases, the dissipation of the projectile's kinetic energy can be explained using common elastic-plastic mechanical parameters, constitutive relationships, and failure criteria utilized in the static analysis of ductile materials. As velocities increase, the penetration phenomenon becomes localized and moves to hydrodynamic behavior, with associated phase changes and fragmentation.

Using the sonic criterion, if the impact velocity is less than the velocity of the stress wave in the target $\left(v_0/\sqrt{K/\rho_0}\right) < 1$, plastic waves take over, affecting a volume that is larger than the projectile's size. As velocity increases, the volume affected becomes more localized. Beyond a certain threshold, the penetration process aligns with hydrodynamic equations, requiring careful consideration of thermodynamics, particularly in relation to shock wave propagation, material compression, and subsequent expansion. The material is initially compressed by a shock wave, which increases the entropy of the system. An isoentropic expansion comes after. Permanent changes in the microstructural configuration of the material reflect an increased entropy state. Stronger shock pressures can provide the material with energy beyond the heat of fusion, causing it to melt, vaporize, sublimate, and even generate plasma.

For impact scenarios, the material modeling can be broken down into constitutive model, failure and fracture criteria, and equation of state [110], respectively described in Section 2.1.3, Section 2.1.4, and in Section 2.1.5.

2.1.3. Constitutive Model

At moderate stress level, a variety of materials experience irreversible thermodynamic plastic deformation. The initiation of plastic deformation within these materials is influenced by their metallurgical structure, rate of deformation, and temperature, with a dependency on their previous deformation history.

Constitutive models for ductile materials that employ a linear strain-stress correlation lack the ability to describe complex phenomena such as work hardening, which is critical for a comprehensive understanding of dynamic material behavior. Therefore, several plasticity models have been formulated with the objective of describing material behavior during dynamic loading, encompassing work hardening, strain-rate hardening, and thermal softening.

One of the earliest models that accounts for strain-rate hardening was introduced by Cowper and Symonds [19]. Their method adjusts the constant yield stress with the equation:

$$\sigma_y(\dot{\epsilon}) = \sigma_{y,0}\left(1 + \frac{\dot{\epsilon}}{D}\right)^{1/p} \tag{2.2}$$

where p and D are hardening parameters retrieved experimentally.

Another commonly utilized constitutive formulation for numerical simulations is the elastic-plastic material model developed by Johnson-Cook [46]. This model includes the coupling of strain-rate and work hardening with thermal softening and can be expressed through the following relation:

$$\sigma_y(\epsilon_{pl}, \dot{\epsilon}_{pl}, T) = \left(A + B\,\epsilon_{pl}^n\right)\left(1 + C\,ln\frac{\dot{\epsilon}_{pl}}{\dot{\epsilon}_{pl,0}}\right)\left(1 - (T^*)^m\right) \tag{2.3}$$

with five parameters A, B, C, n, and m to be empirically evaluated, respectively representing the yield stress of material in standard conditions, the strain hardening variable, the strengthening factor of strain rate, the strain hardening factor, and the thermal softening coefficient. The model utilizes a reference plastic strain rate $\dot{\epsilon}_{pl,0} \cong 1.0\ s^{-1}$, and a non-dimensional temperature $T^* = \left(\frac{T - T_{ref}}{T_m - T_{ref}}\right)$. Here, T_{ref} represents a reference temperature below which yield stress is temperature independent, typically room conditions, while T_m is the melting temperature of the material.

The model developed by Steinberg et al. [92] is another notable constitutive formulation for impact simulations. It characterizes the relationship between yield strength and shear modulus (G), expressed as functions of pressure p and temperature T. These functions are shown in the following equations:

$$\sigma_y(p, T, \epsilon_{pl}) = \sigma_0\left[1 + \beta(\epsilon_{pl,0} + \epsilon_{pl}))\right]^n \left[1 + \frac{1}{\sigma_0}\frac{\partial \sigma_y}{\partial p}\frac{p}{\left(\frac{\rho}{\rho_0}\right)^{1/3}} + \frac{1}{G_0}\frac{\partial G}{\partial T}(T - T_0)\right] \tag{2.4}$$

$$G(p, T) = G_0\left[1 + \frac{1}{G_0}\frac{\partial G}{\partial p}\frac{p}{\left(\frac{\rho}{\rho_0}\right)^{1/3}} - \frac{1}{G_0}\frac{\partial G}{\partial T}(T - T_0)\right] \tag{2.5}$$

The model does not account for strain rate dependence because it is generally limited to scenarios with very high strain rates ($\dot{\epsilon} \gg 10^5\ s^{-1}$), where the increase in yield strength due to strain rate effects reaches saturation. Indeed, the empirical parameters for this model (β and n) have already been determined under extreme strain rate conditions [92].

2.1.4. Failure and Fracture Criteria

The study of material deformation behavior is essential in explaining the phenomena of penetration and debris cloud generation. However, the complex stress patterns and potential failures in and around the impact area make this analysis challenging.

Spall fracture is a key failure mechanism in impact phenomena, particularly relevant in situations where a thin target, such as the outer surface of a space structure, is impacted by a projectile at very high velocity. In such cases, if the initial shock waves (S_1 and S_2) are not dissipated before reaching the free edges, rarefaction tensile waves (R_1, R_2, R_3, and R_4) are generated and can induce in the material pressure levels that exceed the tensile strength of the material, resulting in fracture and fragmentation (Fig. 2.1) [31].

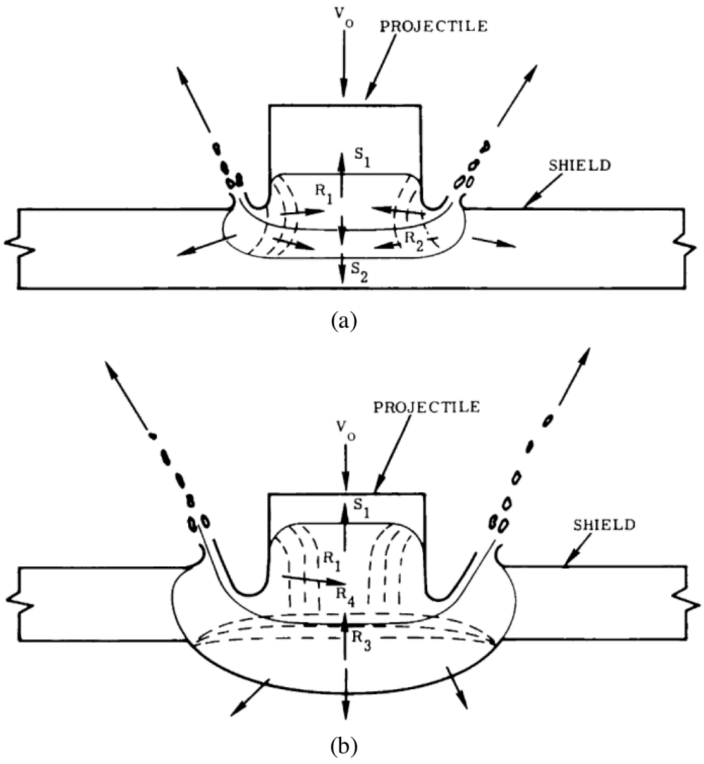

Figure 2.1: Estimated wave pattern in HVI [31].

Fracture under tension is only one of many possible failures in materials. In modeling material failure, several critical values such as fracture stress, maximum principal stress/strain, shear strain, volumetric strain, and total plastic work must be considered, which can concur in any stress state and lead to material failure. Additionally, when the applied load is inadequate to cause immediate fracture, micro-structural damages accumulate over time and progressively reduce the strength of the material. Computational models employ an auxiliary damage function to address this scenario, which captures the evolution of damage accumulation and integrates it until a predetermined critical value is reached. This approach is more sophisticated than relying on fixed, instantaneous parameters such as stress, strain, and plastic work to detect material failure.

In the Johnson-Cook damage model [50], material failure is determined by the damage parameter D, which is a cumulative measure of the plastic strain increment relative to the equivalent strain to fracture:

$$D = \sum \frac{\Delta \epsilon_{pl}}{\epsilon_f} \tag{2.6}$$

The strain to fracture, ϵ_f, takes into account the effects of stress, strain rate, and temperature. It is defined by:

$$\epsilon_f \left(\frac{p}{\sigma_v}, \dot{\epsilon}_{pl}, T \right) = \left[D_1 + D_2 \, e^{[D_3 (p/\sigma_v)]} \right] \left[1 + D_4 \, ln \left(\frac{\dot{\epsilon}_{pl}}{\dot{\epsilon}_{pl,0}} \right) \right] (1 + D_5 \, T^*) \tag{2.7}$$

Here, the failure parameters D_i are determined experimentally, while σ_v represents the equivalent von Mises stress. At failure ($D = 1$), the deviatoric stress components in the corresponding element or integration point are set to zero.

2.1.5. Equation of State

Equations of State (EOS) of materials describe the relationships among thermodynamic state variables, providing insights into the material's response under varying physical conditions [80]. These variables predominantly include pressure (p), mass density (ρ), specific internal energy (e), specific volume (v), and temperature (T).

EOSs can be divided into axiomatic and empirical: the former are based on a solid physical representation of the phenomena occurring in the material, especially at the molecular scale, such as the well-known *ideal gas law*, which is based on the kinetic theory of gases. The latter are defined as empirical mathematical models relating the thermodynamic variables and are usually implemented to describe the more complex behavior of solid materials.

To characterize the dynamics of shock wave propagation, a large number of experimental techniques have been developed, predominantly focusing on quantifying the shock speed (U) and particle velocities (u) within the compressed region trailing the shock front [16]. The relationship between U and u for most metals is expressed as $U = a + s_1 u$ [85], where empirical evidence suggests $a \approx c_b$ (the bulk speed of sound under uniaxial compression) [85], and s_1 a material-dependent parameter derived from fitting experimental data. Deviations from the linear correlation typically stem from material anomalies such as porosity, elastic waves, or phase transitions [85].

On the other hand, the *Rankine-Hugoniot relations*, also referred to as *jump conditions*, represent a crucial set of equations enforcing the conservation laws across the shock wave's discontinuity. Integrating this linear relationship with the Rankine-Hugoniot jump conditions, which define the state variable transformations across a shock wave, leads to the determination of the "*shock Hugoniot*" in the pressure-volume plane. This is often referred to as the "*shock EOS*":

$$p - p_0 = \frac{c_b^2 \, \rho_0 \, \rho \, (\rho - \rho_0)}{[\rho - s_1(\rho - \rho_0)]^2} = \frac{\rho_0 \, c_b^2 \, \eta}{(1 - s_1 \eta)^2} \tag{2.8}$$

where $\eta = 1 - (\rho_0/\rho)$ is the actual relative volume.

The *Mie–Grüneisen EOS* [35] is an empirical equation of state that relates the pressure and volume of a solid at a specific temperature, deriving its foundation from the *Grüneisen model* which delves into the influences of volumetric changes on the vibrational characteristics of a crystal lattice. The Grüneisen model can be mathematically represented as:

$$\Gamma = v \left(\frac{dp}{de} \right)_v \tag{2.9}$$

where v is the specific volume, p is the pressure, e is the specific internal energy, and Γ signifies the *Grüneisen parameter*, depicting the thermal pressure emanating from a collection of vibrating atoms. Assuming the independence of Γ value in relation to p and e, the integration of the Grüneisen model yields:

$$p - p_0 = \frac{\Gamma}{v_0}(e - e_0) = \rho_0 \, \Gamma \, (e - e_0) \tag{2.10}$$

with p_0 and e_0 representing the pressure and internal energy at a specified reference state.

The Mie–Grüneisen EOS finds extensive application in modeling material behavior under high-pressure and energy scenarios, such as shock-compressed solids. For this reason, the reference state quantities can be directly estimated from the Rankine–Hugoniot conditions (p_H and e_H):

$$p\left(\rho, e\right) = p_H + \rho_0 \, \Gamma \left(e - e_H\right) \tag{2.11}$$

The Hugoniot state parameters are deduced using Eq. (2.8) as:

$$p_H = p_0 + \rho_0 \, c_b^2 \, \frac{\eta}{(1 - s_1 \eta)^2} \tag{2.12}$$

$$e_H = e_0 + \frac{\eta}{\rho_0} p_H - \frac{\eta^2}{2} \, \frac{c_b^2}{(1 - s_1 \eta)^2} \tag{2.13}$$

leading to the resulting Mie–Grüneisen EOS:

$$p\left(\rho, e\right) = p_0 \left(1 - \eta \Gamma\right) + \frac{\rho_0 \, c_b^2 \, \eta}{(1 - s_1 \eta)^2} + \rho_0 \Gamma (e - e_0) \tag{2.14}$$

Moreover, an expansion specific EOS is required, as the aforementioned model is tailored for compression states only, possibly resulting in negative wave velocities under tensile stresses. The polynomial EOS is generally implemented for these circumstances:

$$p(\rho, e) = K_1 \eta + K_2 \eta^2 + K_3 \eta^3 + (B_0 + B_1 \eta) \rho_0 e \tag{2.15}$$

The parameters of this expansion EOS (K_i and B_i) can be determined by fitting experimental data or by establishing appropriate correlations with the Hugoniot state.

Contrastingly, in extreme conditions like HVI, where chemical dissociation and thermal electronic excitation processes are prevalent, the assumption of a linear Γ in relation to density becomes untenable. This is where the *Tillotson EOS* [96] comes into play, specifically designed for such hyper-velocity impact simulations involving phase transformations - melting or vaporization - in the target or the projectile.

In addition to the aforementioned models, tabular databases such as the *SESAME* computer-based library developed by *Los Alamos National Laboratory* (LANL), also play a significant role in hyper-velocity impact simulations [69]. These databases offer a vast array of experimentally derived pressure values as functions of density and internal energy, enabling the derivation of an equilibrium surface in the thermodynamic state space.

2.2. Numerical models

On-ground experiments represent the most direct method of studying HVI, but testing is limited by launch capability and diagnostic equipment. In fact, there is a significant difference in velocity and mass between the projectiles that can be launched by the state-of-art HVI facilities available today at various research centers around the world and actual space debris. As stated earlier, the existing diagnostic equipment solely permits the observation of the overall shape and structure of the debris cloud, and allows the preliminary tracking of only the largest fragments of that

cloud [99]. Consequently, it is not feasible to meticulously observe the impact process, including the material fragmentation and debris cloud evolution over time. High costs, time consuming and stringent technical requirements make large-scale testing difficult [39].

To minimize the number of tests performed, several empirical and semi-empirical models have been developed to characterize HVI. The empirical models are based on impact tests performed in experiments and on orbital missions. NASA's Standard Breaking Model (SBM), implemented in 1998 [54], is the most widely used empirical model. Based on all available data sources at the time, the SBM provides size, mass, and velocity distributions of debris clouds from hypervelocity collisions. On the other hand, semi-empirical models are based on theoretical laws and procedures, but also incorporate assumptions and parameterizations derived from experimental data. They use a wide range of empirical results to rule out physically impossible outcomes, relying on conservation principles. These techniques are useful when detailed data on the objects involved in the collision and event kinematics are lacking, and when studying multiple scenarios requires multiple runs. The most used are the Fragmentation Algorithms for Strategic and Theater Targets (FASTT) [71] and the Collision Simulation Tool (CST) [30].

Conversely, numerical simulation reduces the cost and time of research, allowing optimization of experimental methods and material selection, and offering the possibility to study the impact process in detail [39]. Moreover, simulation has the potential to address unexplored scenarios by leading the experimental design. This tool offers a clear understanding of the impact process and the internal mechanism of hyper-velocity phenomena, and can be used to verify the dynamic constitutive relationship and dynamic fragmentation of materials. Consequently, numerical simulation has been widely used in the investigation of such problems.

Early numerical simulations of impact were focused on the higher speed regimes, where the materials can be considered as fluids, and the contributions of strengths can be neglected (see Section 2.1.1) [27]. The result has been the creation of "*hydro-codes*", specialized computer programs, in the field of impact physics. Over time, hydro-codes have evolved to deal with lower velocity regimes by incorporating additional material characteristics.

Hydro-codes have been in use since 1945 and are now prevalent in academic and industrial applications because of their numerical stability and accurate correlation with experimental data [89]. As computational technology advanced, hydro-codes underwent rapid evolution during the 1960s and 1970s [53]. Both Eulerian [95] and Lagrangian [47] methods were introduced, along with coupled approaches like Arbitrary Lagrangian-Eulerian (ALE) [40]. In the late 1970s, meshless Lagrangian approach, known as Smoothed-Particle Hydrodynamics (SPH), was first proposed for astronomical research [68, 33] and later extended to impact and shock physics.

2.2.1. FEM

The Finite Element Method (FEM) is a leading numerical technique for solving differential equations commonly encountered in various engineering models that cannot otherwise be solved analytically. FEM is widely employed in diverse fields including structural analysis, heat conduction, and fluid dynamics. It offers a sophisticated approach to address specific boundary value problems in two or three spatial dimensions by solving partial differential equations [67].

The development of FEM as a numerical modeling methodology can be traced back to the early 1940s [64]. Hrennikof, a Russian-Canadian structural engineer, presented an innovative membrane and plate model built as a lattice framework [42]. His strategy was to discretize the solution domain into a lattice-structured mesh, marking the genesis of mesh discretization techniques.

The Finite Element Method decomposes large systems into smaller, more manageable subunits called Finite Elements. To accomplish this decomposition, the method involves spatial discretization using a mesh that defines the numerical domain of the solution (Fig. 2.2) [67]. By formulating a boundary value problem via FEM, a set of algebraic equations is generated to approximate the function in the specified domain. Next, the basic equations that express these limited elements are combined into a comprehensive system that reflects the entire problem. By reducing the associated error function, an accurate solution is sought [43].

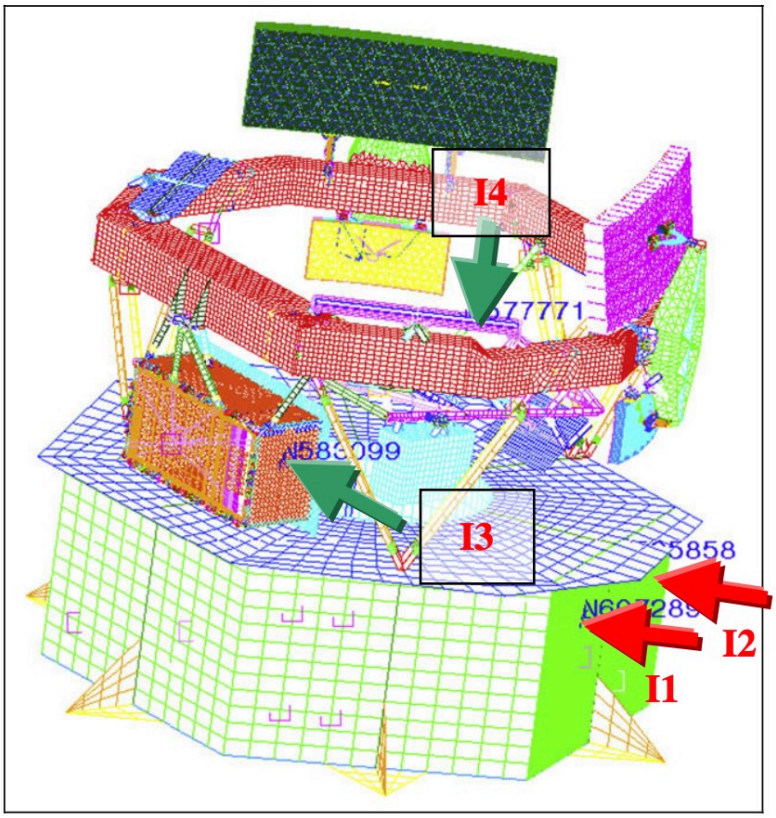

Figure 2.2: Overall view of GAIA satellite finite-element model [97].

Due to the increasing interest in hyper-velocity impacts and the inherent limitations of today's experimental structures, a growing number of researchers have become involved in the numerical representation of these high-energy impacts [100]. Initial numerical modeling efforts involved performing FEM simulations. Various FEM-based numerical algorithms, such as the Lagrange algorithm [10], Euler algorithm [41], and ALE [2], were investigated to overcome the challenges of HVI.

However, traditional FEM techniques have limitations when applied to HVIs as FEM-based pre-

dictions do not agree with empirical observations. These limitations arise due to the high deformation and abrupt interface changes that the material undergoes during the removal of damaged elements through numerical erosion mechanisms. Additionally, the removal of multiple elements results in a significant loss of mass, momentum, and energy within the system. Therefore, the remaining elements are insufficient to represent the post-impact behavior accurately. It is challenging to obtain precise results through FEM alone for HVIs that exhibit significant material deformation, penetration, and fragmentation. In fact, the use of conventional FEM for HVIs appears to be inapplicable. [5, 39, 106].

2.2.2. SPH

Nowadays, Meshless Methods (MM) are the primary algorithms used for simulating hyper-velocity impacts, explosions, crack propagation, and metal forming [14]. Out of these methods, Smoothed-Particle Hydrodynamics, Optimal Transportation Meshfree (OTM) [61], Material Point Method (MPM) [70], and Combined Particle-Element Method (CPEM) [51] have achieved good results. Notably, SPH has shown exceptional predictive ability in HVI problems [90], making it the focus of further investigation.

SPH is a Lagrange-type particle-based meshless method developed in 1977 by Lucy, Gingold, and Monaghan for simulating star formation [33, 68]. This approach was designed to solve mesh tangling difficulties that arise in extreme deformation scenarios encountered in FEM. The primary distinction between classical methods and SPH is the lack of a grid. The continuum is represented by a collection of interacting discrete mass particles. Indeed, the SPH method utilizes a set of interpolation points for discretizing the volume of a system. As a result, particles constitute the computational framework on which the governing equations are resolved. Every particle contains discrete values of the computed continuous field and moves following the law of the governing equations. By using a kernel function, SPH achieves stable and smooth approximations of the field functions and their derivatives by weighing the influence of neighboring particles. The fundamental principle of this technique is displayed in Fig. 2.3. SPH has a time-varying node connectivity. This dynamic nature of particle interactions enables the modeling of problems that entail significant deformations, such as hyper-velocity impacts.

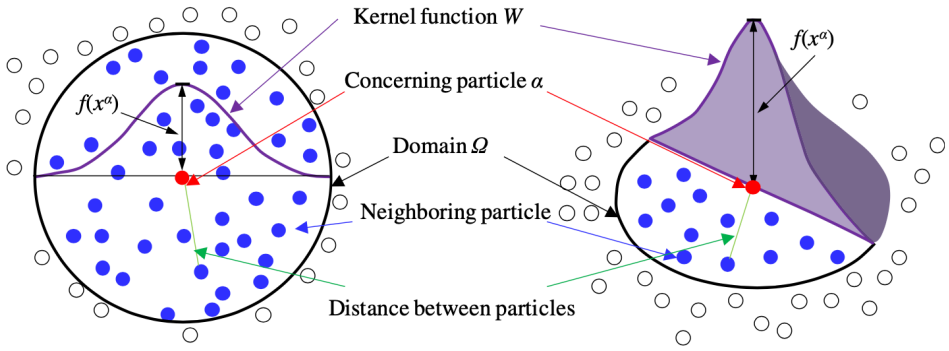

Figure 2.3: Illustration of the SPH concept for a 2D domain Ω with kernel function W [20].

In the following, the basic formulation of the SPH method, including its mathematical basis and practical implementation of the code will be presented. For a complete discussion, readers are recommended to consult [75] and [65].

The SPH formulation follows a two-step process when applied to continuous equations in their strong form. Initially, field variables such as density, velocities and energy are converted to a continuous format using an integral representation, known as the *kernel approximation*. The next step involves *particle approximation*. In this case, the domain is discretized into predefined particles and the field variables are estimated by a smooth summation of the related values of the neighbouring particles. The steps are described below in more detail:

Kernel approximations – In the SPH approach, kernel approximation serves as a method to represent field variables and their derivatives in an integrated continuous manner. This concept leans on the precise representation of a function $f(x)$, utilizing the Dirac Delta function $\delta(x)$ sampling characteristic as illustrated:

$$f(x) = \int_{\Omega} f(x')\, \delta(x - x')\, dx' \tag{2.16}$$

Here, as in Fig. 2.3, Ω denotes the volumetric domain used to study the function. Since Dirac's Delta is impulsive, it can be used only when $f(x)$ is continuous in its domain. The kernel approximation procedure replaces Dirac's Delta with an appropriate kernel function $w(x, h)$. This function adjusts the contributions within a specific radius of influence, determined by a parameter called "*smoothing length*" or h. This leads to the kernel approximation of $f(x)$, represented as:

$$< f(x) > = \int_{\Omega} f(x')\, w(x - x',\, h)\, dx' \tag{2.17}$$

When deriving the field's gradient kernel approximation, one employs Eq. (2.17), substituting $f(x)$ with $\nabla f(x)$:

$$< \nabla f(x) > = \int_{\Omega} (\nabla f(x'))\ w(x - x',\, h)\, dx' \tag{2.18}$$

Here, $\nabla f(x')$ symbolizes the gradients corresponding to x'. Further manipulation yields:

$$< \nabla f(x) > = -\int_{\Omega} f(x')\, \nabla w(x - x',\, h)\, dx' \tag{2.19}$$

Kernel functions must meet certain mathematical criteria in order to provide accurate approximations:

1. *Normalisation condition* − The integration of the smoothing function should be unity:

$$\int_{\Omega} w(x - x',\, h)\, dx' = 1 \tag{2.20}$$

2. *Delta function property* − As smoothing length collapses, the function should approach the Dirac Delta:

$$\lim_{h \to 0} w(x - x',\, h) = \delta(x - x') \tag{2.21}$$

3. *Parity Condition* − The kernel function should be symmetrical and thus maintains the evenness:

$$w(x - x',\, h) = w(x' - x,\, h) \tag{2.22}$$

4. *Compact Condition* − Beyond a certain threshold, the smoothing effect becomes non-

existent:

$$w(x - x',\, h) = 0 \qquad \text{for} \qquad |x - x'| > \kappa\, h \qquad (\kappa \in \mathbb{N}) \tag{2.23}$$

5. *Positivity* − The kernel function should always remain positive.
6. *Decay Behaviour* - As it approaches the edge of the support, the kernel function should decrease uniformly to zero.
7. *Smoothness* − The function must exhibit a degree of smoothness to ensure continuity in its derivatives.

The Eq. (2.23) delineates the effective area of the smoothing function, referred to as κh or the support domain. Within this domain, the function is consistently positive, decreasing and smooth. This implies that the integration domain, Ω, can be reduced only to the support domain for any integration at a particular location x.

The parity condition of the kernel function (Eq. (2.22)) is set such that the accuracy of the approximation can achieve second-order precision. By expressing the field variable through a Taylor series expansion, it is possible to rewrite Eq. (2.17) as:

$$\begin{aligned} < f(x) > &= \int_\Omega \Big\{ \left[f(x) + f'(x)(x - x') + O((x - x')^2) \right]\, w(x - x',\, h) \Big\}\, dx' = \\ &= f(x) \int_\Omega w(x - x',\, h)\, dx' + f'(x) \int_\Omega \left[(x - x') w(x - x',\, h) \right]\, dx' + O(h^2) \end{aligned} \tag{2.24}$$

where $O((x - x')^2)$ symbolizes the residual term of quadratic order based on the displacement $(x - x')$. If the kernel function is even, the second integral in Eq. (2.24) disappears, and the first integral equates to $f(x)$, as outlined by condition Eq. (2.20). The compaction condition Eq. (2.23) aids in constraining the residual term to the squared smoothing length's residual. The final, simplified expression is:

$$< f(X) > = f(X) + O(h^2) \tag{2.25}$$

This articulates the SPH method's capacity for second-order precision.

The kernel function, denoted as W, measures the effect of neighboring particles on a designated interpolation point. The *cubic B-spline*, the most extensively utilized smoothing kernel within the SPH community, is also implemented in LS-DYNA, the software employed for this research. The cubic B-spline kernel function is defined as:

$$w(x, h) = C_D^{spline}(h) \cdot \begin{cases} 1 - \frac{3}{2}\bar{r}^2 + \frac{3}{4}\bar{r}^3 & \text{for} \quad 0 \le \bar{r} < 1 \\ \frac{1}{4}(2 - \bar{r})^3 & \text{for} \quad 1 \le \bar{r} < 2 \\ 0 & \text{for} \quad \bar{r} \ge 2 \end{cases} \tag{2.26}$$

In this context, the symbol $\bar{r} = |x - x'|/h$ represents the standardized distance between the integration point and its neighboring particles. Equation (2.27) details the value of the constant $C_D^{spline}(h)$, which is influenced by the spatial dimensions, type of kernel function employed, and

smoothing length h that defines the active region of the smoothing function W.

$$C_D^{spline}(h) = \begin{cases} \frac{1}{h} & \text{for 1D space} \\ \frac{15}{7\pi} \cdot \frac{1}{h^2} & \text{for 2D space} \\ \frac{3}{2\pi} \cdot \frac{1}{h^3} & \text{for 3D space} \end{cases} \tag{2.27}$$

Particle approximation – After establishing the kernel approximation, the next step is to discretize the domain using the particle approximation technique. The computational domain (Ω) is divided into a specific number of particles, which are arranged freely in three-dimensional space. Field variables are then identified at these locations, which are essential for performing interpolation, derivation, and integration tasks.

Each particle i, has an associated finite volume, ΔV_i. Through the expression of particle mass m_i and mass density ρ_i, can be used in the kernel approximation of state functions. The particle approximation may be directly employed to express the discretized versions of Eqs. (2.17) and (2.19). This is elucidated in the following mathematical relations:

$$< f(x_i) > \; = \sum_{j=1}^{N} \frac{m_j}{\rho_j} \; f(x_j) \; w(x_i - x_j, h) \tag{2.28}$$

$$< \nabla f(x_i) > \; = - \sum_{j=1}^{N} \frac{m_j}{\rho_j} \; f(x_j) \; \nabla w(x_i - x_j, h) \tag{2.29}$$

where N denotes the number of particles in the designated vicinity. The above equation states that the estimated value of a field variable (or its gradient) at a specific point can be calculated by adding up the field variable values of particles situated within the compact support domain. This computation is affected by the weights of the kernel function.

When numerically implementing the articulated method, there are several significant aspects that require discussion, such as time integration and the management of boundary elements. This discussion addresses the considerations specific to the implementation carried out within the commercial solver, LS-DYNA, utilized for this research project. A thorough analysis of the implementation's technical details is available in the official software manual [36].

Time Integration – In numerical solvers, the main task is to integrate the discretized equations of motion. The first-order explicit integration method is employed in SPH due to its computational simplicity and efficiency. Although more intricate schemes, such as implicit methods, may provide enhanced stability and accuracy, those characteristics are not the primary focus in this particular scenario. In fact, the SPH simulations require very short time steps, specifically to capture the extensive deformations of the system and the brief duration of the events under investigation. For example, hyper-velocity impacts occur within the microsecond (μs) time scale.

To ensure numerical stability, the time step (δt) of any explicit integration scheme must conform to the *Courant-Friedrichs-Lewy (CFL) Condition* for every computational element. It can be expressed by the equation:

$$\delta t \; < C_{max} \; \frac{L_i^*}{v_i^*} \tag{2.30}$$

Where C_{max} indicates the maximum Courant number for the specific integration technique being used. For the $i-th$ computational element, the characteristic length and velocity are represented by L_i^* and v_i^*, respectively. In SPH computations, these quantities are generally understood as the smoothing length h_i and velocity of sound c_i plus the velocity magnitude of the particle v_i. The velocity of sound is defined as $c_i = (E_i/\rho_i)^{1/2}$, where E_i represents the rigidity value. Thus, the time step implemented in the LS-DYNA SPH formulation is:

$$\delta t \ = C_{max} \ \min_i \left(\frac{h_i}{c_i + v_i} \right) \tag{2.31}$$

Smoothing Length Evolution – The smoothing length, denoted as h, is a highly important parameter that affects both the accuracy of the solution and the computational effort associated with it. To maintain the desired level of accuracy while avoiding unnecessary computational overhead, it is advantageous to enable h to evolve spatially – varying from one particle to another – and temporally. One possible objective is to maintain a constant number of particles within the compact support area. This implies that the local particle density should be inversely proportional to the smoothing length in each dimension. Using D to denote the dimensionality of the problem, two methods can be implemented to accomplish this goal:

1. A straightforward approach employs a power law relation given by

$$h = h_0 \left(\frac{\rho_0}{\rho} \right)^{1/D} \tag{2.32}$$

2. An alternative strategy is to introduce a time derivative for the smoothing length linked inversely to the time derivative of the density:

$$\frac{Dh}{Dt} = -\frac{1}{D} \frac{h}{\rho} \frac{D\rho}{Dt} \tag{2.33}$$

Neighbouring Particle Searching – Within the SPH method framework, the absence of a fixed mesh means that neighboring particles relative to a particular node will change as the system progresses. As a result, an efficient searching algorithm is necessary to identify the support domain for each node at every computational time step. Due to the frequency of this operation, algorithm efficiency is of utmost importance. The current solver implementation utilizes "*bucket sorting*" technique. By dividing the domain into cubical cells or "buckets," this method simplifies identifying neighboring particles only in the current and adjoining ones.

Boundary Element and Contact – The normalization condition, expressed by Eq. (2.20), for the smoothing function W is compromised near and on the domain boundary. To address this issue, one proposed solution is to strategically introduce "*ghost particles*" along the domain boundary and beyond it. These particles offer supplementary repulsive forces at the boundary, thereby preventing active particles from penetrating it. Similarly, when two separate SPH bodies come closer together, the combined contributions of the particles in the kernel summation produce repulsive forces. Thus, specific contact algorithms common in conventional Lagrangian numerical strategies are no longer needed.

Calculation Cycle – The solver performs calculations at each time step, as shown in Fig. 2.4.

Using the updated state variables, such as position and velocity, the loop proceeds by recalculating and updating the smoothing lengths for each particle by exploiting one of the techniques described in smoothing length evolution. This allows the neighbouring particle searching algorithm to identify the support domain for each node. The following operations involve calculating the SPH approximations for the density and strain rates. The values are entered into the constitutive laws and Equation of State appropriately chosen depending on the phenomenology of the event to be simulated to calculate the pressures, stresses and internal energy values. These metrics help determine the forces acting on the particles, facilitating effective management of boundary interactions and contacts between parts. Once these preparatory steps are completed, the particle accelerations are fully calculated and integrated into the explicit scheme, resulting in a progression of time steps and the start of a new cycle.

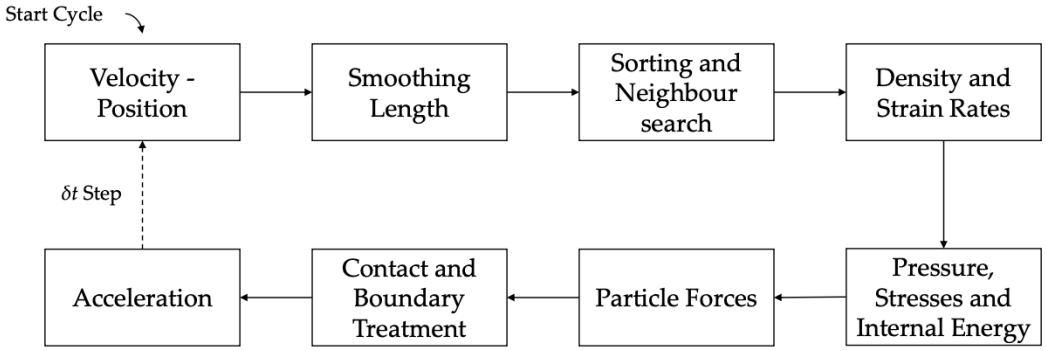

Figure 2.4: Integration cycle steps in the LS-DYNA SPH solver [36].

Artificial Viscosity – When conducting computational simulations, accurately depicting phenomena such as shock wave propagation requires specific considerations. In particular, it is necessary to counteract potential numerical fluctuations and non-physical oscillations in the regions close to the shock. To address this challenge, an artificial dissipation term known as *artificial viscosity* (AV) is introduced to simulate the conversion of kinetic energy into thermal energy. The implementation of LS-DYNA's artificial viscosity is presented in the following equation:

$$\Pi_{ij} = \frac{-\alpha \bar{c}_{ij} \mu_{ij} + \beta \mu_{ij}^2}{\bar{\rho}_{ij}} \tag{2.34}$$

$$\mu_{ij} = \begin{cases} \frac{\bar{h}_{ij}\,(\vec{v}_{ij}\cdot\vec{x}_{ij})}{|x_{ij}|^2 + 0.01\bar{h}_{ij}^2} & \text{for} \quad \vec{v}_{ij}\cdot\vec{x}_{ij} < 0 \\ 0 & \text{for} \quad \vec{v}_{ij}\cdot\vec{x}_{ij} \geq 0 \end{cases} \tag{2.35}$$

Here, α and β are modifiable constants, typically adjusted for specific scenarios, while c represents the material bulk speed of sound. The notations $\bar{c}_{ij}$, $\bar{\rho}_{ij}$, and $\bar{h}_{ij}$ denote averaged quantities between particles i and j. The term $0.01\,\bar{h}_{ij}$ in the denominator of μ_{ij} serves to stabilize computations for approaching particles. $\vec{v}_{ij}$ and $\vec{x}_{ij}$ represent respectively the relative velocity and position. The component scaled by α provides the bulk viscosity, whereas the term associated with β aims to counteract particle interpenetration at elevated Mach numbers.

The artificial viscosity, Π_{ij}, has pressure dimensions, and can be directly integrated into the equations of motion as an augmented hydrostatic pressure. However, it is important to note that this term can occasionally result in non-physical energy dissipation. Such pitfalls become

pronounced when the considered element's aspect ratio deviates significantly from unity, as observed during extreme deformations. This deviation can render the computed characteristic length L^* misleading. Hence, it is crucial to assign constants α and β judiciously. In certain cases, adding an extra artificial heating term may correct such anomalies.

Tensile Instability and Further Formulations – The described SPH method is a basic formulation. Over time, numerous variations have been suggested, each with distinct objectives, mainly to address inherent challenges. LS-DYNA incorporates various formulations, each tailored to better model specific phenomena.

New formulations also emerge with the intent to solve issues inherent to the classical SPH formulation. Indeed, a significant limitation when employing the classical SPH formulation in computational solid mechanics is the so-called *tensile instability*. This problem stems from the numerical instability of particles under certain tensile stress scenarios, potentially leading to particle aggregation, material breakage, or numerical discrepancies.

One attempt to combat tensile instability involved introducing a repulsive force when particles get too close to one another. This artificial stress term, outlined in Refs. [74, 34], stabilizes SPH simulations, but only for 2D problems.

Another approach to address the instability issue is represented by the *Corrective SPH* (CSPH), proposed by Chen in Ref. [13]. Chen's methodology relies on transitioning the kernel estimate to a Taylor series expansion. Furthermore, in another strategy, Sugiura and Inutsuka [93] drew inspiration from the *Godunov SPH* method [45], incorporating a Riemann solver and reaching second-order spatial precision.

The aforementioned strategies heavily rely on traditional SPH formulations, where particles interact through a kernel function. This method means that particles can move into and out of each other's support domains as materials deform, contributing to tensile instability [82]. Thus, the *Total Lagrangian SPH* was recently developed [84] which computes the kernel function based on the reference configuration rather than on the current one, showing promising results in mitigating tensile instability in HVI simulations.

The pseudo-spring technique is another noteworthy method, initially formulated to represent crack growth in impact scenarios [12]. *Pseudo-spring SPH* fosters efficient immediate neighbor interactions by connecting neighbors via pseudo-springs. Material degradation is evaluated through the behavior of these pseudo-springs, paving the way for intriguing insights into crack propagation during impacts.

Further enhancements to the SPH method encompass forms like *Moving Least Squares Particle Hydrodynamics* (MLSPH) [22], *Godunov SPH* [45], δ*-SPH* [73], and *Gamma-SPH* [62], each inspired by different application challenges of SPH. To provide a broader perspective, Fig. 2.5 chronicles key SPH developments over the past decades, showcasing the most important formats in this evolving landscape.

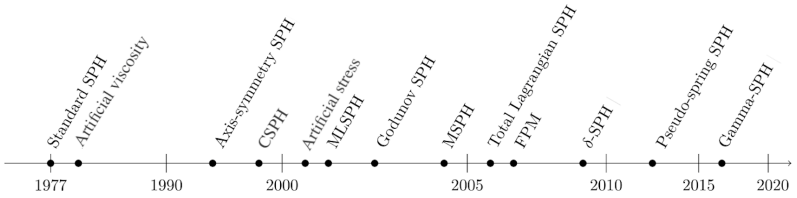

Figure 2.5: Developments of SPH methods [72].

In conclusion, despite their advantages, meshless methods, including SPH, have notable shortcomings. These include challenges in defining physical boundaries, tensile instability, computational cost, and ambiguous material boundaries, all of which hinder the accurate representation of HVIs. In addition, these methods are not well suited for simulating composites and foams, limiting in-depth exploration of the impacts problem. Some of these challenges have been addressed, such as the improvement of physical boundaries for SPH particles and techniques to reduce tensile instability. However, the problem of vague material boundaries remains, due to the inherent limitation that a single-node particle cannot adequately represent boundary shapes. This underscores the importance of innovative numerical simulation methods in future research to overcome these limitations.

2.2.3. Coupling Techniques

In the field of solid mechanics, the Finite Element Method has long been the numerical tool of choice. Over the years, it has evolved into a mature and robust technique that has found application in various commercial software solutions. Despite its widespread use and proven effectiveness in predicting structural response under various loading conditions, FEM has certain limitations. In particular, it exhibits reduced reliability when applied to scenarios involving large deformations and structural failures under dynamic loading, such as in cases of fracture and fragmentation [5].

The shortcomings of FEM stem primarily from its inherent mesh partitioning requirements and its sensitivity to mesh distortion due to the fixed topological connectivity [83]. This sensitivity can lead to inaccurate results that lack physical relevance. This problem becomes particularly pronounced when FEM is used to simulate scenarios such as HVI, penetration resistance, ice breakage, and crash events that involve material failure and significant deformation [106].

The inability of FEM to satisfactorily predict continuous failure mechanisms introduces additional numerical challenges [21]. One approach to mitigate this challenge is to adopt a *numerical erosion criterion* for solid elements [21], which facilitates the removal of distorted elements based on predefined failure criteria that include pressure, stress, strain, damage, or temperature. It is important to note that this erosion function is not a material property, but rather a numerical technique used in conjunction with FEM to predict fracture patterns, with erosion parameters determined empirically.

However, this approach is not without its drawbacks. The erosion of an element will either reduce its mass to zero - in violation of the conservation of mass principle - or redistribute its mass

to the corner nodes [21]. In both cases, the compressive strength and internal energy of the eroded element are lost. Substantial elimination of elements results in a significant loss of mass, momentum, and energy in the system, rendering the remaining elements inadequate to accurately represent post-impact reality. In addition, the process of removing failed elements can cause abrupt changes at the interface [39], making it difficult to simulate structural failure involving material fragmentation. Given these challenges, obtaining accurate results for HVI problems using traditional FEM becomes infeasible [5].

For the aforementioned reasons, meshless methods (MM), in particular SPH, have emerged as a robust alternative to the FEM. Originating as one of the pioneering particle methods in computational mechanics, SPH has shown unique efficiency in dealing with large deformation problems, circumventing the mesh distortion problems prevalent in FEM thanks to its nodal approximation without meshing [56]. SPH is particularly advantageous in scenarios involving fluid-like media behavior, using Lagrangian particles to describe deformation and smoothly transitioning from continuum to fragmented states. This capability mitigates material interface problems often encountered in Eulerian codes, making SPH the method of choice for HVI simulations.

Unlike FEM, where numerical erosion leads to mass inconsistency, SPH maintains constant mass throughout the simulation. The interparticle links in SPH fail when the particle separation exceeds a critical threshold, but the particles remain within the problem domain. In this case, the deviatoric stresses in the SPH particles are reduced to zero and the particles carry only compressive stresses, exhibiting fluid-like behavior [21]. This feature is particularly beneficial in fracture-dominated simulations, ensuring conservation of mass, momentum, and energy.

However, SPH is not without its challenges. It struggles with tensile instability, ambiguous material boundary definitions, and difficulty in post-impact fragment identification within debris clouds, which complicates damage analysis in rear-plate impact situations [39]. In addition, SPH is poorly suited for simulating composite [102] and foam materials [15], which pose significant obstacles to advanced HVI studies that consider current trends in space shield structure. Despite these challenges, considerable research efforts in MM have attempted to address issues related to consistency, stability, and Dirichlet boundary conditions, resulting in the development of viable solutions [37]. Nevertheless, it is imperative to acknowledge that SPH, while superior in certain aspects, cannot achieve the efficiency of FEM in structural response applications, primarily due to its high computational requirements. The extensive neighbor search and physical quantity calculations required for each particle in SPH make it particularly onerous for large-scale and three-dimensional problems, resulting in reduced computational efficiency [72].

Consequently, an efficient simulation can only be achieved by strategically discretizing certain domain regions with particle methods while using finite elements for the rest of the domain [83]. A common numerical solution technique to optimize computational cost is the coupling of SPH with FEM, providing a potentially accurate solution for numerical simulations in HVI scenarios.

The integration of MM-FEM coupling aims at exploiting the strengths of both approaches. On the one hand, particles are used to describe localized region near the impact zone where fracture or deformation is expected to predominate. On the other hand, FEM addresses the global struc-

tural response and helps save computational cost by reducing the number of active SPH particles. This method not only introduces clear material boundaries and a wide range of modelable materials, but also allows accurate fracture modeling. As a result, this approach facilitates the simulation of highly deformed or fractured materials without the need to remove mass-carrying elements.

While this issue is prevalent in HVI simulations, the applicability of the coupled SPH-FE method extends to a broader context. It is particularly advantageous in scenarios characterized by rapid changes in material parameters, loads, or boundary conditions within specific domain regions. In addition, nonlinear problems that require repeated refinement of meshless approximations or multiple iterations of simple linearized problems also benefit from coupled methods [56].

Several papers have been devoted to coupling algorithms. Johnson in 1994 [49], shows that the primary differences between SPH and FEM are limited to the calculation of strains, strain rates, and forces. In addition, the ability to use the same material model for both SPH particles and finite elements further underscores the appeal of coupling methods and confirms their position as a valuable asset in computational mechanics.

In this section, a subset of coupling strategies has been the subject of a critical review. A comprehensive insight into different coupling methods can be found in the work of Li and Liu [60]. In literature, the coupling of the FEM with SPH - or, more generally, with meshless methods - can be divided into two main categories: the multi-phase interactions, such as fluid-structure interactions, where the fluid is usually modeled with particles and the structure with finite elements, and the simulation of localized structural responses to impact events, where most of the structure is modeled with FEs, and only the highly deformed region is modeled with particles. In the first case, the interactions occur between two different bodies, while in the second case, the interactions occur within the same physical entity.

Attaway et al. [6] first proposed a methodology to model fluid-structure interaction by coupling SPH and FEM using a penalty-based approach. In state-of-the-art simulations, the fluid-structure interaction is usually modeled with a ”*master-slave*” coupling algorithm (also known as ”*leader-follower*” or ”*primary-secondary*”): once the contact is identified, one surface is set as the master and the other as the slave. Typically, in this case, the solid structure is defined as the master surface that controls the contact, while the fluid is considered to be the slave. At every time step, the algorithm checks for penetration of the slave particles into the structure master surfaces and assesses the reaction forces required to push the slave nodes away from the master surface [7].

For the second scenario, which corresponds to the current research interests, the SPH/FEM coupling techniques can be further divided into two main methods [72]. The first involves a transformation technique that converts finite elements into SPH particles in response to the evolving material states. The second method involves the discretization of different structural domains using SPH and FEM and is therefore based on interface contact algorithms. The two different approaches are shown in Fig. 2.6.

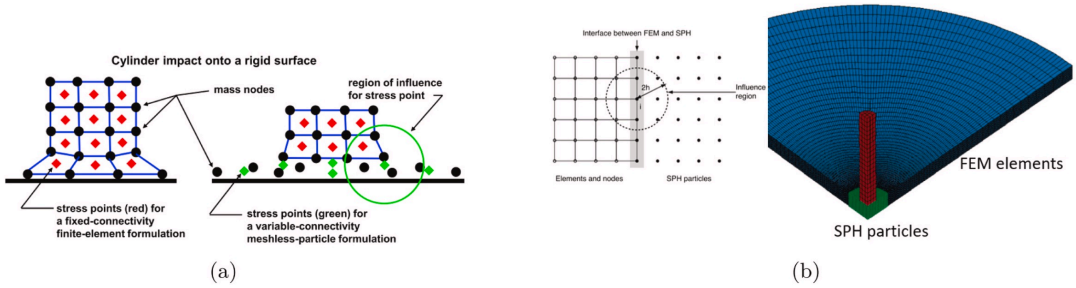

Figure 2.6: The FE-SPH coupling methods: on the left (a), the FEs are converted to SPH particles as the material progressively deforms [51]; on the right (b), different domains of the structure are modeled with SPH and FE [94].

The approach on the left, adapted from [51], first describes the entire structure with finite elements. As material deformation progresses and stress rises, these elements are transformed into SPH particles. This methodology is often referred to as *adaptive coupling*. Conversely, the strategy on the right, based on reference [94], uses SPH particles to model the central region of the target plate, which undergoes significant deformation, while the remaining structure is represented by finite elements. The projectile can be modeled through SPH particles or finite elements depending on the degree of deformation it is expected to exhibit. Indeed, finite elements are still considered sufficient for modelling areas that undergo minor deformation. The interface contact scheme in figure is only an example. Several types of SPH-FEM interfaces have been proposed. In the following sections, first the adaptive and then the interface coupling methods are discussed.

Adaptive coupling - The adaptive coupling of FEM with SPH has seen significant developments. The method is based on the replacement of FEM elements with SPH particles when critical levels of stress, strain, or other state variables are met. When a FEM element fails, it is removed and replaced by a set of pre-defined SPH particles. This substitution conserves the energy and mass of the system and mitigates the abnormal deformation that can result from altered contact surfaces. SPH particles model the broken material, which is capable of withstanding compressive stress but not tensile and shear stress, thus avoiding tensile instability within SPH formulations [39]. The adaptive coupling FEM-SPH is shown in Fig. 2.7. At the same time, the SPH algorithm, FE-particle coupling and contact algorithm cooperate to calculate the stress, strain, and other parameters of the simulation members.

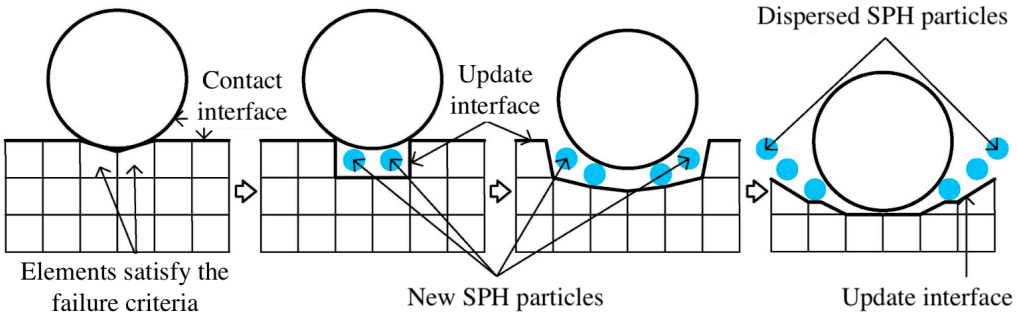

Figure 2.7: FEM-SPH adaptive method process [39].

The genesis of this adaptive strategy can be attributed to the work of Johnson et al. [49], who initially applied this approach to impact simulations. In their study, they demonstrated two con-

version techniques: one in which SPH nodes slip along a pre-existing finite element mesh, and another in which SPH nodes are autonomously generated from the mesh. Subsequent advances by Johnson et al. [52, 51], following the foundational work of Fahrenthold and Horban [28], introduced integrated particle-finite element algorithm. This hybrid approach, in which finite elements and meshless particles simultaneously model the same materials, was successfully implemented in high velocity impact scenarios, demonstrating its effectiveness in dynamic simulations.

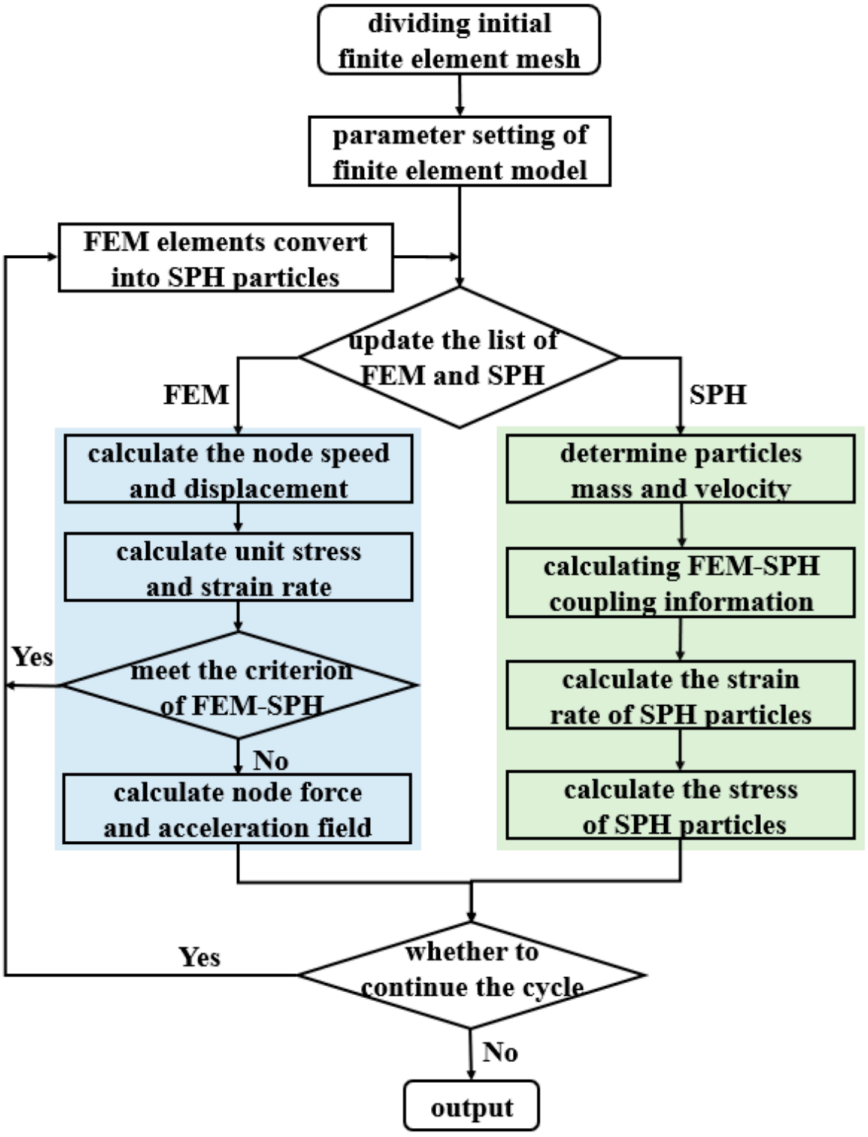

Figure 2.8: FEM-SPH adaptive coupling algorithm flow-chart [108].

The adaptive coupling algorithm follows a systematic procedure [39], summarized as follows:

1. Concurrent computation for both FEM and SPH is performed within the current time step.
2. After the computation, an evaluation against a predetermined failure criterion is performed for each element. Elements meeting this criterion are eliminated and their properties (i.e., mass, velocity, and material properties) are transferred to newly generated SPH particles occupying the same spatial coordinates.

3. These particles are then integrated into the SPH framework for subsequent computations.
4. The contact interface is updated and a contact algorithm is applied to manage the interaction between the unbroken finite elements and the SPH particles in the simulation.
5. The algorithm advances to the next time step.

Figure 2.8 visually details the basic steps of the adaptive coupling algorithm for finite elements and particles in a flow-chart format.

An increasing number of FEM elements become SPH particles as the simulation progresses. The remaining elements represent the intact portion of the structure that was not completely damaged, while the SPH particles represent the fully fragmented debris. This method exploits the strengths of FEM for mesoscale modeling and different material types, including anisotropic models, allowing the simulation of advanced materials and complex structures, such as composites and foams, that are beyond the capabilities of a sole SPH approach [39].

Interface contact coupling - To combine the computational efficiency of the FEM with the proficiency of SPH in managing large deformations, a hybrid discretization approach can be employed. This entails partitioning the problem space, denoted by Ω, into two distinct domains: Ω_{FEM} is tackled using finite element methods, while Ω_{SPH} is tackled through a meshless particle framework, as shown in Fig. 2.9 (left).

The coupling of SPH and FEM is realized by an interface contact algorithm, which enforces an interface constraint to ensure coherent solutions along the boundary shared by the two domains, symbolized by $\Gamma_{Interface} = \Omega_{FEM} \cap \Omega_{SPH}$.

At this juncture, the particles are constrained and move synchronously with the elements. It is crucial to ensure consistency in displacement, velocity, and stress throughout the interface for the physical accuracy of the simulation [21]. As shown in Fig. 2.9 (right), the random particle "i" is influenced by both finite elements and SPH particles within its support domain, which is defined by the smoothing length h. To maintain the simulation's integrity, it is necessary to utilize advanced computational techniques to determine particle properties at the interface and to maintain the continuity required.

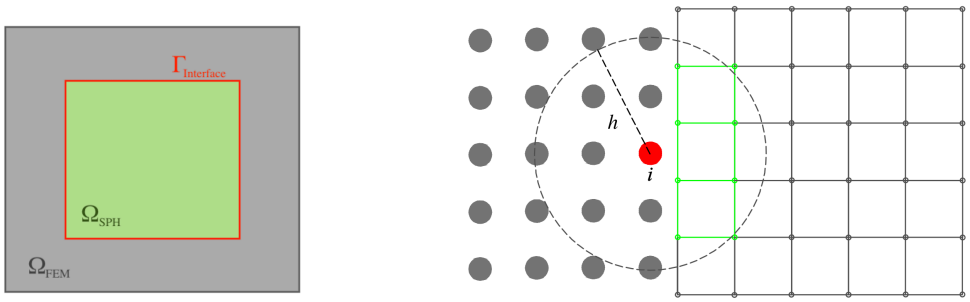

Figure 2.9: FEM-SPH interface contact coupling domain discretization example: (left) domain discretization, (right) interface detail [21].

The development of an interface coupling algorithm that efficiently bridges FEM and MM pre-

cedes the adaptive approach and offers a wide range of applicability beyond addressing issues of high deformation and computational load. This methodology is useful in simulating phenomena at atomic and multi-scale levels, making it a versatile tool in computational modeling [9, 98].

Over the past three decades, the scientific community has seen the emergence of several contact algorithms designed to facilitate interactions at FE-meshless interfaces. Although they have been developed for different meshless techniques, these algorithms are versatile in the sense that they can be adapted to work with SPH.

A selection of noteworthy interface coupling strategies are discussed in this section. For a comprehensive analysis of these methodologies, readers are directed to consult Li and Liu's comprehensive text on the subject [60].

In 1994, Johnson [49] presented a pioneering method for coupling the SPH and FEM domains. His model anchors particles to finite element nodes, allowing for a strong and continuous transfer of both tensile and shear forces across the SPH-FEM interface. This was achieved by combining the forces on the FE nodes (F_{FEM}) with those on the particles (F_P), along with their masses, to derive a unified calculation of acceleration as shown in Eq. (2.36).

$$a_{FEM,coupling} = a_{P,coupling} = \frac{F_{FEM} + F_P}{m_{FEM} + m_P} \tag{2.36}$$

The relevant forces are calculated according to:

$$F_{FEM} = m_{FEM}\, a_{FEM}, \qquad F_P = m_P\, a_P \tag{2.37}$$

However, this method has a notable drawback: it requires a one-to-one correspondence between the particles and nodes [83]. Therefore, this coupling mechanism cannot be applied universally to any arbitrary particle distribution.

For this reason, a recent study [83] proposed a new algorithm based on *slave-master coupling* to couple particles to elements in a way that allows arbitrary nodal arrangements. In fact, this new method does not retrieve particle quantities through simply imposing equality between nodes and particles and therefore forcing a certain nodal arrangement, but by exploiting a stiffness assumption and thus the rigid body laws of motion between the two domains.

The master-slave algorithm is employed to obtain particle properties. Since the particle is considered a slave node that follows the motion of the master node, in this application the FE, its properties at any time can be expressed in terms of the properties of the FE nodes, using the coordinates of the particle projection on the nearest element to weight the relative influence.

Subsequently, in 1995 Liu et al. [63] showed how to couple the Reproducing Kernel Particle Method (RKPM) with FEM by modifying the shape functions in the transition area for both RKPM and FEM. They applied the reproducing condition also in the transition area.

In 1995, Belytschko et al. [8] formulated a coupling technique for the Element-Free Galerkin

(EFG) method with FEM using mixed interpolation within the transition domain. This method replaces the finite element nodes with particles and interconnects them smoothly to the EFG nodes using a ramp function to ensure continuity and consistency at the interface. Figure 2.10 providing a clear depiction of this coupling methodology.

Here, the particle domain is represented by Ω_{SPH}, the element domain is represented by Ω_{FEM}, and the transition region is denoted by Ω_B. The element boundary and particle boundary are represented by Γ_{FEM} and Γ_{SPH}, respectively.

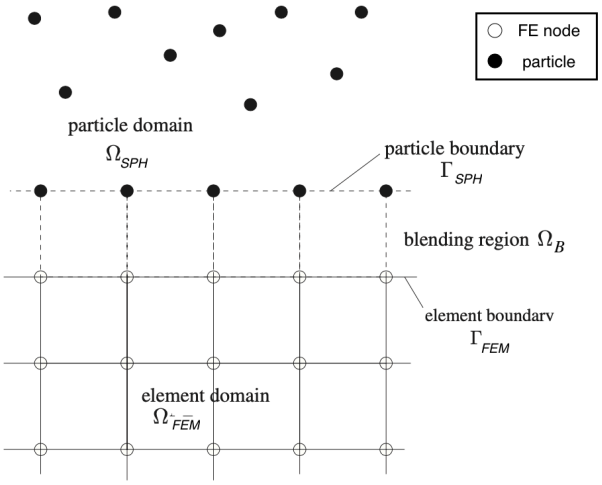

Figure 2.10: FEM-SPH interface contact coupling via ramp functions [83].

In the interface region, an approximation of the displacement vector u, is given by:

$$u = u_{FEM}(x) + R(x)(u_{SPH}(x) - u_{FEM}(x)) \qquad \forall x \in \Omega_B \tag{2.38}$$

Here, u_{FEM} and u_{SPH} are the FE and particle approximations for u in the transition region and $R(x)$ is the so-called ramp function. Although several formulations of the ramp function exist in the literature [8], the main feature is that it must be constructed in such a way as to ensure continuity, and thus:

$$R(x) = 0 \qquad \forall\, x \in \Gamma_{FEM}, \tag{2.39}$$

$$0 \leq R(x) \leq 1 \qquad \forall\, x \in \Omega_B, \tag{2.40}$$

$$R(x) = 1 \qquad \forall\, x \in \Gamma_{SPH} \tag{2.41}$$

For example, in [83] the ramp function is defined as follows:

$$R(X) = 3r^2(x) - 2r^3(x) \tag{2.42}$$

with

$$r(x) = \sum_{i \in \Gamma_{SPH}} N_i(x) \tag{2.43}$$

Where $N_i(x)$ is the shape function of the $i-th$ particle evaluated at x.

The drawback of this method is that the derivatives along the interface are discontinuous [8]. Fortunately, in 2000, Huerta et al. [44] were able to remove this disadvantage developing an upgraded ramp function.

In 2004, Belytschko and Xiao [9] introduced the '*bridging domain coupling method*', a technique designed to enhance the interface between finite elements and particles for atomistic and multiscale simulations. This method represents a significant improvement over the original '*hand-shake*' model introduced by Abraham et al. in 1998 [1].

Two main components of this approach are the use of Lagrange multipliers and the Augmented Lagrangian method to enforce motion constraints. The system is structured so that the Lagrange multiplier field gradually decreases to zero at the boundary of the FEM domain, ensuring smooth force interactions between the FE and particle domains. A visual representation of this coupling method is shown in Fig. 2.11.

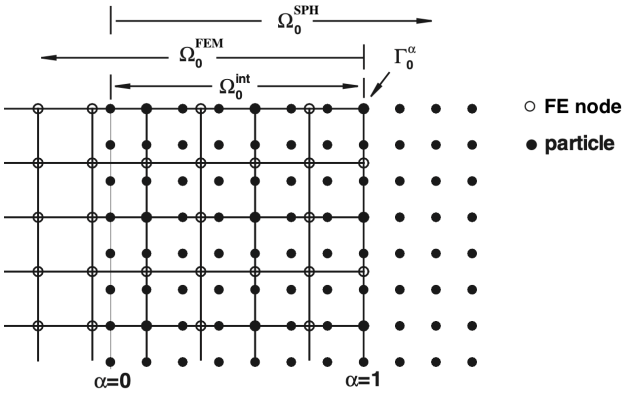

Figure 2.11: FEM-SPH interface contact coupling via bridging domain [83].

Compared to Fig. 2.9 (left), the model introduces an overlapping domain named Ω^{int} where the FEM and particle subdomains intersect. Within this region the scaling parameter α is introduced, with a value of one at the border of the finite element domain Γ^{α} and gradually decaying to zero towards the other end of the intersection domain Ω^{int}. The subscript '0' marks the parameters at the initial state.

In the region Ω_0^{int}, the system displacements can be approximated by the shape functions $N_I(x)$ of FEM or the kernel functions $w_I(x)$ of particle methods:

$$u_{FEM}(x,t) = \sum_I N_I(x)\, u_{FEM,I}(t), \tag{2.44}$$

$$u_{SPH}(x,t) = \sum_I w_I(x)\, u_{SPH,I}(t) \tag{2.45}$$

Therefore, the displacements constraint condition in Ω_0^{int} at the discrete position of particles is:

$$g_I = g_{iI} = u_{FEM,iI} - u_{SPH,iI} = \left\{ \sum_J N_{JI} u_{FEM,iJ} - \sum_K w_{KI} u_{SPH,iK} \right\} \tag{2.46}$$

According to the *Lagrange multiplier method*, the problem can be reduced to finding the station-

ary point of the energy function W_L, as expressed in the following equation:

$$W_L = W^{int} - W^{ext} + \lambda^T g \tag{2.47}$$

Where λ is the vector of Lagrange multipliers λ_i for the constrain g_i for each of the particles. W^{int} and W^{ext} represents respectively the total internal and external potential energy of the system.

The total internal potential energy W^{int} can be expressed as follow:

$$W^{int} = \int_{\Omega_0^{FEM}} \beta^{FEM} F^T \cdot P \, d\Omega_0^{FEM} + \int_{\Omega_0^{SPH}} \beta^{SPH} F^T \cdot P \, d\Omega_0^{SPH} \tag{2.48}$$

where F^T is the transpose of the deformation gradient, P the nominal stress tensor and β the scaling parameter defined in Eqs. (2.50).

On the other hand, the total external potential energy W^{ext} can be expressed as follow:

$$\begin{aligned} W^{ext} = \int_{\Omega_0^{FEM}} \beta^{FEM} \rho_0 b \cdot u \, d\Omega_0^{FEM} + \int_{\Omega_0^{SPH}} \beta^{SPH} \rho_0 b \cdot u \, d\Omega_0^{SPH} + \dots \\ \cdots + \int_{\Gamma_0^{FEM}} \beta^{FEM} \bar{t} \cdot u \, d\Gamma_0^{FEM} + \int_{\Gamma_0^{SPH}} \beta^{SPH} \bar{t} \cdot u \, d\Gamma_0^{SPH} \end{aligned} \tag{2.49}$$

where ρ_0 is the initial density, b are the body forces per unit mass, $\bar{t}$ are the prescribed boundary traction defined positive outward, and u the displacements vector. The scaling parameter is defined as:

$$\beta^{FEM}(x) = \begin{cases} 0 & \text{in} \quad \Omega_0^{SPH} \\ 1-\alpha & \text{in} \quad \Omega_0^{int} \\ 1 & \text{in} \quad \Omega_0^{FEM} - \Omega_0^{SPH} \end{cases} \tag{2.50}$$

$$\beta^{SPH}(x) = \begin{cases} 0 & \text{in} \quad \Omega_0^{FEM} \\ \alpha & \text{in} \quad \Omega_0^{int} \\ 1 & \text{in} \quad \Omega_0^{SPH} - \Omega_0^{int} \end{cases} \tag{2.51}$$

In the same work, Belytschko and Xiao also proposed an Augmented Lagrangian methods for a better numerical stability. The Augmented Lagrangian methods can be developed by adding a penalty term to Eq. (2.47), as follows:

$$W_{AL} = W^{int} - W^{ext} + \lambda^T g + \frac{1}{2} p g^T g \tag{2.52}$$

where p is the penalty parameter; if $p = 0$, Eq. (2.52) is identical to Eq. (2.47).

To develop the corresponding discrete equations the Lagrange multiplier field must be expressed in terms of shape functions denoted by $\Lambda_I(x)$:

$$\lambda_i(x,t) = \sum_I \Lambda_i(x) \bar{\lambda}_{iI}(t) \tag{2.53}$$

Generally, the shape functions for the Lagrange multiplier field $\Lambda_I(x)$ are different from that used for the displacement, $N_I(x)$ or $w_I(x)$. To distinguish the Lagrange multiplier field λ_I in Eq. (2.53) for the constrain g_I in Eq. (2.46), $\bar{\lambda}_{iI}$ is denoted as the unknown Lagrange multiplier at the Lagrange multiplier nodes.

The discrete equations are then obtained by inserting Eqs. (2.44), (2.45) and (2.53) into Eq. (2.52) and setting the derivatives of W_{AL} with respect to u_I and λ_I to zero. The reader is referred to [9] for further details and to [83] for the dynamic extension.

Working on the total Hamiltonian of the system and enforcing displacement constrain as shown above, Xu and Belytschko in [104], developed a less computationally demanding coupling by diagonalization of the Lagrange multiplier constraints. Although the efficiency, the new implemented form results in loss of energy conservation property.

In conclusion, in 2007 by Zhang et al. [107], a faster formulation of the bridging domain coupling method has been developed for the case where the continuum domain can be treated as linear elastic.

2.3. Shock Wave Induced by HVI

In the coming decade, scientific satellites with significant advancements in required measurement precision, such as *Sentinel-1C* and *Sentinel-2C*, will be launched. Consequently, it is imperative to develop exceptionally stable platforms. As already implemented in the ESA's *Global Astrometric Interferometer for Astrophysics* (GAIA) [97] and the *Gravity field and steady-state Ocean Circulation Explorer* (GOCE) [79] satellites, sandwich panels composed of carbon fiber reinforced plastic and aluminum honeycomb cores are expected to be the preferred configuration for these platforms, offering superior structural advantages such as high specific stiffness and minimal thermal expansion.

In this scenario, the risk of micro-meteoroids and space debris impacts cannot be neglected. These impacts are comparable in effect to the shock caused by explosive devices [79], making them a credible hazard to the ultra-high sensitivity on-board equipment requirements. Satellites, especially *Sentinel-1A* or *Sentinel-2A*, which execute numerous avoidance maneuvers annually due to continuous potential impact detections, are particularly concerned with the transient disturbances caused by such collisions. These disruptions can jeopardize the precision of measurements by undermining the integrity of vital stability regions, thereby hindering the achievement of mission objectives.

As mentioned, a high-amplitude shock wave hitting the impact point causes local plastic deformation (i.e., craters) that attenuates significantly as it moves into the surrounding structure, transforming it into an elastic wave. The impact results in a single pulse in the direction of the projectile's trajectory in the spacecraft wall, with a peak velocity comparable to that of the impacting projectile itself [87].

Ground-based experiments often cannot accurately reproduce such HVI conditions. For exam-

ple, the *GAIA* mission, operating in a Lissajous orbit around the Earth-Sun L2 point, faces a primary debris field of micro-sized particles with velocities exceeding 20 km/s [87]. Such a scenario is currently impossible to reproduce experimentally. Therefore, numerical simulations are essential to characterize the structural response to these impacts. Although FEM tools are generally preferred for the assessment of structural responses to different loads, their application in this context is limited due to the large size mismatch between the satellite and typical impacting bodies (m compared to mm) and the inability of the numerical model to cope with extreme high loading and high deformation events, requiring alternative simulation strategies.

The primary goal of experimental and numerical impact testing campaigns is to investigate the wave propagation in spacecraft structures after impact events. These studies are also concerned with the effects of various parameters, particularly the properties of the materials involved and the characteristics of the projectiles, on the resultant vibrations and structural integrity. In general, it has been observed from lower velocity experimental impact tests that the high-frequency content is quickly damped when transmitted to the interconnected structure [79]. Therefore, the focus is on the transmission of low-frequency content, which is the primary source of instability in space vehicles.

2.3.1. Numerical Models and Preliminary Results

From the point of view of the spacecraft dynamics, non-catastrophic hyper-velocity impacts are categorized on the basis of their severity and their frequency [79]. Frequent, but low-intensity, impacts can cause a continuous degradation in the accuracy of scientific data due to their noise-like effect on the spacecraft's dynamic environment. These are generally caused by particles colliding with the spacecraft more than once per hour. Intermediate-intensity shocks occur less frequently but may temporarily interrupt data collection due to the magnitude of the disturbance relative to the sensitivity of the on-board instruments. Such impacts are associated with particles hitting the spacecraft at intervals ranging from daily to monthly. Finally, rare but high-intensity impacts pose a risk of at least temporary loss of spacecraft attitude control, occurring at a rate of less than one per year.

Simulations of HVI induced vibrations on spacecraft have utilized two distinct methodologies. The first method involves generating an excitation signal from a simulation of a spacecraft wall impacted by debris, which is then used as input for finite element analyses to assess vibration responses at various impact points [87, 32]. Conversely, the second method does not distinguish between local impact effects and the overall dynamic response; it attempts to model the entire system as a single entity into one simulation procedure [32].

In both strategies, effective modeling necessitates that the modal truncation should be large enough to account for the main structural frequency responses. Moreover, the area of impact must be sufficiently detailed to absorb the frequency content of the applied load [97].

The second approach employs SPH to retrieve the force impulse exerted on the structure around the impact zone, and then transfer the information to a couple finite element model to analyze the whole structural vibrational response. Despite SPH showing promise in calculating induced vibrations from an HVI, the significant computational demands and the complexities involved in

integrating SPH with FEM currently limit its practicality [32].

On the other hand, the objective of the first technique is to obtain a preliminary but realistic estimate of the HVI-induced force at the impact site. Two methods have been implemented to calculate the equivalent force impulse applied by the projectile on the target [32]. The first method involves monitoring undamaged sections at various distances from the impact site. The disturbances in these sections are purely elastic, and the progression of these waves can be traced to define the initial elastic excitation at the impact site. The second method involves evaluating the total momentum transferred to the target. Although the former provides detailed insight, it is hampered by the complexity of the stress wave environment and the computational demands of using large targets to avoid boundary reflections. The second method, although less detailed, offers a broader overview without providing the specific force peak shape. By varying conditions such as projectile size and velocity, it is possible to establish a general elastic-equivalent excitation function for a given structure subjected to HVI.

The complexity increases significantly when attempting to estimate the force transferred by impacting sandwich panels commonly used in modern satellites. The design of these panels often results in the projectile's energy being predominantly absorbed by either the front or back panel, depending on the specific conditions of the impact. Vergniaud et al. [97] have established a criterion, derived from experimental data and projectile momentum, denoted P_p, which determines whether the force should be applied to the front or rear sheet of the sandwich panel.

For sandwich panels with a 20 mm aluminum Honeycomb Core (HC) and Carbon Fiber Reinforced Plastic (CFRP) skins of 0.5 mm thickness, a threshold has been set: if P_p is less than 1.82 g m/s, the force should be applied to the front skin. Conversely, when P_p exceeds this threshold and significant penetration of the front face sheet has been achieved, the back sheet should be considered the primary site of excitation and the force should be applied accordingly [97]. This distinction is critical for accurate simulation and analysis of impact dynamics on satellite structures.

The validation of simulation models used to assess the impact of micro-meteoroids and space debris on satellite structures has been partly established through experimental testing. These tests, however, faced challenges in isolating the vibration signals induced by the impact from those related to the test equipment itself, such as the light-gas gun. Detailed information on these experimental setups is provided in Ref. [79].

An illustrative comparison shown in Fig. 2.12 juxtaposes the experimentally retrieved with the numerically evaluated vibration signal at 150 mm offset from the shot axis. On the left side, the graph is related to a 2 mm thick Al 7075-T6 plate impacted by a 2.0 mm Al-sphere at 5.3 km/s, while, on the right side, the plot is related to a CFRP/Al HC Single Plate impacted by 1.5 mm Al-sphere at 5.69 km/s [86]. The comparison exhibits a good qualitative congruence for both scenarios, capturing the initial high-frequency disturbance and the subsequent low-frequency oscillations. However, the numerical simulation of the vibration environment necessitates extensive computational resources to attain the frequency resolution required for an effective comparison with experimental and finite element analysis data.

The waveform from these disturbances can be categorized into three phases: longitudinal (1), shear (2), and flexural (3) waves [86]. While these phases are distinctly identifiable in metallic targets (Fig. 2.12 left), they are less distinct in composite sandwich panels (Fig. 2.12 right). The flexural wave, essential in quantifying impact-induced disturbances, is discernible around 50 μs in aluminum plate and around 35 μs in composite honeycomb post-impact.

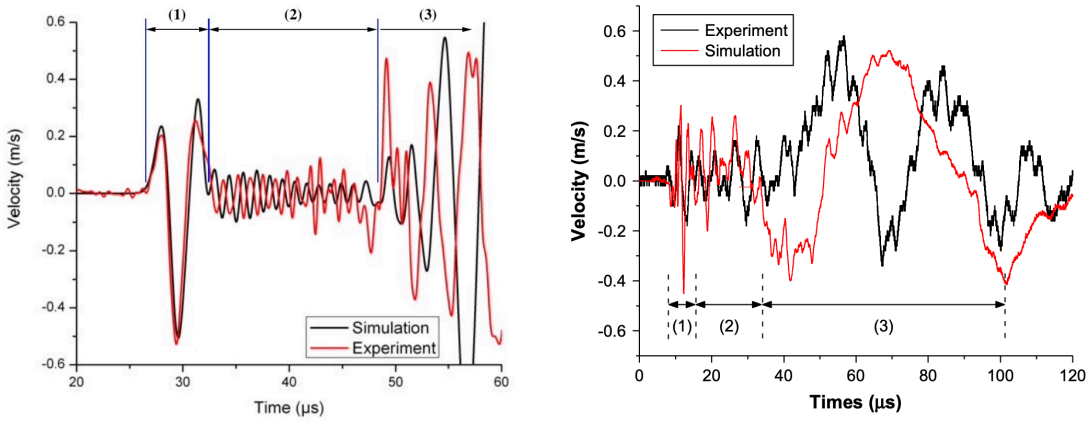

Figure 2.12: Comparison of experimental and numerical disturbance waveform at 150 mm from normal impact in (left) a 2 mm thick Al 7075-T6 plate measured with 2.0 mm Al-sphere at 5.3 km/s, and (right) a CFRP/Al HC SP with 1.5 mm Al-sphere at 5.69 km/s [86]. Sections of longitudinal (1), shear (2) and flexural (3) waves are marked.

2.4. Literature Review Conclusion

The objective of this *literature review* has been to provide a reliable understanding of the risk associated with the increasing density of space debris population in LEO and the associated threat of HVI to satellite functionality, with a particular focus on the available simulation tools. Now, the reader is aware of the growing risks posed by hyper-velocity MMOD impacts, the limitations of both the experimental research, due to high cost and complex procedures, and the numerical models, due to low level of adaptability, high computational time and complex implementations.

HVIs pose multifaceted challenges to satellites, ranging from threat to accuracy of measurements to overall survivability of the system. The review of relevant literature reveals a research gap in the integration of Smoothed Particle Hydrodynamics and Finite Element Method techniques to characterize the structural response of satellites to HVIs in regard to vibration and stress propagation. This research has first gone through a detailed description of the physical aspects related to this phenomenon and the mathematical modeling of the behavior of the involved materials (i.e. description of material constitutive models, failure criteria and equations of state).

In this review, the dominant numerical models, namely FEM and SPH, were discussed. Their respective strengths and weaknesses were pointed out. FEM was found to be computationally efficient but lacks robustness in representing severe deformations, while SPH provides an accurate representation of high-stress and high-deformation events at the expense of increased computational requirements. Therefore, a sole reliance on either method is considered insuf-

ficient for the objectives of this thesis. A comprehensive review of coupling methods between meshless techniques and FEM has been conducted, filtering out those most relevant to the goals of the thesis and categorizing them into three primary schemes: adaptive coupling, edge-to-edge interface coupling, and bridging domain interface coupling. The advantages and limitations of each have been delineated.

Although there are studies on the shock wave effects induced by HVI, an integrative application of FEM and SPH remains to be developed. This gap is currently addressed by detecting an acceleration wave from experimental analysis at a certain distance from the impact site and reconstructing it back to apply the digital acceleration signal to the spacecraft finite element model to retrieve the global structural behavior. The conclusion of this review anticipates that the successful integration of SPH and FEM methodologies will not only enhance the understanding of HVI phenomena, but will also inform the design strategies necessary to mitigate the associated risks.

3

Simulation Methodology for Single-Plate Hyper-Velocity Impacts

The chapter delineates the methodological framework employed for simulating HVI on a single-plate configuration. This section explains the iterative process undertaken and the reasons behind the adoption of certain models over others. Specifically, it evaluates the influence of the shape of SPH domain, its initial spatial lattice configuration, and the algorithm employed for SPH/FEM coupling, on the degree of realism and accuracy of the simulations. To validate and compare this novel simulation approach, the implemented models replicate the experimental test conducted by Sibeaud et al. [88]. This facilitates both qualitative and quantitative assessments of the model modification. Beyond merely comparing post-impact geometrical parameters, the evaluation encompasses an energy analysis and an exploration of stress-wave internal reflections.

Initially, exploiting the model symmetry, a quarter model of the experimental setup has been proposed, followed by the development and analysis of a full plate and impactor model. In Chapter 4, the simulation modeling technique that most faithfully reproduces the reference test is subsequently adapted to a double-wall configuration, also known as Whipple shield or Whipple bumper, and the simulation outcomes are compared with experimental data of tests conducted by the European Space Agency (ESA), courtesy of courtesy of Airbus Defence and Space.

The dataset collected during these experiments is exhaustive and applicable to a diverse array of scenarios, providing valuable insights into induced vibrations and enhancing understanding within the domain of HVI simulations.

All the computations in this chapter are performed with the LS-DYNA R13.0.1 MPP Single Precision version in the High Performance Computing cluster of the Delft University of Technology Aerospace Faculty (HPC12).

3.1. Reference Test

The research conducted by Sibeaud et al. [88] at the Centre d'Études de Gramat (CEG) was chosen for replication due to the clarity in the presentation of the experimentally collected measurements, which are stated to be accurate to within 1%. Additionally, the recent extensive numerical investigation proposed within Legaud et al.'s paper, titled "*Improvement of Satellite Shielding under High-Velocity Impact Using Advanced SPH Method*" [59] further supports the decision to replicate this research. Combining experimental and numerical methods, the study provides comprehensive results and clarity of model inputs.

Legaud's study aimed to enhance hyper-velocity simulation capabilities and reliability through a sensitivity analysis of three main parameters: the number of particles through the thickness of the plate, the SPH formulation, and the particle pressure cut-off. The investigation aimed to determine their respective influences on computational accuracy and performance.

In this report, the experimental test n.3 from the work of Sibeaud et al. has been reproduced. The test consisted of a 5 mm radius spherical projectile made of aluminum alloy Al 2017 shot onto a 2 mm thick, 150 mm square plate made of aluminum alloy Al 6061-T6 at normal incidence with a measured velocity of 5941 m/s.

The investigation that follows evaluates the discrepancies between the experimental and numerical models in order to evaluate and compare different simulation settings. The following parameters were measured and used as benchmarks: final crater radius, debris cloud length, maximum cloud radius, and axial velocity at the cloud front 16 µs after impact.

The experimental data collected during the test are presented in Table 3.1:

Crater Radius (*final*) [mm]	**Front Cloud Velocity** (*16 µs*) [m/s]	**Cloud Length** (*16 µs*) [mm]	**Cloud Max Radius** (*16 µs*) [mm]
8.45 mm	5296 m/s	81.1 mm	32.8 mm

Table 3.1: Results of the HVI experimental test [88]

In this section of the thesis, the focus was on selecting the optimal SPH domain shape and SPH/FEM interface algorithm that would allow for the most accurate numerical reproduction of HVI in space. Both square and circular SPH domain shapes were tested, and two SPH/FEM interface algorithms were evaluated: "*tied contact*" and "*adaptive contact*".

On the one hand, the effect of different SPH domain shapes (square and circular) on the propagation of information from one domain to the other was assessed. The objective was to determine the influence exerted by the interface geometry and interface geometrical discontinuity on proper propagation of information. On the other hand, different SPH/FEM interface options were tested to ascertain whether an algorithm performs more effectively than another. The tied contact between the SPH and FE parts enforces a kinematic constraint at the interface, ensuring coherent solutions along the boundary. The adaptive contact introduces a transition domain comprising hybrid SPH/FEM elements. The approach remains based on kinematic constraints, yet ensures

a more seamless transition from the SPH to the FE domain due to the dual nature of the transition area. The contacts are respectively described in detail in Sections 3.2.2 and 3.2.3.

To properly capture the specific effect of the SPH domain shape and the interface algorithm used, all four possible cross configurations were tested. In order to provide the reader with a comprehensive and clear view of the next sections, the different test settings are summarized in Table 3.2:

	Tied Contact	**Adaptive Contact**
Square impact domain	Reference Test	Square domain with adaptive contact
Circular impact domain	Circular domain with tied contact	Circular domain with adaptive contact

Table 3.2: Combination table of the implemented numerical tests.

3.2. Quarter Plate Model

To reduce computational costs, the decision was made to numerically replicate only a quarter of the experimental test. Therefore, the dimensions of the modeled plate were set to [75 mm, 75 mm, 2 mm], and a quarter slice of the spherical projectile was employed in the simulation. The boundary conditions consisted of two symmetry planes aligned along the x and y axes, while the external edges of the plate were clamped. For a visual representation of the simulation geometry, see Fig. 3.1. The blue region represents the SPH plate impact domain, the red portion represents the rest of the plate, and the green region represents the projectile. To implement symmetry planes in LS-DYNA, the keywords ***BOUNDARY_SPC_SET** for solid elements and ***BOUNDARY_SPH_SYMMETRY_PLANE** for SPH particles are used.

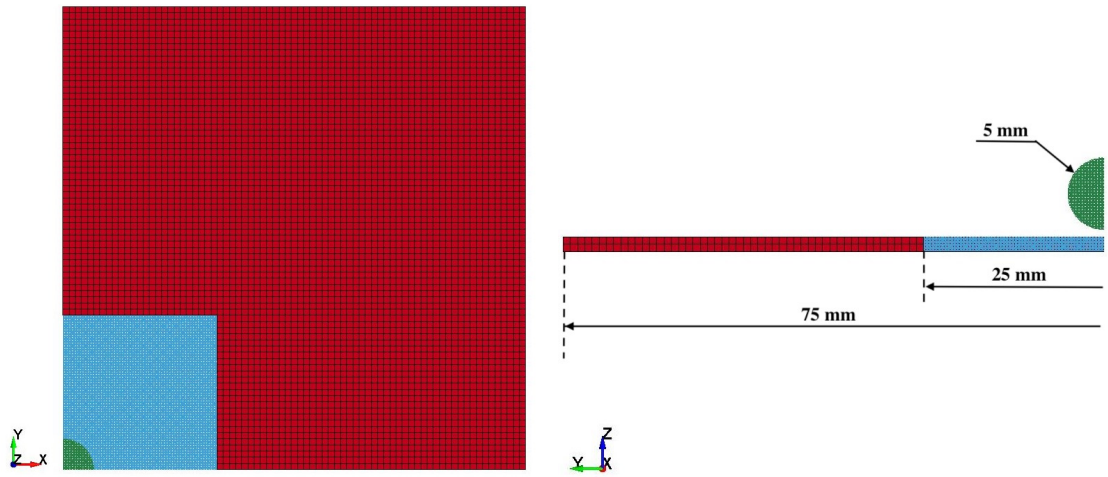

Figure 3.1: Geometry of the reference test simulation (top and lateral view - pictures from LS-DYNA Pre-Post V4.8).

The following subsections describe the most relevant numerical aspects of the simulation model and discuss the two types of contact implemented: tied contact and adaptive contact.

3.2.1. Model Parameters

This section covers the most important LS-DYNA keywords that are common to all simulations introduced in Chapter 3. For further information, please refer to Appendix A.

The control settings applied to the SPH particles play a central role in determining the stability, accuracy, and efficiency of the simulation by defining the particle interactions. In all the presented simulations, a ***CONTROL_SPH** card was used to manage SPH particle properties, including the activation of a particle deactivation box. This box effectively deactivates SPH particles that have gone outside the box and are no longer interacting with the structure, optimizing computational efficiency while capturing key impact features such as the evolving debris cloud and ejecta veil.

The SPH control algorithm dynamically adjust the number of neighbors per particle during the computation, significantly exceeding the default value of 150. LS-DYNA's automatic adjustment of this value allowed the simulation to proceed to the final stages. If the number of neighbors per particle increases too much, the automatic process of neighbor determination leads to a program crash, so that it is necessary to update the initial default value.

Regarding the SPH formulation, Legaud et al. [59] concluded that the default SPH formulation is optimal for hyper-velocity impacts. The *CONTROL_SPH settings further define the inter-particle interaction. The default "particle approximation" is used. According to this setting, particles of two different parts interact with the same mechanics as particles of the same part interact internally, ensuring accurate collision detection and debris cloud dynamics.

Artificial viscosity played a key role in addressing discontinuities and preventing tensile instability. The choice of the Monaghan formulation over the standard solid-element artificial viscosity formulation proved to be more widely applicable due to the complex nature of the impact zones, as the solid-structure approximation fell short. Finally, incremental stabilization was implemented as total stabilization is only recommended for hyperelastic materials.

In addition, ***SECTION_SPH** card settings were used to control the SPH smoothing function and the smoothing length constant. The use of an initial value of 1.2, bounded between 0.2 and 1.5 during the simulation, allowed for effective control of the particle dynamics. The cubic spline function was implemented as the kernel function of choice.

The plate area surrounding the impact zone requires the use of finite elements to limit the computational effort. For proper finite element functionality, modeling cards different from those associated with SPH must be implemented.

In this context, ***SECTION_SOLID** is used to satisfy the finite element attributes. Despite the thin composition of the bumper plate, shell elements were not considered due to the potential complications arising from their interaction with SPH. The main aspect that requires attention in the section card is the choice of the element formulation.

The constant stress solid element was chosen because of its accuracy, efficiency, and adaptabil-

ity to large deformations. However, its use requires hourglass stabilization, which is implemented through the ***CONTROL_HOURGLASS** tab. The use of the Flanagan-Belytschko viscous form type within this stabilization method proves to be suitable for very high speed scenarios. This specific viscosity type is recommended in the LS-DYNA manual and has been defined in the literature [81] as optimal for hyper-velocity simulations. A major advantage is its negligible effect on the system energy, which increases its suitability for such simulations.

The termination time of the simulation is controlled by the mandatory ***CONTROL_TERMINATION** card in LS-DYNA, which allows tunability based on the simulation objectives. For the single wall scenario, a simulation duration of 20 µs is sufficient to capture the entire event, given the initial high projectile velocity defined by the ***INITIAL_VELOCITY_GENERATION** card. No further termination criteria were specified.

While the original experimental study employed different aluminum alloys - Al 2017 for the projectile and Al 6061-T6 for the impacted plate - due to limitations in obtaining adequate Al 2017 material model data, and noting the similarity in material characteristics, both parts were modeled using data commonly associated with Al 6061-T6 aluminum alloy. Legaud et al. [59] utilized the Steinberg-Guinan material model, yet prior studies [38] revealed its insufficient accuracy. Consequently, the Johnson-Cook model was implemented. The LS-DYNA ***MAT_JOHNSON_COOK** keyword's input parameters are detailed in Table 3.3 and Table 3.4.

Material Property	Symbol	Value
Density	ρ	$2.703 \quad g/cm^3$
Elastic Modulus	E	$69 \quad GPa$
Shear Modulus	G	$27.6 \quad GPa$
Poisson's Ratio	ν	0.33
Melting Temperature	T_m	$775 \quad K$
Reference Temperature	T_0	$273 \quad K$
Specific heat	c_p	$875 \quad J/kgK$

Table 3.3: Material properties of Al 6061-T6 aluminum alloy [4, 59]

Johnson-Cook parameters	Symbol	Value
Yield Stress	A	$324.1 \quad MPa$
Strain Hardening parameter	B	$113.8 \quad MPa$
Strain Hardening exponent	n	0.42
Strain Rate parameter	C	0.002
Thermal Softening exponent	m	1.34
Pressure Cut-off	σ_p	$-1200 \quad MPa$
Spall type	$SPALL$	2.0
Damage Constant 1	D_1	-0.77
Damage Constant 2	D_2	1.45
Damage Constant 3	D_3	-0.47
Damage Constant 4	D_4	0
Damage Constant 5	D_5	1.6

Table 3.4: Johnson-Cook material model parameters for Al 6061-T6 aluminum alloy [91, 59].

LS-DYNA provides several spalling models to represent material splitting, cracking and failure under tensile loading. In this scenario, the material physically spalls when $\sigma_{max} \geq -\sigma_p$. Once spalled, the tensile stresses are reset to zero while allowing the material to withstand compressive stresses. The maximum principal stress spalling model, selected by setting SPALL to 2.0, detects spalling when the maximum principal stress, σ_{max}, exceeds the limit. The deviatoric stresses of the spalled material are nullified, so that hydrostatic stresses are not allowed, and all calculated tensile pressures within the spalled material are reset to zero, allowing the material to behave like debris.

The Johnson-Cook material model requires an equation of state. The Grüneisen EOS has been implemented using the LS-DYNA keyword ***EOS_GRUNEISEN**. The related parameters are presented in Table 3.5.

Grüneisen parameters	Symbol	Value
EOS Constant 0	C	$5328 \quad m/s$
EOS Constant 1	S_1	1.4
EOS Constant 2	S_2	0
EOS Constant 3	S_3	0
Grüneisen parameter	Γ_0	1.97
A factor	A	0.48

Table 3.5: Grüneisen EOS parameters for Al 6061-T6 aluminum alloy [59]

3.2.2. Tied Contact

The initial contact methodology adopted between the SPH and FEM plate components is established through a tied contact system, which functions as a constraint-based mechanism. The kinematic constraint is set between the nodes of one component and the segments of the other.

The ***CONTACT_TIED_NODES_TO_SURFACE** keyword is used to implement the connection between components by defining the contact slave set as the external SPH nodes bordering the finite elements model of the plate's external zone, and the master set as the segment set of finite elements faces within the plate model's external zone that share borders with the internal SPH plate domain. This configuration creates a tied linkage, restricting the elements and nodes translational degrees of freedom [36].

Under these tied contact conditions, the movement of slave nodes mirrors the motion of the master surface. During simulation initialization, each slave node is aligned with the nearest master segment through an orthogonal projection. Criteria are established to determine proximity, and if met, the slave nodes are adjusted to conform to the master surface without introducing stresses, allowing for minor geometric adaptations.

A warning message is logged in the output text file if nodes are deemed too distant from their corresponding master segments, indicating the absence of a tied connection. Throughout the simulation, the position of the slave node remains fixed in relation to its assigned master segment, upheld through kinematic constraint equations.

Exploiting this coupling method, two simulations have been implemented using first a square and then a circular SPH domain (Table 3.2). The square SPH domain with tied contact test corresponds to the reference test already implemented within the paper of Legaud et al. [59] and within the Master's thesis of Harazim [38]. A mesh convergence study has already been performed [38], for this reason it has been omitted. The geometry of the square SPH domain with tied contact simulation - or reference test - is shown in Fig. 3.1, while the geometry of the circular SPH domain with tied contact is shown in Fig. 3.2.

Although it may seem unconventional to study the effect of a hypervelocity impact on a circular-shaped plate, given that the classical configuration of current satellites involves square-shaped plates (which may also exhibit curvatures), this choice was adopted to simplify modeling by using the circular-shaped SPH domain. However, this simplification was later abandoned in the advanced stages of the study. As outlined in Chapter 4, although the SPH domain maintains a circular shape, it is embedded in a plate of square geometry.

The author notes that the objective of the study is to identify the optimal methodology for the transfer of stress waves and vibrations induced by hypervelocity impact in a generic flat plate of isotropic material, rather than in a specific configuration. It is assumed that such transfer, at least in the instants immediately following impact, is not affected by the general geometry of the plate, but only by local model design properties, such as the coupling algorithm and the geometry of the interface itself.

In both simulation scenarios, the projectile is modeled as a quarter of a sphere with a radius of 5 mm. The plate has a complete straight edge of 75 mm, while the SPH domain of the plate includes edges of 25 mm. To maintain consistency in both simulations, the SPH interparticle distance within both the plate impact zone and the projectile is set to 0.125 mm.

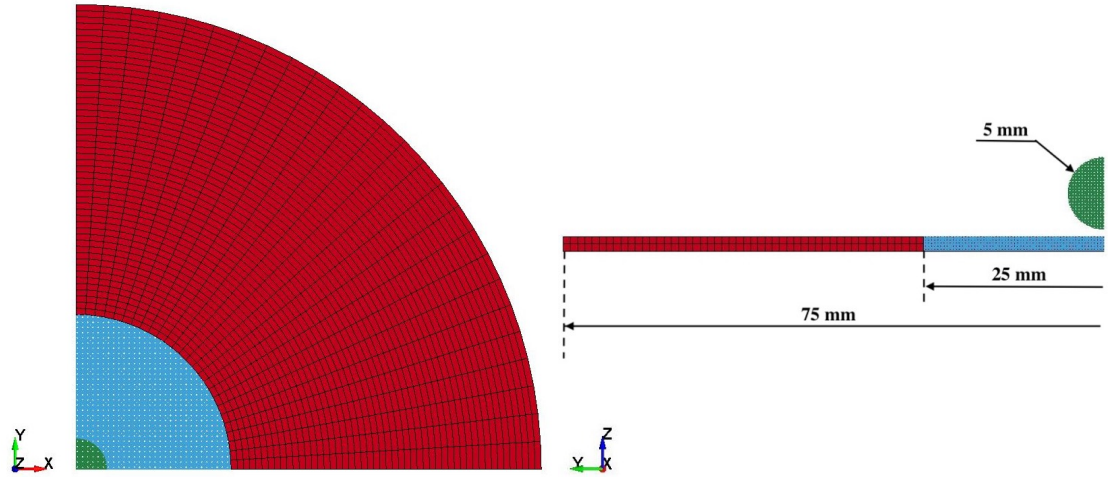

Figure 3.2: Geometry of the circular SPH domain with tied contact test simulation (top and lateral view - pictures from LS-DYNA Pre-Post V4.8).

Each scenario uses a projectile consisting of 67,024 particles. The simulation of the square domain includes a plate impact domain with 640,000 particles and 10,000 solid elements. The circular domain simulation, on the other hand, uses 502,416 particles and 2,600 solid elements

in its plate domain. In both scenarios, the SPH region has 16 particles within the plate thickness, while the FEM region integrates 2 elements. Both simulations were executed in parallel using 16 Massively Parallel Processing (MPP) processors. The total CPU time was 3461 seconds (57 min, 41 sec) for the square SPH domain simulation and 5181 seconds (1 h, 26 min, 21 sec) for the circular SPH domain simulation.

To validate both simulations, key metrics such as the final crater radius, the debris cloud length, its maximum radius, and the axial velocity at the cloud front 16 µs after impact are extracted. The collected values, along with their relative errors, are listed in Table 3.6. Moreover, a top view showing the crater shape is given in Fig. 3.3, while a representation in oblique view of impact evolution is displayed in Fig. 3.4. Finally, the velocity profile at 16 µs post-impact is shown in Fig. 3.5.

	Crater diameter (final)	**Debris Cloud Velocity** (16 μs)	**Debris Cloud Length** (16 μs)	**Cloud diameter** (16 μs)	**Avg.**
Experimental data	18.90 mm	5296 m/s	81.1 mm	65.6 mm	–
Square impact domain	21.36 mm (13.01 %)	5241 m/s (1.0 %)	80.7 mm (0.5 %)	67.2 mm (2.4 %)	**4.23 %**
Circular impact domain	21.37 mm (13.01 %)	5249 m/s (0.9 %)	82.2 mm (1.4 %)	66.3 mm (1.1 %)	**4.10 %**

Table 3.6: Results and relative errors of tied SPH/FEM interface simulation with a square or a circular SPH domain.

The results indicate that the circular domain exhibits a slightly better overall performance, as illustrated in the final column of the table. In fact, the simulation results diverge from the experimentally collected data to a lesser extent than the simulation performed with a square domain, with the exception of the debris cloud length. However, this difference is not conclusive due to the small variations and the challenges in precisely defining a boundary when determining the maximum diameter of the debris cloud. This ambiguity introduces subjectivity into the selection of the crater boundary particles. A more meaningful measure is the axial velocity of the debris cloud, evaluated by the average velocity of its leading edge.

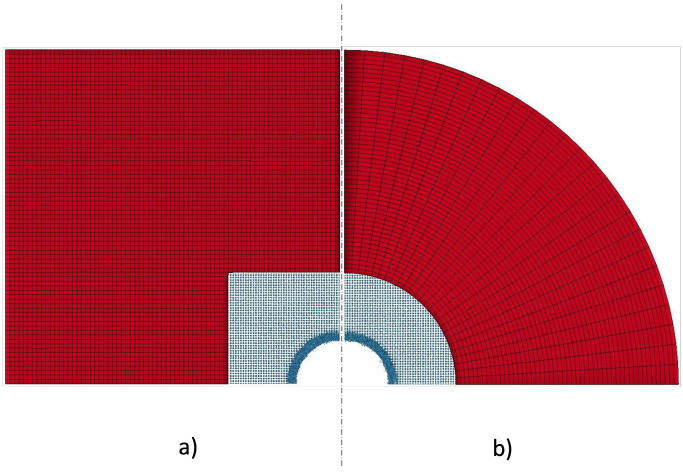

Figure 3.3: Final crater in simulation with tied SPH/FEM interface with a square (a) and a circular (b) SPH domain (top view - pictures from LS-DYNA Pre-Post V4.8).

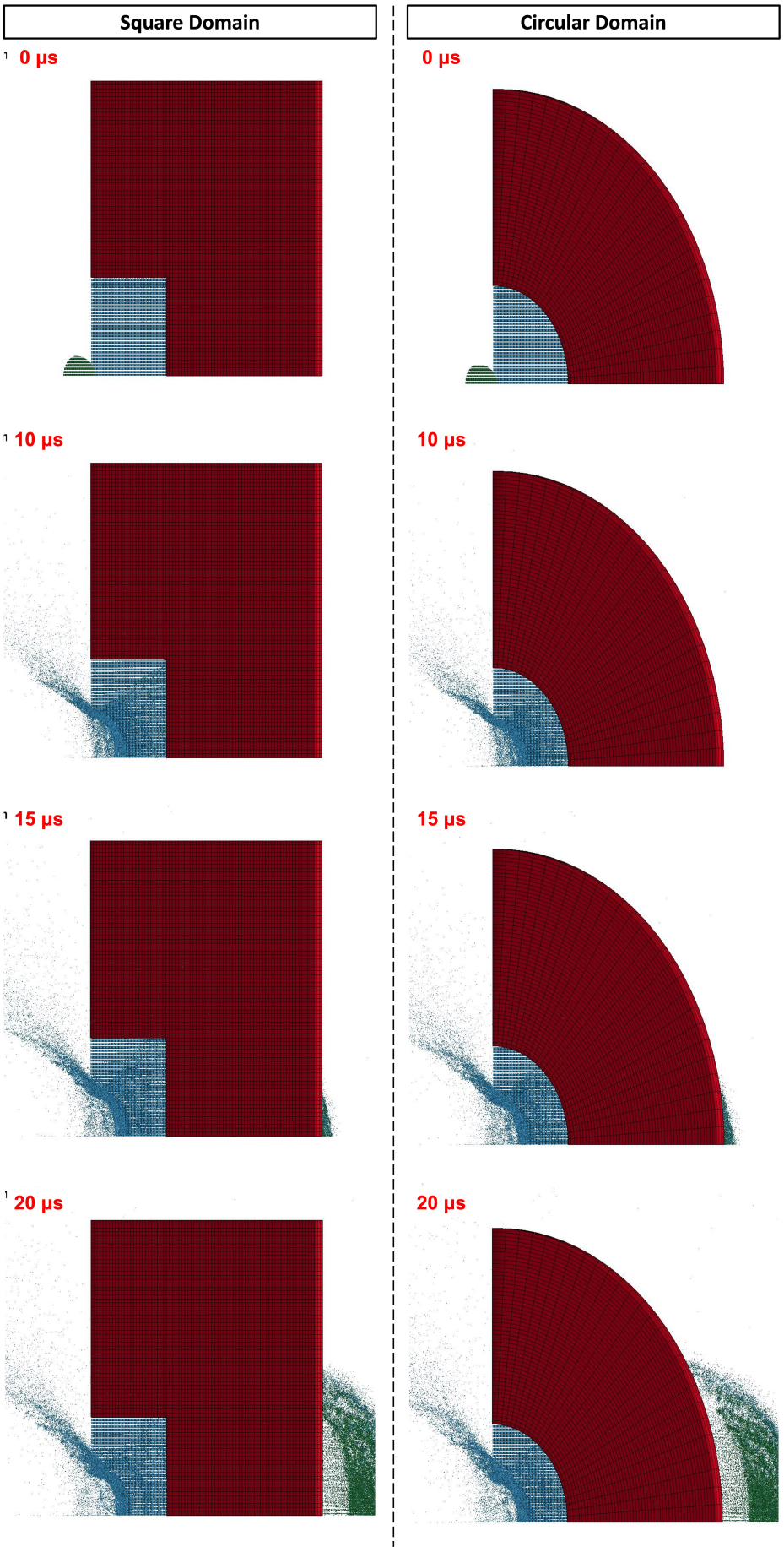

Figure 3.4: HVI evolution at different time-step in simulation with tied SPH/FEM interface with a square (left column) and a circular (right column) SPH domain (oblique view - pictures from LS-DYNA Pre-Post V4.8).

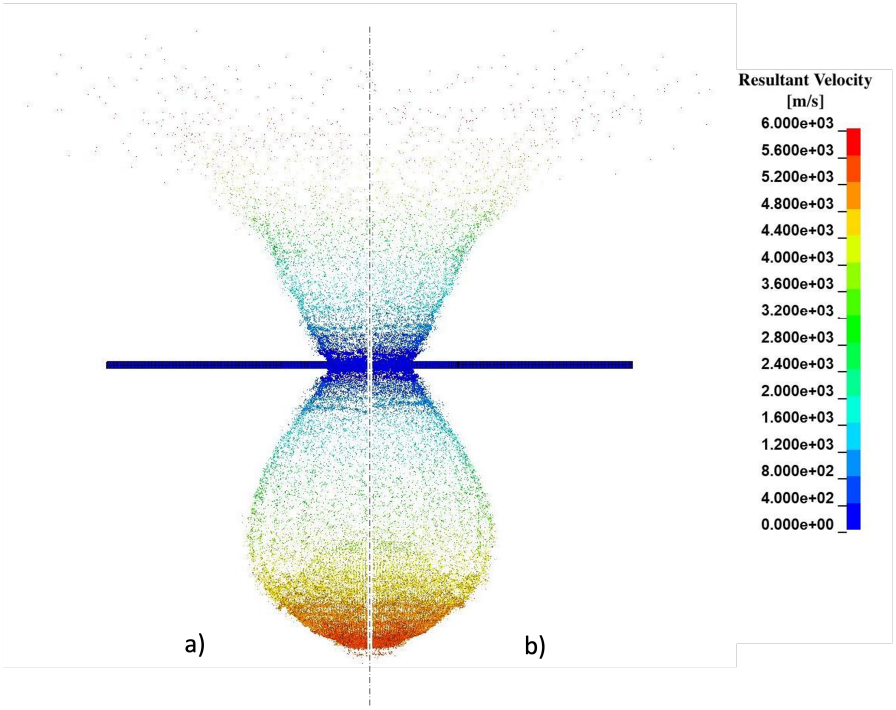

Figure 3.5: Resultant velocity profile at 16 µs in simulation with tied SPH/FEM interface with a square (a) and a circular (b) SPH domain. Initial projectile movement downward (lateral view - pictures from LS-DYNA Pre-Post V4.8).

3.2.3. Adaptive Contact

To identify the optimal simulation methodology for modeling HVI, a different SPH-FEM contact algorithm was investigated. The second type of contact methodology is a solid-to-SPH transition zone between the SPH and FEM plate components. It is implemented using the LS-DYNA keyword ***DEFINE_ADAPTIVE_SOLID_TO_SPH**. With this method, a hybrid solid elements are added between the SPH model and the finite element model of the plate. Each hybrid element uses both solid and particle discretization techniques. The solid component is then constrained through tied contacts. On the finite elements domain side using ***CONTACT_TIED_SURFACE_TO_SURFACE**, while, on the SPH domain side using ***CONTACT_TIED_NODES_TO_SURFACE** keyword.

The use of this contact system, which is still based on kinematic constraints, ensures a smoother transition due to the dual nature of the transition area, resulting in more accurate stress propagation to elements further from the impact zone.

The *DEFINE_ADAPTIVE_SOLID_TO_SPH keyword has been introduced to create SPH particles, either as replacements or supplements for solid Lagrangian elements. This feature is valuable for dynamically transforming a Lagrangian solid part into SPH particles, especially when the constituent Lagrangian solid elements fail. One or more SPH particles can be generated for each failed element. These particles automatically inherit all Lagrangian node and integration point quantities from the failed solid elements. The constitutive properties of the new SPH part correspond with the referenced material and EOS in the new SPH part definition.

Successively, this feature has also been implemented to ensure a smooth transition from a SPH

to a solid element domain. The SPH formulation can withstand significant deformation, while the solid meshes accurately describe the material interfaces. The interaction works by constraining SPH node locations with solid elements, while SPH elements introduce a penalty force term against solid node movement [105].

The *DEFINE_ADAPTIVE_SOLID_TO_SPH keyword offers flexibility in specifying the number of SPH particles generated per element. Hexahedral elements can contain (n × n × n) SPH elements, where "n" ranges from 1 to 3. Control parameters enable the user to manage the type of coupling between SPH particles and adjacent solid elements, i.e. interaction, no interaction or thermal only, as well as to define the start time of this coupling - either from the beginning of the simulation or from the moment of failure of the solid element.

To ensure the accurate establishment of the contact hybrid layer interface between the SPH and FEM domains, the coupling is triggered at the beginning of the simulation. In the transition zone between the SPH and FEM domains, 27 particles per solid element ($n = 3$) are generated (Fig. 3.6). This value represents a balanced compromise between computational efficiency and accuracy. It should be noted that the transition zone is placed significantly away from the point of impact, which eliminates the need for a higher particle count. However, the influence of the value of "n" on the accuracy of the stress wave propagation has not yet been investigated.

Fig. 3.6 shows a detail of the SPH/FEM adaptive interface method. The hybrid domain, consisting of solid elements and SPH particles, is rendered in yellow. To enhance clarity, the yellow solid elements have been made transparent and some have been blanked out to show the presence of the brown SPH particles in the interior. At the beginning of the simulation, as mentioned above, 27 particles were created per solid element.

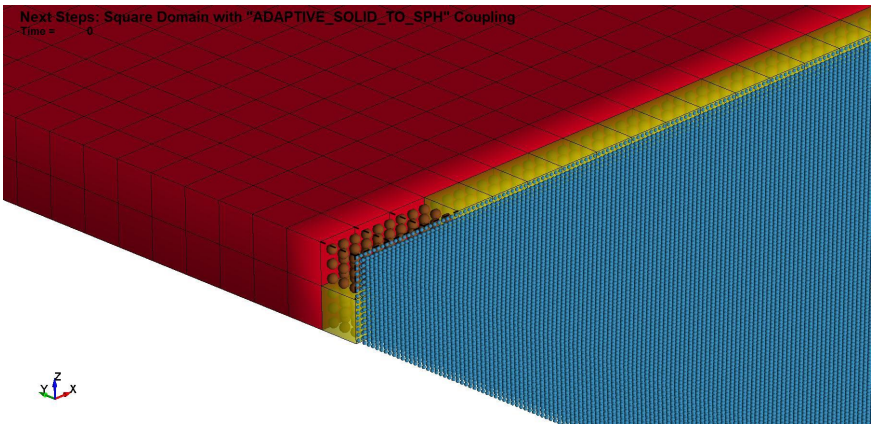

Figure 3.6: Detail of the SPH/FEM Adaptive interface method (pictures from LS-DYNA Pre-Post V4.8).

Adaptive contact has been implemented in both the square and circular domain SPH simulations, as shown in Table 3.2. Fig. 3.7 shows the geometry of the square SPH domain with adaptive contact simulation, while Fig. 3.8 shows the geometry of the circular SPH domain with adaptive contact simulation.

As in the tied contact models, the projectile (shown in green) is modeled as a quarter model of a sphere with a radius of 5 mm. The plate has straight edges that measure a total of 75 mm,

and the plate's SPH region encompasses edges that measure 25 mm. A transition domain of adaptable solid elements, 1 mm in width and represented in yellow, is enclosed between the SPH domain of the plate (shown in blue) and the FEM domain (shown in red). In both simulations, the interparticle distance within the plate SPH impact zone and the projectile is consistently maintained at 0.125 mm.

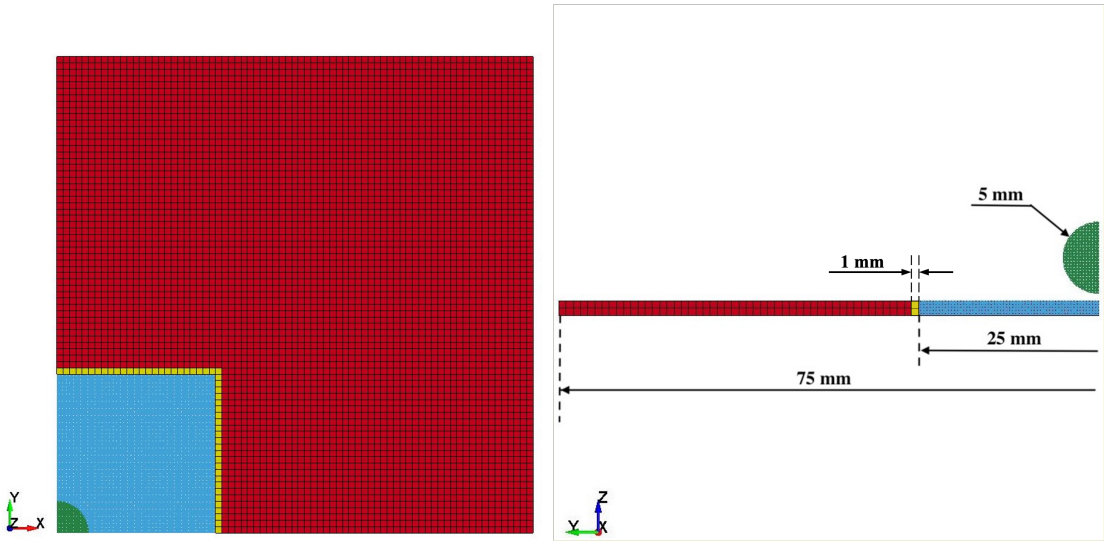

Figure 3.7: Geometry of the square SPH domain with adaptive contact test simulation (top and lateral view - pictures from LS-DYNA Pre-Post V4.8).

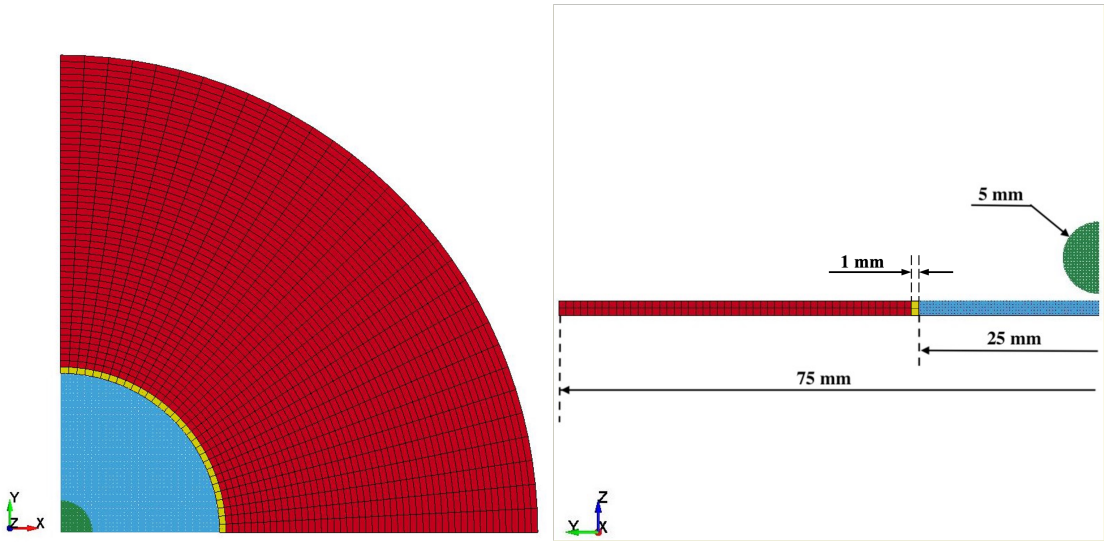

Figure 3.8: Geometry of the circular SPH domain with adaptive contact test simulation (top and lateral view - pictures from LS-DYNA Pre-Post V4.8).

The projectile consists of 67,024 particles in both scenarios. The plate is composed of 640,000 particles and 9,898 solid elements in the square domain configuration, and 502,416 particles and 2,548 solid elements in the circular domain setting. In both scenarios, the SPH domain contains 16 particles across the thickness of the plate, while the adaptive - or SPH/FEM interface - and FEM domains have two elements. It is important to note that, adhering to the previously described contact settings, 27 SPH particles are generated for each adaptive solid element.

Concerning the specifics of the contact setup, 102 adaptable solid elements are used in the square domain simulation, while 52 of them are used in the circular domain simulation. The SPH particles that are linked with the adaptable FEM interface zone are generated only at the beginning of the simulation. In the square domain simulation, a total of 2,754 newly generated SPH particles are created, while in the circular domain simulation the amount is 1,404. Both simulations were executed in parallel using 16 MPP processors. The total CPU time was 3861 seconds (1 h, 4 min, 21 sec) for the square SPH domain simulation and 2489 seconds (41 min, 29 sec) for the circular SPH domain simulation.

As previously illustrated in Section 3.2.2, the validation of both simulations and their comparison with other tests involves the gathering of identical key metrics (final crater radius, debris cloud length, maximum debris cloud radius, and axial velocity at the cloud front 16 µs post-impact). These values, along with their respective relative errors, are presented in Table 3.7. Furthermore, Fig. 3.9 provides a top view illustration of the crater shape, while a representation in oblique view of impact evolution is displayed in Fig. 3.10. Figure 3.11 shows the velocity profile at 16 µs post-impact.

	Crater diameter (final)	**Debris Cloud Velocity** (16 μs)	**Debris Cloud Length** (16 μs)	**Cloud diameter** (16 μs)	**Avg.**
Experimental data	18.90 mm	5296 m/s	81.1 mm	65.6 mm	–
Square impact domain	21.11 mm (11.70 %)	5298 m/s (0.04 %)	80.4 mm (0.9 %)	68.6 mm (4.57 %)	**4.30 %**
Circular impact domain	21.37 0mm (12.69 %)	5276 m/s (0.38 %)	80.6 mm (0.6 %)	68.1 mm (3.81 %)	**4.37 %**

Table 3.7: Results and relative errors of adaptive SPH/FEM interface simulation with a square or a circular SPH domain.

The findings are consistent with those reported for the tied contact case. Therefore, it is reasonable to conclude that the choice between the SPH and FEM zone contact methods does not affect the accuracy of the simulation regarding the analyzed parameters. As a result, the size of the crater formed and the characteristics of the debris cloud remain quite the same.

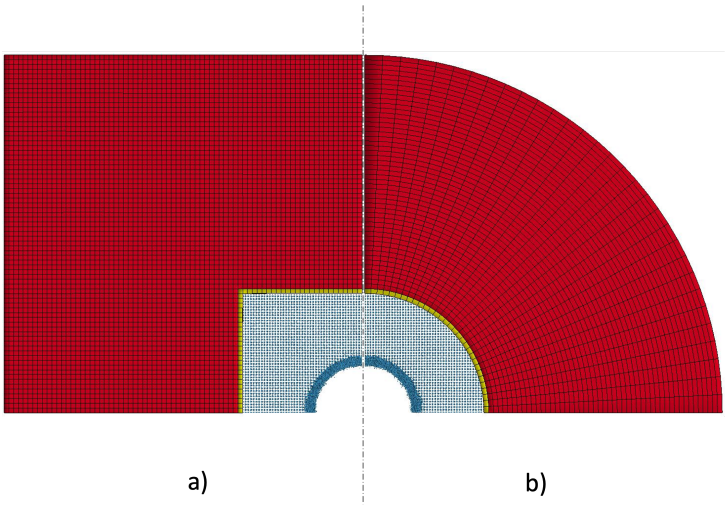

Figure 3.9: Final crater in simulation with adaptive SPH/FEM interface with a square (a) and a circular (b) SPH domain (top view - pictures from LS-DYNA Pre-Post V4.8).

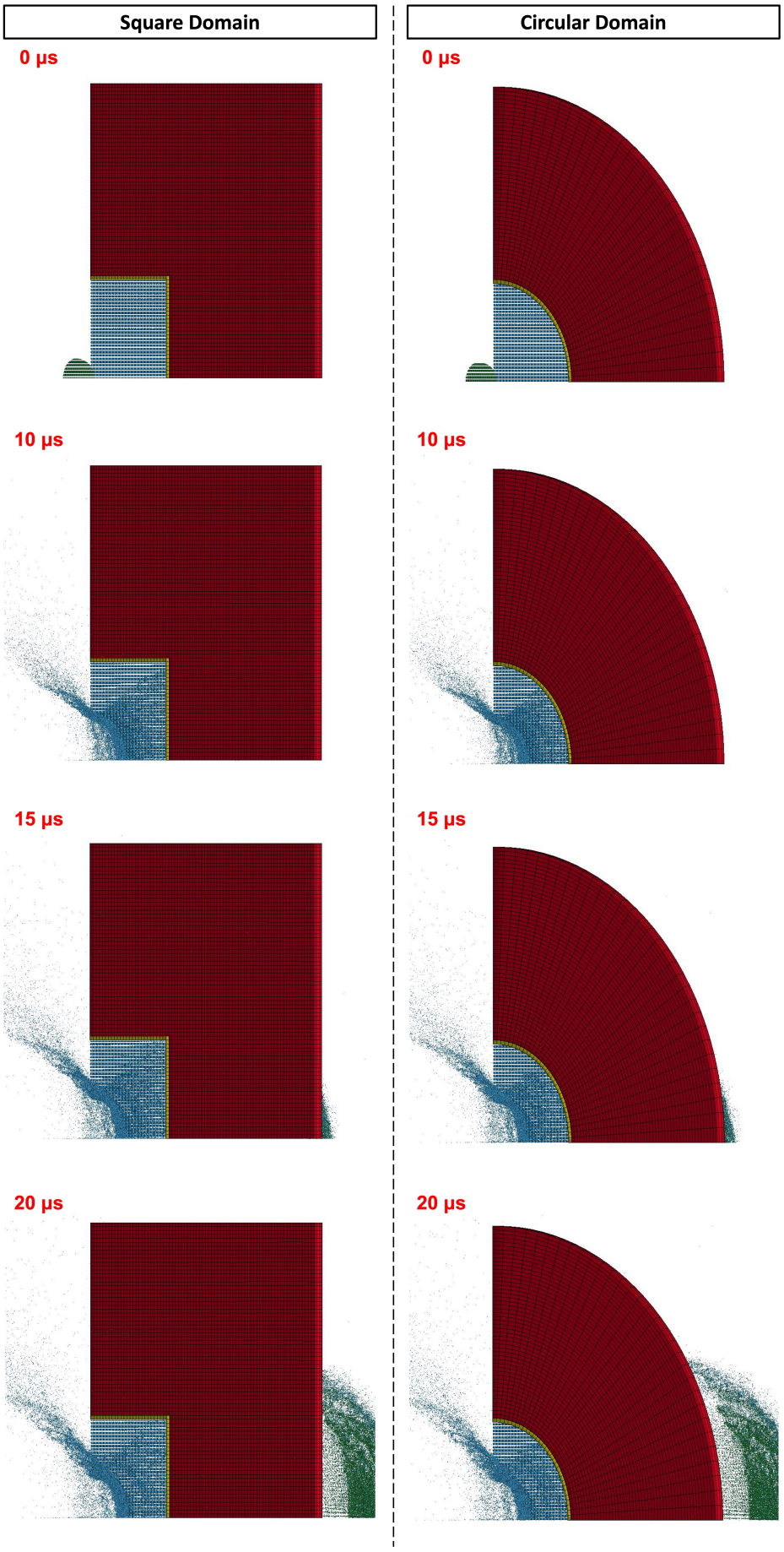

Figure 3.10: HVI evolution at different time-step in simulation with tied SPH/FEM interface with a square (left column) and a circular (right column) SPH domain (oblique view - pictures from LS-DYNA Pre-Post V4.8).

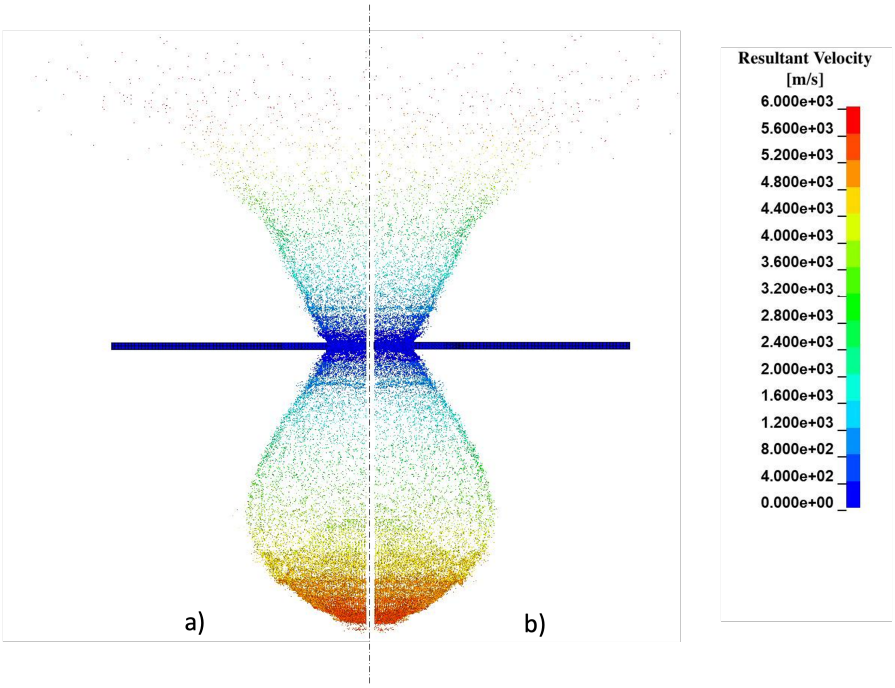

Figure 3.11: Resultant velocity profile at 16 µs in simulation with adaptive SPH/FEM interface with a square (a) and a circular (b) SPH domain (lateral view - pictures from LS-DYNA Pre-Post V4.8).

3.3. Stress Analysis in the Plate

In the previous sections, two different contact methods were used to simulate the impact of a spherical debris on an aluminum plate. Table 3.8 reports a comparison of the simulation results collected in tables 3.6 and 3.7, including the average errors. Based on the data presented, it is clear that the type of SPH/FEM contact setting has no impact on the morphology of the resulting crater and debris cloud.

	Square Tied	Circular Tied	Square Adap.	Circular Adap.
Average Error	4.25 %	4.10 %	4.30 %	4.73 %

Table 3.8: Average error of the simulations described in Section 3.2

The choice of SPH/FEM contact setting mainly affects the propagation of stress waves from the impact site to the rest of the panel. It is important to note that the need to find the best way of coupling between the SPH and FE domains arises from the requirement for accurate propagation of stress wave and acceleration from the impact site to the satellite in order to evaluate the effect of the MM/OD HVI on the new generation of satellites equipped with increasingly sensitive instrumentation.

Fig. 3.12 shows the propagation of the stress wave from the impact site to the rest of the modeled plate in the tied contact setting with a square and a circular domain. The results of four successive times that are the most significant for the SPH/FEM stress-wave transition process are reported to give the reader a complete understanding of the phenomena: at 7, 9.5, 12, and 14.5 µs post-impact. A black background has been chosen for better contrast.

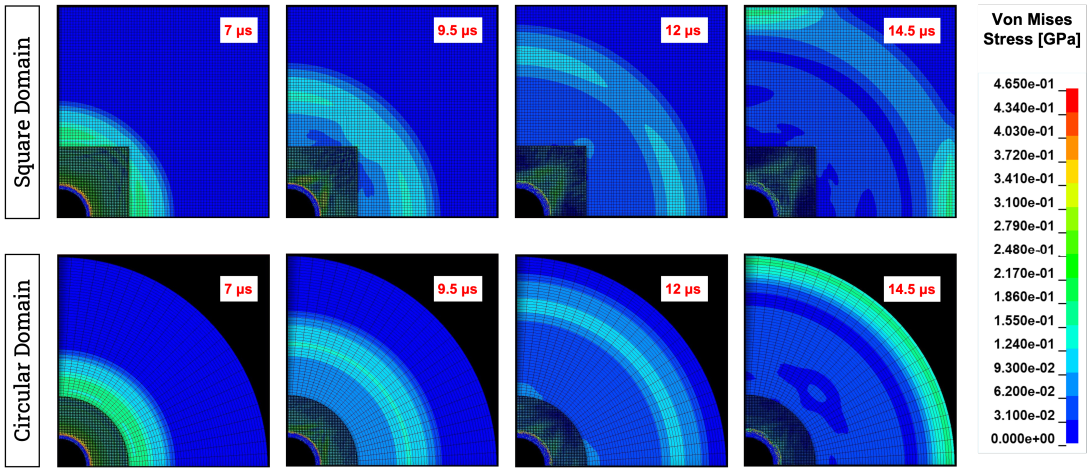

Figure 3.12: Stress wave propagation in simulation with tied SPH/FEM contact interface with a square (first row) and a circular (second row) SPH domain at 7, 9.5, 12, 14.5 µs after the impact (pictures from LS-DYNA Pre-Post V4.8).

In Fig. 3.13, the propagation of the stress wave from the impact site to the rest of the modeled plate is shown in the adaptive contact setting with a square and a circular domain. These results were acquired simultaneously with those in the previous illustration.

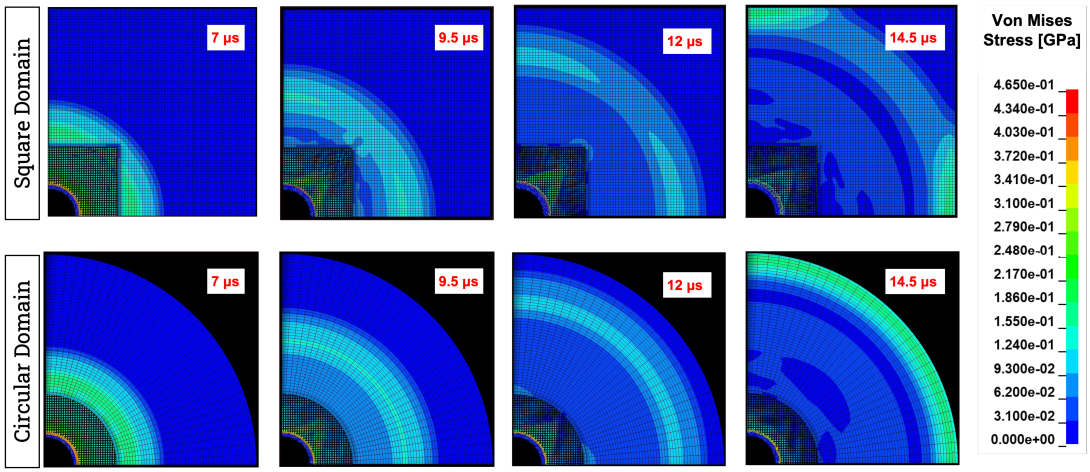

Figure 3.13: Stress wave propagation in simulation with adaptive SPH/FEM contact interface with a square (first row) and a circular (second row) SPH domain at 7, 9.5, 12, 14.5 µs after the impact (pictures from LS-DYNA Pre-Post V4.8).

Qualitative analysis of the images suggests a potential improvement in the circular region. However, it is not clear whether this improvement is entirely attributable to an improved interface between SPH and FEM. It is possible that the observed enhancement is primarily due to a uniformity and synchronicity of errors, particularly concerning equidistant points from the impact center. Further investigation is necessary to distinguish the separate effects of interface refinement and uniform error distribution on the performance differences between domains.

Ensuring energy conservation in simulations is crucial for accuracy and reliability. Energy losses, especially at interfaces between modeling methods, can introduce errors and compromise results. Therefore, analyzing energy variation throughout simulations is crucial for understanding performance and identifying areas for improvement.

In Section 3.4 a study of energy variation with different simulation setup has been conducted. The purpose of this analysis is to determine the effectiveness of SPH/FEM contact methods in conserving energy. This can help refine and optimize simulation contact methodologies for greater accuracy and robustness.

In order the assess the goodness of the contact it would also be interesting to look for internal reflection of the stress wave within the plate at the SPH/FEM interface. This type of phenomena, although not physical, and therefore dangerous for the correctness of the simulation, is typical of interface surface between two different modelling methods. This topic is fully discussed in Section 3.5.

Additionally, it is possible to observe an axial asymmetry along the edges of the circular domain with symmetric boundary conditions. This presents a significant challenge that could potentially be reduced by considering a complete representation of the plate instead of limiting the simulation to a quarter section of the problem domain. To improve the accuracy and robustness of the simulation, it may be beneficial to address the axial asymmetry issues by modeling the entire plate. However, this approach will increase the computational cost of the model. This strategy is discussed further in Section 3.6.

3.4. Energy Consideration

LS-DYNA is an explicit dynamic solver that can model the complex physics associated with short-duration, high-intensity events subject to complex, nonlinear, and transient dynamic forces. In contrast to implicit analysis methods, where convergence relies on factors such as force, moment, displacement, and heat to maintain equilibrium, the computational algorithms employed in explicit dynamic analysis prioritize the conservation of mass and momentum. Hence, there is no explicit consideration of energy conservation. Consequently, to ensure the validity of simulation results, it is essential for users to verify the overall energy balance, thus monitoring the principles of energy conservation throughout the simulation process [23].

The basic idea is that if all possible sources of error have been effectively addressed, the total energy of a system should exhibit minimal variation throughout the simulation. Therefore, quantifying the degree of energy fluctuations is a diagnostic tool for assessing the level of error in the simulation. By monitoring the degree of energy alteration, researchers can determine the accuracy of the simulation and evaluate the effectiveness of error minimization strategies used.

Generally, an energy imbalance does not necessarily indicate incorrect results. As long as the user knows where the energy is coming from and where it is going, it should be safe.

In this section a study of energy variation with different simulation setup has been conducted. The purpose of this analysis is to determine the effectiveness of SPH/FEM contact methods in conserving energy. This can help refine and optimize simulation contact methodologies for greater accuracy and robustness.

Energy conservation can be checked using an *Energy Error* term. It is defined as the ratio be-

tween the relative energy error to the maximum energy value between current energy, reference energy, and work done.

$$\textbf{\textit{Energy Error}} = \frac{|Current\ Energy - Reference\ Energy - Work\ Done|}{\max\{|Current\ Energy|,\ |Reference\ Energy|,\ |Work\ Done|\}} \tag{3.1}$$

where the $Reference\ Energy$ is the energy sum at the beginning cycle, the $Current\ Energy$ is the energy sum at the current cycle, and the $Work\ Done$ is the sum of work done by constraints, loads, body forces, contact penalty forces, and energy removed from the system by element erosion.

Another possible way to check the energy balance is by checking the *Energy Ratio*. It is defined as the ratio of the total energy within the system to the sum of the initial total energy and external work and, for the perfect energy balance, it should be constantly equal to 1 [23].

$$\textbf{\textit{Energy Ratio}} = \frac{Total\ Energy}{(Initial\ Total\ Energy + External\ Work)} \tag{3.2}$$

However, when solving the explicit dynamics problem, there can be different sources that cause energy imbalance, such as the hourglass energy, numerical erosion mechanisms, and boundary conditions.

In Fig. 3.14 the Total, Kinetic and Internal Energy of the previous simulations are shown. The main clue is to verify wherever the SPH/FEM contact setting can be considered as a cause of energy loss throughout the simulation.

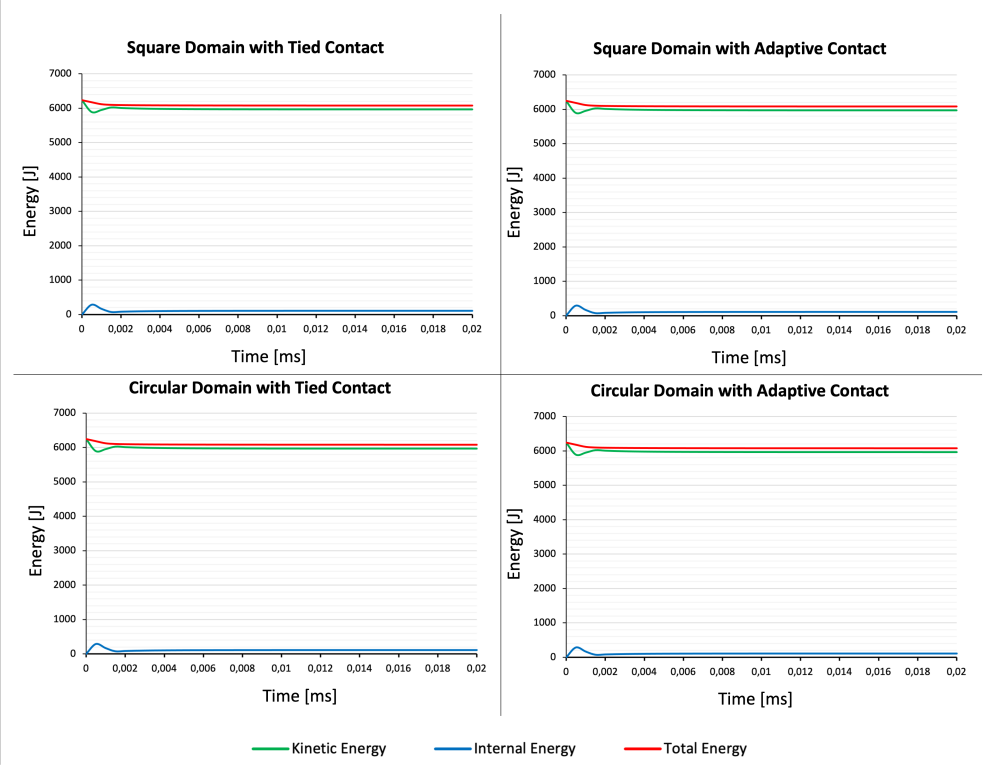

Figure 3.14: Total, Kinetic and Internal Energy evolution during the simulation for different simulation settings.

The simulations all follow a similar pattern. Initially, the system's total energy consists entirely of the projectile's kinetic energy. Upon impact, some of this energy is converted into the internal material energy of the plate and the projectile. It is important to note that there is some leakage of the total energy. In Fig. 3.14, the hourglass energy, which must be minimised in order to guarantee the accuracy of the simulation, is not shown because of its negligible value. In fact, in all four simulations, it does not surpass 0.02 J.

The graph in Fig. 3.15 displays the Energy Ratio over time for the previous simulations. The graph shows that the energy dispersion throughout the simulation is not affected by the interface contact setting. The curve pattern is similar for all four types of simulation settings, leading to an asymptotic value of 0.973. Presumably, the projectile impact contact configuration ought to be examined. Although the energy ratio is not constant throughout the simulation, it is important to note that this does not affect the validity of the simulation. It is generally accepted that small losses are acceptable for simulation validity [23].

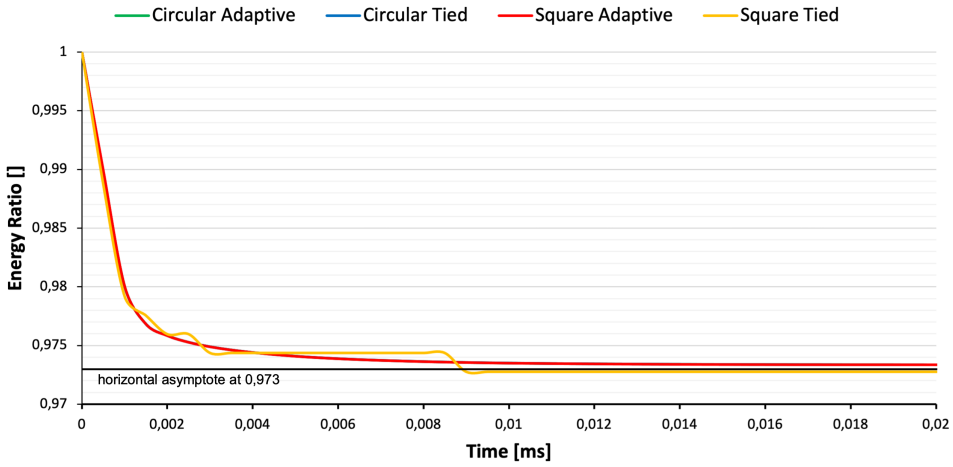

Figure 3.15: Energy ratio evolution during the simulation for different simulation settings.

3.5. Stress-Wave Internal Reflection

To assess the quality of contact, it is essential to analyze the internal reflection of stress waves within the plate at the interface between the SPH and FEM domains. This study is significant because non-physical phenomena can occur at the interface of different modeling methodologies, which may compromise the accuracy of the simulation.

The study also aims to evaluate the effect of symmetry planes implemented in the quarter model. Data were collected at three different locations along the SPH/FEM interface. Two measurement points are positioned near the symmetry planes with their normals along the x or y axis, and the third one is positioned in the center of the SPH/FEM interface at a 45-degree angle (Fig. 3.16).

The study was performed only on the circular domain configuration for simplicity sake. The methodologies for tied and adaptive contact are similar, but the differences will be highlighted in the following subsections. The purpose is to determine the effectiveness of SPH/FEM contact methods in ensuring a continuous and smooth stress-wave propagation. This can help refine

and optimize simulation contact methodologies for greater accuracy and robustness.

3.5.1. Methodology

The methodology used in this analysis is based on the primary assumption of an axially symmetric behavior, which governs the stress wave propagation phenomenon, especially in the immediate post-impact time period. However, to evaluate the effect of the symmetry planes, three different locations along the SPH/FEM interface were analyzed. As mentioned above, two data points are located in the proximity of the edges where a symmetrical boundary condition has been applied, while the third one is set at the midpoint of the interface.

To analyze the effect of the SPH/FEM interface, stress history data were collected at two contiguous measurement spots for three times along the interface for comparative analysis. In resulting graphs shown in Section 3.5.2, one stress data curve belongs to the SPH domain, while the other belongs to the FEM domain.

Figure 3.16, which does not depict the entire plate but rather only the portion of interest, shows schematic representations for both the tied and adaptive contact configurations. The approach is based on the assumption that stress data between two adjacent location sections should be congruent over time, despite a temporal displacement proportional to the velocity of the shock wave within the material and a marginal attenuation of the signal amplitude due to increased volumes of the outermost section and inherent damping effects induced by the stiffness of the plate. This congruence should hold even if the sections join two different numerical methodology domains.

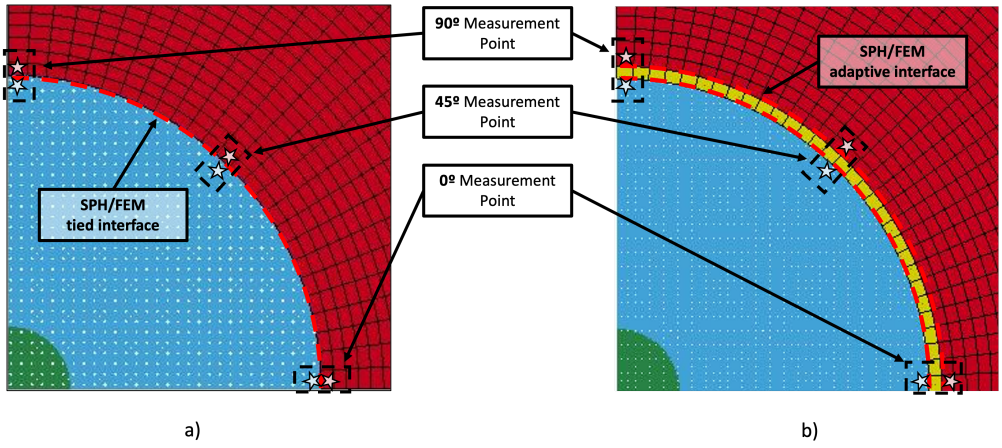

Figure 3.16: Schematic representation of the stress-wave internal reflection testing methodology in tied contact setting (a) and in adaptive contact setting (b).

The expected outcome of this comparative assessment is a near-perfect match of stress data over time for adjacent measurement points in the SPH and FEM domains. Deviations from this anticipated congruence, evidenced by significant variations in the stress profiles, could potentially be indicative of reflective phenomena manifesting at the interface.

In the tied contact configuration, it is important to highlight that thanks to the bi-dimensionality of the interface contact methodology, it is possible to chose two contiguous measurement spots

that pertain to two different methodology domain. Both share one edge with the SPH/FEM interface. Schematic representation for the tied contact configuration is shown on the left side in Fig. 3.16.

On the other hand, in the adaptive contact configuration the interface contact methodology is a tri-dimentional circular crown section, for this reason it is not possible to chose two contiguous measurement points that pertain to two different methodology domain, but it order to make them both share one edge with the SPH/FEM interface, measurement points in the most external circular crown in the SPH domain and in the most internal circular crown in the FEM domain have been selected. In this way, both share one edge with the SPH/FEM adaptive interface. Schematic representation for the adaptive contact configuration is shown on the right side in Fig. 3.16.

To ensure comparability between stress history results in the SPH and FEM domains and to reduce the large noise introduced by analyzing only one particle, stress data undergo an averaging process across various elements within a small rectangular solid located at the desired spot. The solid has dimensions of 1 mm by 1 mm edges in the plate plane, and its height is equal to the entire plate thickness. Figure 3.17 presents an example of the selected particles used to obtain stress data history at a specific location within the SPH domain. Accordingly, the stress history data plotted in the following sub sections for the FEM domain are the results of an averaging process between the two elements along the plate thickness.

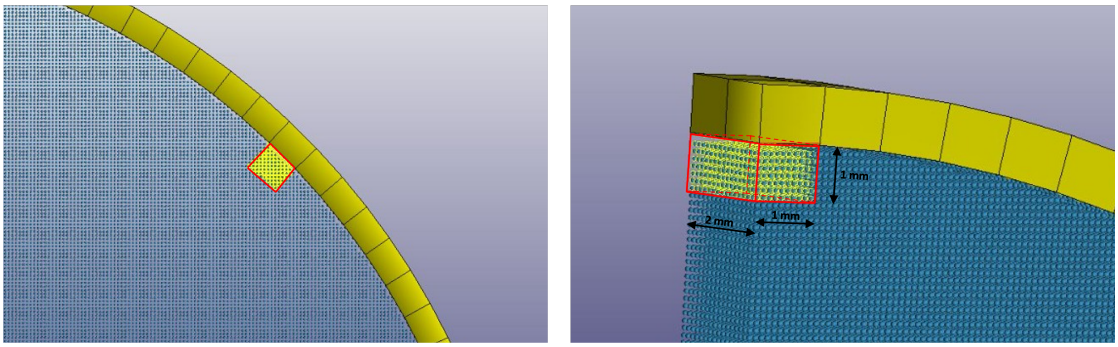

Figure 3.17: Selection methodology for SPH particles to obtain averaged stress data history at a specific location. Circular domain with adaptive contact scenario.

The result is a smoother representation of the stress evolution over time for a given point at a given distance and angle from the impact site.

In order to ensure the capability of fully capturing the behavior of the stress wave signal with high resolution, the sampling rate of the simulations required for this study was increased to 100MHz. As a result, the magnitude of the simulation output data increased.

3.5.2. Results

This section presents the results of numerical simulations conducted for stress-wave internal reflection investigation. The collected data provide a detailed analysis of von Mises stress data over time measured at specific points in tied and adaptive contact configurations, enabling an accurate assessment of the research hypotheses and objectives posed. The analysis was con-

ducted only using the circular domain setting.

The tied and adaptive contact scenarios are visualized in the following graphs using the same nomenclature and color correspondence, regardless of the three different locations of the SPH and FEM comparison (90, 45, or 0 degrees). Figures 3.18 to 3.20 display data related to the tied contact, while Figs. 3.21 to 3.23 display data related to the adaptive contact.

The stress data for the SPH point is presented in two curves on the graphs. The light green curve shows the original retrieved values, while the green curve shows the SPH von Mises stress data curve shifted in time to make it comparable to the FEM stress data. This shift in time compensates for the fact that the stress wave first invests the SPH point and then the FEM equivalent point. The time shift was evaluated with the goal of minimizing the difference in the curve during the initial rise.

It has been observed that the shift in time of the stress wave curve remains constant regardless of the analyzed direction. The average shift in time of the SPH von Mises stress curve in a tied contact configuration is 0.27 µs. In the adaptive contact scenario, this value doubles to approximately 0.51 µs. This is because the measuring points in the adaptive contact scenario are not contiguous, resulting in an average distance that is approximately double that of the tied contact scenario.

The stress curves for the tied contact methodology are shown in Figs. 3.18, 3.19, and 3.20 for comparisons at 90, 45, and 0 degrees, respectively.

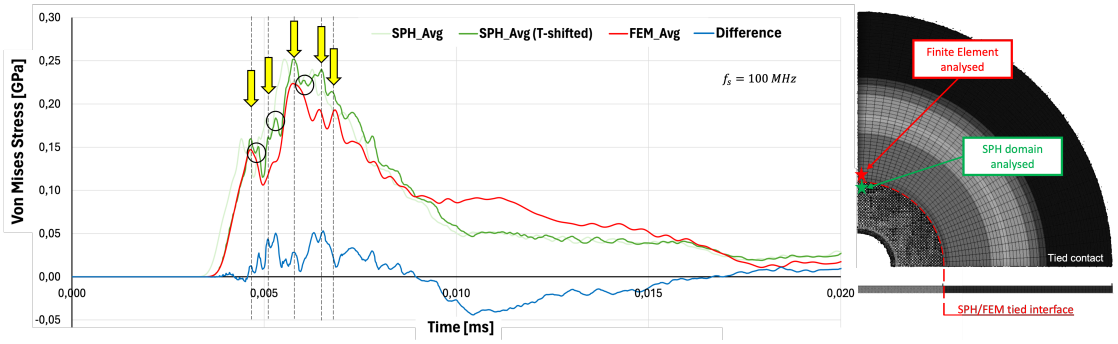

Figure 3.18: SPH and FEM von Mises stress data comparison in circular tied domain (top 90°).

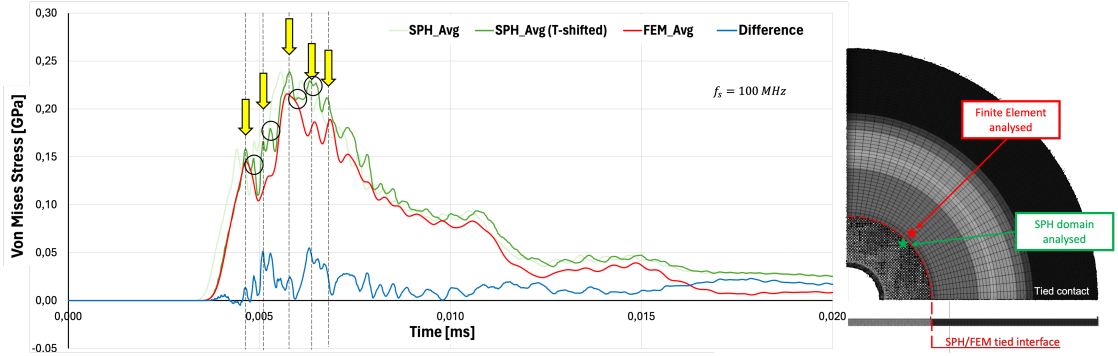

Figure 3.19: SPH and FEM von Mises stress data comparison in circular tied domain (middle 45°).

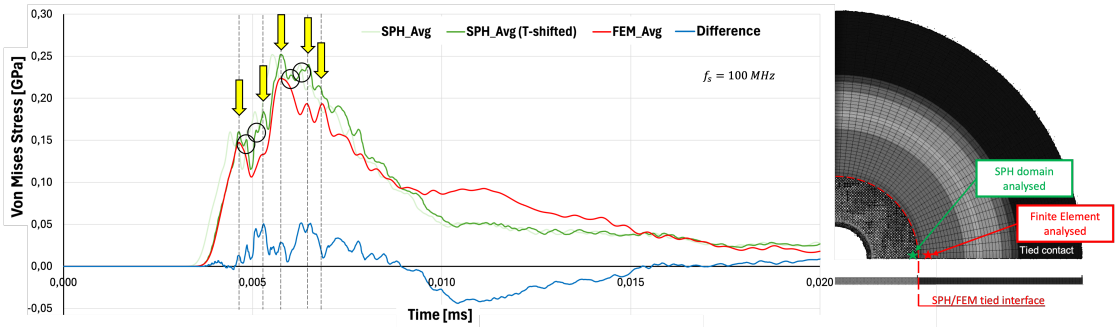

Figure 3.20: SPH and FEM von Mises stress data comparison in circular tied domain (bottom 0º).

Similarly, the von Mises stress curves for the adaptive contact methodology are shown in Figs. 3.21, 3.22, and 3.23 for comparisons at 90, 45, and 0 degrees, respectively.

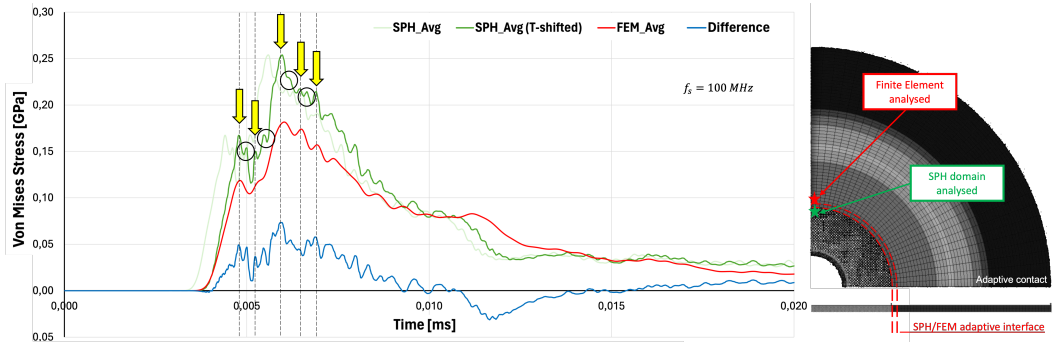

Figure 3.21: SPH and FEM von Mises stress data comparison in circular adaptive domain (top 90º).

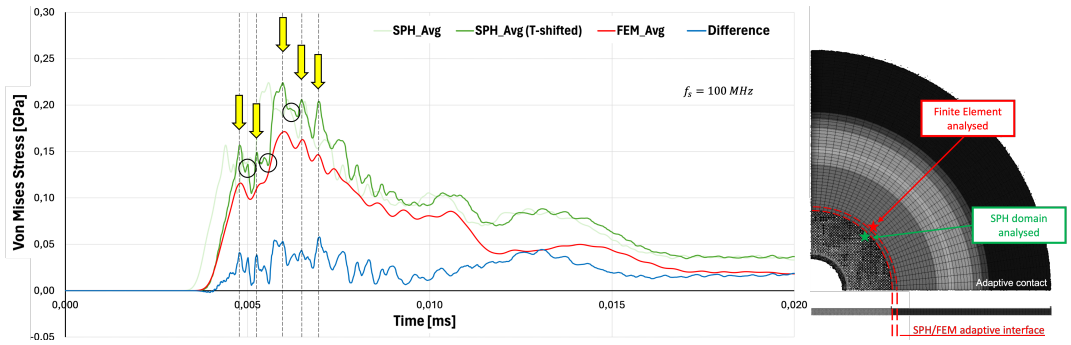

Figure 3.22: SPH and FEM von Mises stress data comparison in circular adaptive domain (middle 45º).

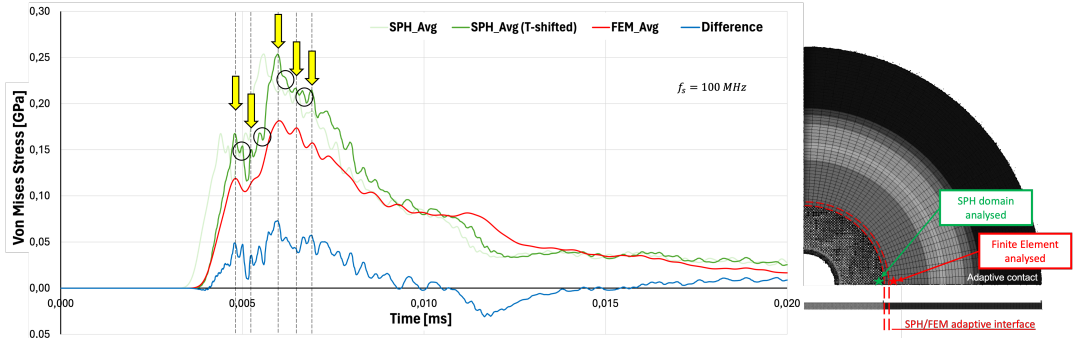

Figure 3.23: SPH and FEM von Mises stress data comparison in circular adaptive domain (bottom 0º).

Upon analysis, it is clear that there is a strong correlation between the data collected in the SPH and FEM domains. The results support the hypothesis of a temporal shift and minor signal amplitude attenuation due to increased volumes of the outermost section and inherent damping effects induced by the stiffness of the plate. Additionally, the two curves exhibit a similar pattern, indicating a high level of agreement. Indeed, both graphs show the main stress peaks occurring at the same time. The peaks are highlighted in the graph using a yellow arrow along a dashed line used to emphasize the temporal matching. This correspondence is particularly strong in the first few microseconds after the impact.

Moreover, the graphs use small dark circles to highlight stress peaks in the SPH data curve that do not appear in the respective FEM curve. The smaller stress peaks that occur immediately after a larger peak do not have a match in the FEM stress curve. Given the isotropic and homogeneous nature of the model material, these peaks are likely related to a numerical induced error. It is possible that they are related to the reflection of the stress waves in the proximity of the SPH/FEM interface.

By comparing the results from the tied and the adaptive contact, it is possible to observe that the latter methodology has a better performance in terms of the amplitude of these reflected peaks. Although the reflected stress peaks present in the tied contact configuration are not entirely eliminated through the use of an adaptive contact, their influence has been significantly mitigated.

The latter claim is supported by Fig. 3.24. Although such plots do not introduce any new data, they only show the stress signals collected at the same point in both the tied and adaptive contact cases. As might be expected, it is possible to observe that the stress pattern is the same in both configurations, with only slight deviations. In general, it can be observed that the peaks are less pronounced in the adaptive case (blue line) than in the tied case (red line). These findings have been interpreted as indicative of diminished reflection at the interface between the two methodologies employed and the stress wavefront, which propagates from the center outward.

It is important to note a general trend in the von Mises stress plots showing that, after a certain period of time, the stress field tends to become more uniform within the impacted plate. This behaviour is highlighted by the light blue line in the previous plots. Indeed, as the simulation progresses, the SPH and FEM differences in stress tend to diminish. To achieve full uniformity of the stress field, it may be necessary to implement longer simulations and larger plates to avoid boundary reflections.

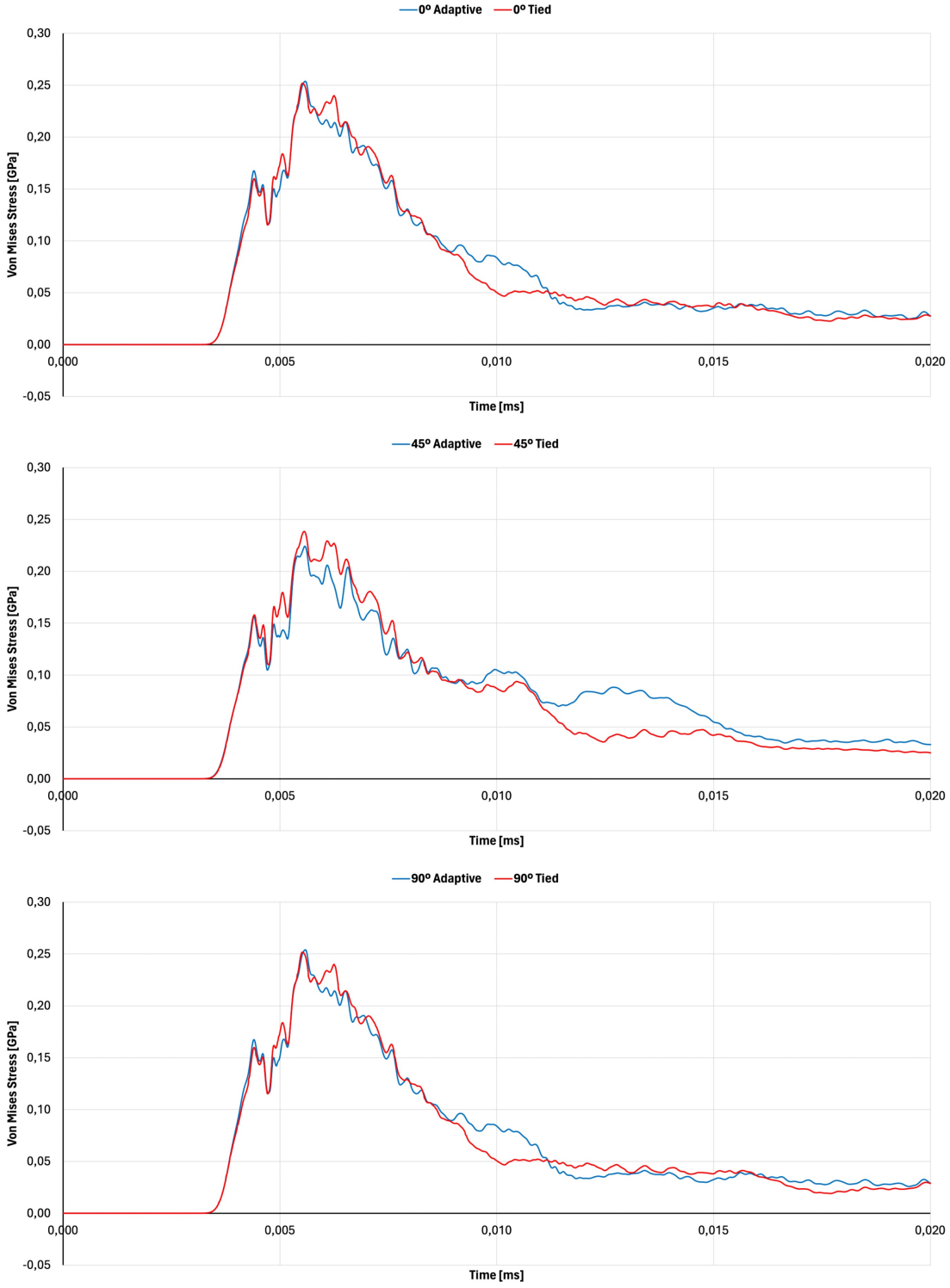

Figure 3.24: SPH von Mises stress data comparison in tied and adaptive circular domain at 90, 45, and 0 degrees.

3.6. Full Plate Model

As discussed in Section 3.3 and highlighted in Fig. 3.25, an axial asymmetry behaviour in stress wave propagation phenomenon is evident along the edges of the domain under symmetric boundary condition.

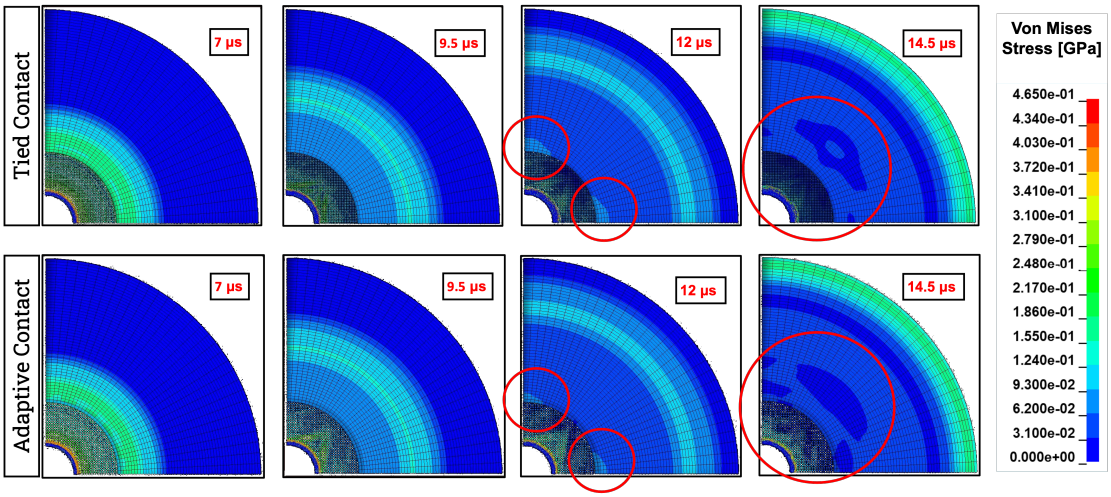

Figure 3.25: Stress wave propagation in simulation with circular SPH domain with a tied (first row) and an adaptive (second row) SPH/FEM contact interface at 7, 9.5, 12, 14.5 µs after the impact. Red circles highlighting axial asymmetry behaviour in stress wave propagation phenomenon (pictures from LS-DYNA Pre-Post V4.8).

By moving from modeling a quarter section to the entire plate, this phenomenon could be studied in more detail. Indeed, it may be worthwhile to model the entire plate, despite the associated increase in computational cost, given the potential benefits of evaluating the impact of symmetrical boundary conditions on stress wave propagation and improving overall accuracy and robustness.

This section presents a complete model of the scenario described in Section 3.1 and the resulting outcomes. Only one type of contact and domain shape has been investigated. Specifically, the circular domain with tied contact was chosen for assessment because it accentuates the axial asymmetry behavior in stress wave propagation (see Fig. 3.25, tied contact row at 12 and 14.5 µs post-impact).

3.6.1. Model Parameters

The full model closely mirrors the quarter model described in Section 3.2. The main differences stems in modelling the full system and in the implemented boundary conditions.

To replicate the experimental setup and to be consistent with the previously studied quarter model, the plate was modeled as a 75 mm radius, 2 mm thick disk. As in the previous setup, the outer edge of the plate are clamped during the simulation and the projectile was represented as a sphere with a 5 mm radius. For a graphical representation, see Fig. 3.26. The blue area represents the SPH plate impact region, the red area indicates the plate modelled with finite elements, and the green area the projectile modelled with SPH. The three stars in Fig. indicate study points from which stress history data has been obtained and which will be plotted in the following sections to compare stress over time at different locations.

To maintain consistency in the modeling approach, the same keywords are used for material properties, EOS, initial settings, and simulation control, as described in Section 3.2 and Appendix A. As mentioned earlier, a tied contact governs the SPH-FEM interaction.

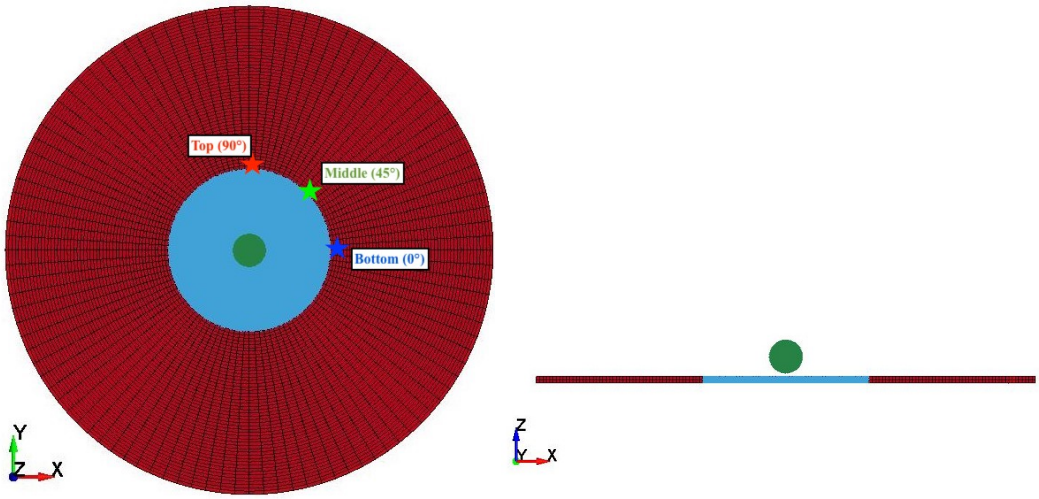

Figure 3.26: Geometry of the full model simulation (top and section view - pictures from LS-DYNA Pre-Post V4.8).

To ensure consistency with the quarter model simulations, even the same modelling parameters have been implemented. Specifically, the SPH interparticle distance within both the plate impact zone and the projectile is set at 0.125 mm. The projectile is composed of 268,096 particles. The plate comprises approximately 2 million particles and 10,200 solid elements. Additionally, the SPH region encompasses 16 particles within the plate's thickness, while the FEM region uses 2 elements.

3.6.2. Results

In this scenario, the validation of the simulation setup always pass through the same key metrics concerning crater and debris cloud geometry. The collected values, along with their relative errors, are listed in Table 3.9.

	Crater diameter (final)	**Debris Cloud Velocity** (16 μs)	**Debris Cloud Length** (16 μs)	**Cloud diameter** (16 μs)	**Avg.**
Experimental data	18.90 mm	5296 m/s	81.1 mm	65.6 mm	–
Quarter plate model	21.37 mm (13.01 %)	5249 m/s (0.9 %)	82.2 mm (1.4 %)	66.3 mm (1.1 %)	**4.10 %**
Full plate model	20.38 mm (7.83 %)	5351 m/s (1.0 %)	81.8 mm (0.9 %)	66.6 mm (1.5 %)	**2.81 %**

Table 3.9: Results and relative errors of circular SPH domain and tied SPH/FEM interface simulation in quarter and full plate configuration.

As expected, the transition from the quarter to the full model, although partially improving the simulation geometry outcome (with special reference to the crater diameter), has only a marginal impact on the accuracy of such data. The following analysis focuses on the characteristic of stress wave propagation.

Figure 3.27 illustrates the propagation of the stress wave from the impact site to the rest of the plate in the tied contact setting with a circular domain. To assess the impact of symmetry boundary conditions, the results of the quarter model with those of the full model have been compared. The study focused on two subsequent time points, 10.5 and 12 µs post-impact, which are considered to be the most relevant for observing the stress wave propagation distortion

effects (see Fig. 3.28). In each figure of the full model, the quarter model is superimposed within a red square located in the upper right corner.

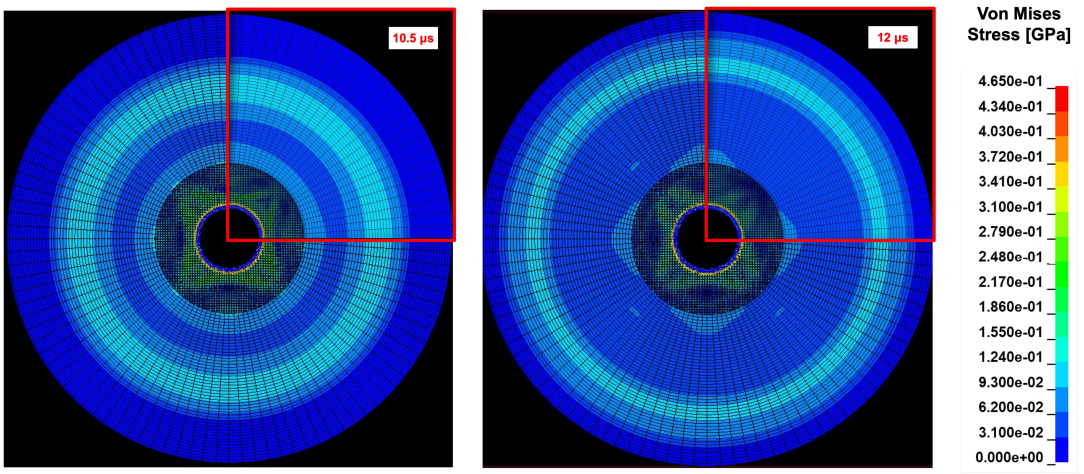

Figure 3.27: Stress wave propagation comparison between the full model and the quarter model (in the upper right corner) in simulation with tied SPH/FEM contact interface and circular SPH domain at 10.5 and 12 µs after the impact.

The results indicate that the simplified quarter model aligns well with the full model, suggesting that symmetry boundary conditions have only a marginal impact on stress wave propagation accuracy. Therefore, the asymmetry in stress wave propagation cannot be attributed to them, but rather to other factors. This observation highlights the accuracy achieved by the quarter model tests, but it does not explain the reason for the asymmetry in a theoretically axial-symmetric case study.

To evaluate the effect of the SPH lattice, von Mises stress history data were collected at three different locations along the SPH/FEM interface. For comparison, as described in Section 3.5, two data points along the x- and y-axes and a third at 45° were used. The data pertains to the FEM domain and the results are presented in Fig. 3.28. For clarification, the locations of the data points are illustrated in Fig. 3.26.

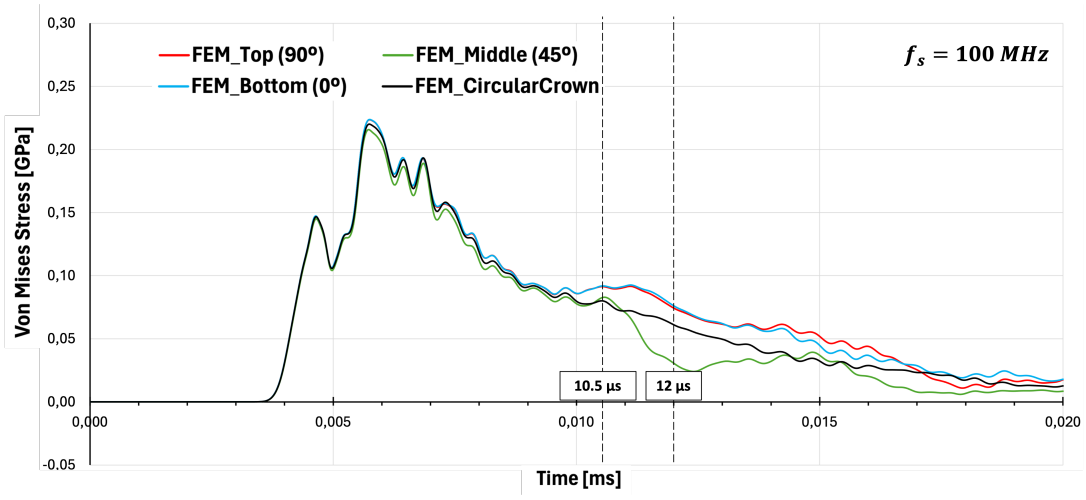

Figure 3.28: Von Mises stress data comparison in circular tied domain in FEM domain (SPH lattice configuration as default).

The graph shows a further manifestation of the anisotropy of the model in transmitting stress. The plotted trajectories reflect the behavior observed in Fig. 3.27. The stress evolution of the study points located along the x (0°) and y (90°) axes, represented by the red and blue curves respectively, show a similar progression with significant overlaps and only slight discrepancies. The stress relative to the study point located at 45°, represented by the green curve in the figure, shows a lower amplitude during most of the simulation. Additionally, the average stress obtained by averaging the stress values along the circular corona, which includes the data acquisition points for the more specific curves, is also illustrated.

After 10 microseconds, the trends of the two curves begin to differ significantly. The study point placed at 45° with respect to the x-axis shows a sharp decrease in stress level at that point, while the analysis reports only a progressive but controlled decrease in stress relative to points along the x- and y-axes. The data at 10.5 microseconds and 12 microseconds have been highlighted and illustrated in the Fig. 3.27 as representative of this abnormal behavior. It is noteworthy that all the curves tend to converge to similar values as the simulation progresses.

3.7. Influence of the SPH Lattice

Figures 3.27 and 3.28 indicate that stress waves exhibit a directional preference. This behavior, which is observed despite the complete absence of symmetry boundary conditions, can be attributed to the inherent lattice properties of the SPH model used to simulate the impact zone. The term ”*lattice*” is used to define the regular spatial arrangement of particles within the SPH framework. The lattice structure, which is determined by the initial placement, could influence the propagation of stress waves through the material. The directional preference observed in stress wave propagation can be related to the anisotropy introduced by the lattice, which influences the mechanical response of the model to impact forces.

The SPH plate and projectile were implemented in LS-DYNA using the pre-implemented ”SPH Generation” function for sphere and cylinder shapes. After determining the number of SPH particles per principal direction, the system automatically generates elements with an orthorhombic lattice. In this scenario, since the inter-particle distance is fixed at 0.125 mm, the lattice formed by the SPH particle can be described as simple cubic crystals (refer to Fig. 3.29).

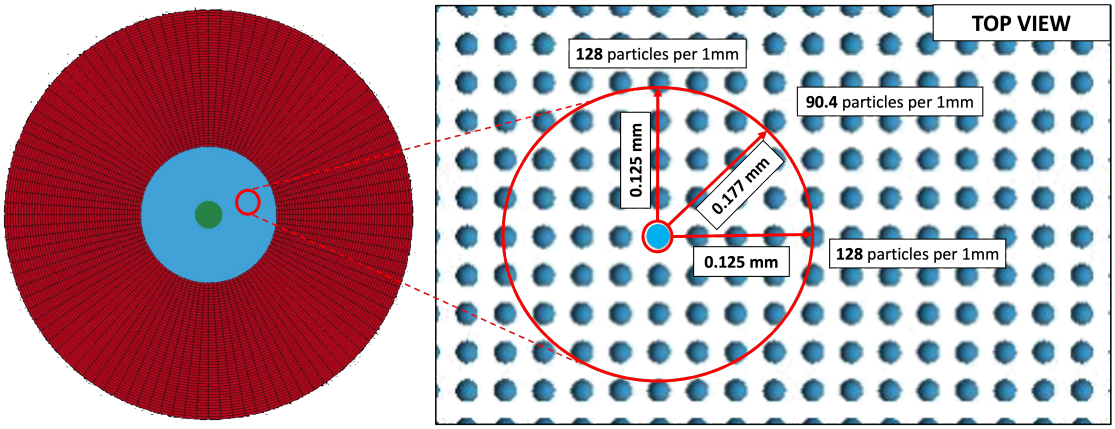

Figure 3.29: SPH lattice configuration as default setting in LS-DYNA.

With this configuration, the density of particles is higher along the principal directions than in the oblique direction. Since the interparticle distance along x or y axis is the user defined one, in the current case 0.125 mm, along the direction oriented at 45°, it is 0.177 mm.

$$c = \sqrt{2a^2} = \sqrt{(0.125\,mm)^2} = 0.177\,mm \tag{3.3}$$

where a is the user defined interparticle distance.

Furthermore, as shown in Fig. 3.29, the simulation implements 16 layers of SPH to discretize the out-of-plate direction, resulting in 128 particles along the x or y axis and 90.4 particles along the 45° oriented direction per 1 mm.

$$n_{x_{or}y} = \frac{1\,mm}{0.125\,p/mm} \times 16 = 128\,p \tag{3.4}$$

$$n_{45°} = \frac{1\,mm}{0.177\,p/mm} \times 16 = 90.4\,p \tag{3.5}$$

3.7.1. Rotated SPH Lattice Model

To assess the influence of the SPH lattice distribution, a new full model simulation was implemented while keeping all simulation parameters and LS-DYNA keywords identical to the previous simulations. The orientation of the SPH plate lattice is the only parameter that has been modified. The blue part in Fig. 3.30 representing the SPH plate has been rotated by 45 degrees (defined as positive according to the right rule) around the direction normal to the plate. The rest of the simulation remains identical. Specifically, the SPH lattice orientation of the projectile has not been altered.

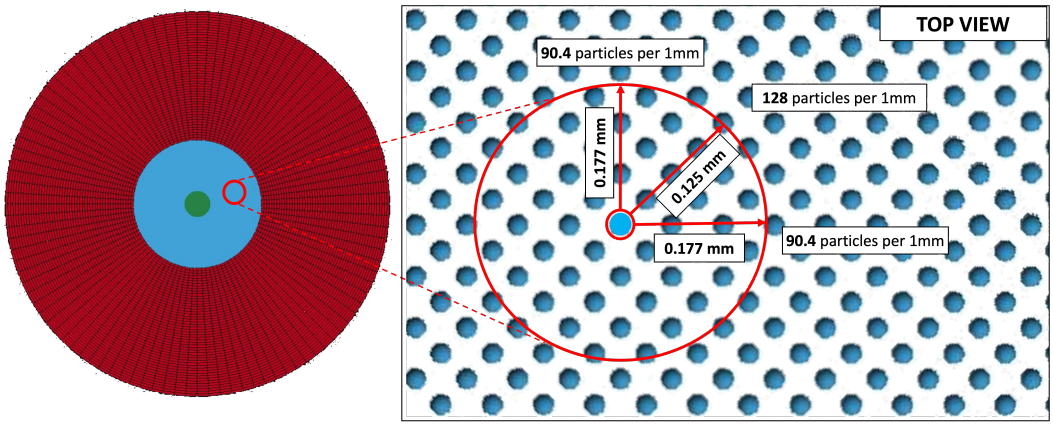

Figure 3.30: SPH lattice configuration in the rotated model.

Contrary to the previous section, in the present configuration, the density of particles along the oblique directions exceeds that along the x and y directions. This is due to the 45° rotation of the SPH lattice along the z-axis. As a result, the interparticle distance along the oblique direction is set by the user, which is 0.125 mm in the current case, while it is 0.177 mm along the x and y axes. Assuming a configuration of 16 layers of SPH along the thickness, as implemented in the simulation to discretize the plate, it is possible to observe 90.4 particles along the x or y axis and

128 particles along the 45° oriented direction (refer to Fig. 3.30)

$$n_{x_{or}y} = \frac{1\,mm}{0.177\,p/mm} \times 16 = 90.4\,p \tag{3.6}$$

$$n_{45^\circ} = \frac{1\,mm}{0.125\,p/mm} \times 16 = 128\,p \tag{3.7}$$

3.7.2. Results

Figure 3.31 illustrates the propagation of the stress wave from the impact site to the rest of the plate in the tied contact setting with a circular domain with the SPH plate domain lattice rotated by 45-degree in counterclockwise direction.

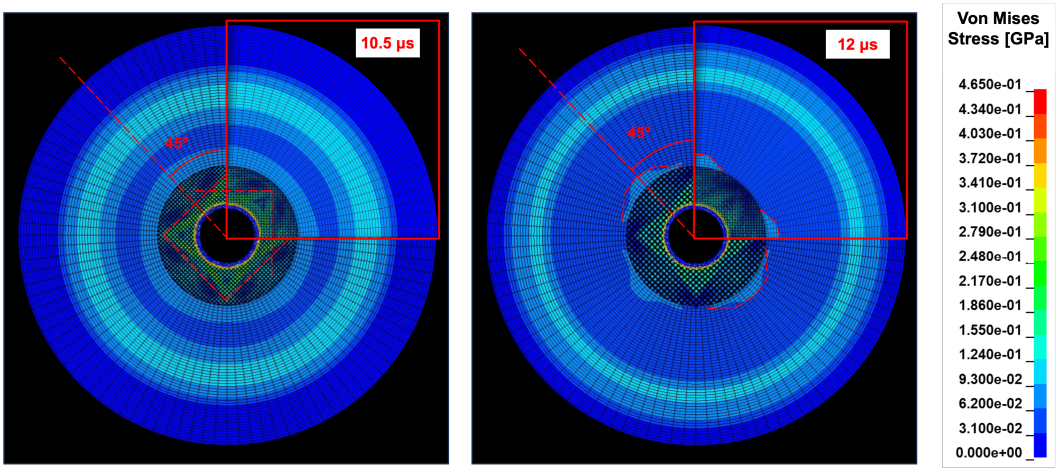

Figure 3.31: Stress wave propagation comparison between the full rotated model and the quarter straight model (in the right upper corner) in simulation with tied SPH/FEM contact interface and circular SPH domain at 10.5 and 12 µs after the impact. Red dashed lines highlighting the mismatched stress features.

As in the previous section, the stress wave propagation diagram results of the straight quarter model are compared with those of the rotated full model to evaluate the effect of the SPH lattice orientation. Two subsequent time points, 10.5 and 12 µs post-impact, were chosen. In each figure of the rotated model, a red square containing the standard quarter model is superimposed in the upper right corner.

The results suggest a correlation between the principal directions of the SPH lattice and the axial asymmetry introduced in the stress wave propagation phenomena, as expected. The stress pattern at a given time shows most features rotated by the same angle as the SPH lattice, indicating that stress propagates in the preferential directions. Red dashed lines highlight the differences between the two models and the angular mismatch.

To evaluate the effect of the SPH lattice rotation, von Mises stress data were collected at three locations along the SPH/FEM interface and reported in Fig. 3.32. Two data points are located along the x and y axes, while the third is set at 45°. The data refer to the FEM domain.

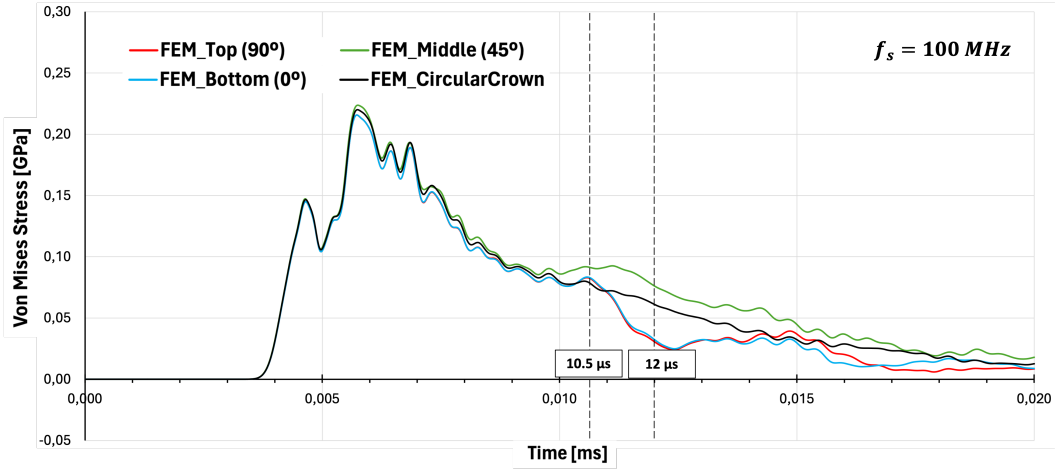

Figure 3.32: Von Mises stress data comparison in circular tied domain in FEM domain (rotated SPH lattice configuration).

The graph confirms the findings of the previous analysis regarding the effect of SPH lattice orientation on stress propagation. The plotted curves reflect the behavior observed in Fig. 3.31. The stress values for the points located at a 45-degree angle (shown in green) reproduce the values for the points located along the x- and y-axes in the standard model. Similarly, the values of the points located along the x and y axes (plotted in blue and red, respectively) reproduce the values of the points located along the oblique axis in the standard model, overlapping each other and showing only minor discrepancies.

3.7.3. Quasi-Isotropic SPH Lattice Model

Obtaining an accurate and reliable reconstruction of the stress propagation in a structure through simulations is crucial for identifying critical points and potential failing areas. To achieve this, it is important to implement a model in which stress waves are independent of the orientation of the SPH lattice. The material used in this simulation is homogeneous, but the region modeled in SPH behaves similarly to a material with anisotropic mechanical properties, responding and propagating stress differently depending on the direction of propagation.

To mitigate this effect and restore the isotropic mechanical properties of the simulated material, an attempt was made to equalize, at least along the previous study directions (x-axis, y-axis and 45° oblique), those parameters that, according to previous studies, conditioned the behavior of the material modeled by SPH, such as the average interparticle distance and, consequently, the average number of particles in one millimeter along the above directions.

To achieve this goal, a technique commonly used in composite material design was adopted to obtain a layup with quasi-isotropic mechanical properties. Therefore, it was decided to orient certain layers of SPH in specific directions, treating each layer as a unidirectional layer of composite material. Given the original SPH model consisting of 16 overlapping particle layers, some of them were oriented at 45° angle with respect to the reference axis, while maintaining the balance between oriented and non-oriented layers to ensure symmetry and balance in the layup.

Figure 3.33 presents a lateral schematic representation before and after the implementation of

the *"balanced"* and *"symmetrical"* lattice. Figure 3.34 provides a top view of the final result.

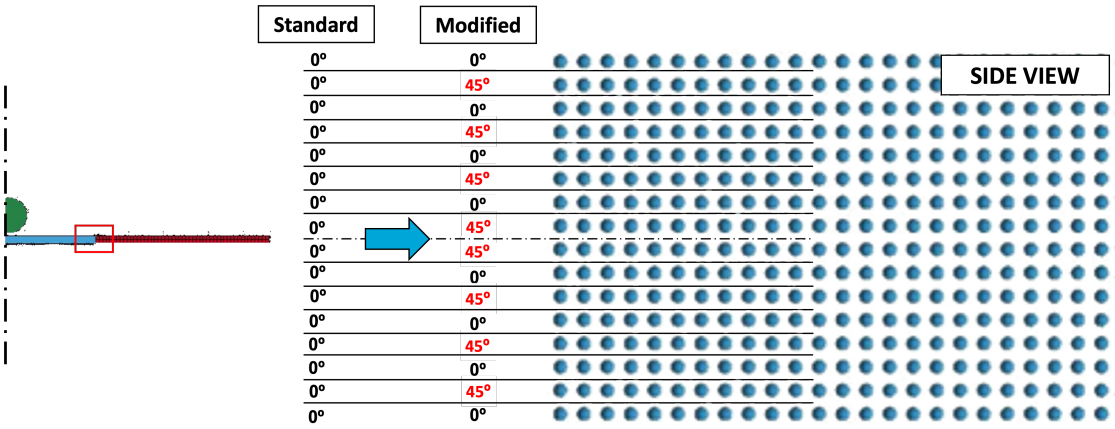

Figure 3.33: Lay-up strategy of the quasi-isotropic SPH lattice (side view).

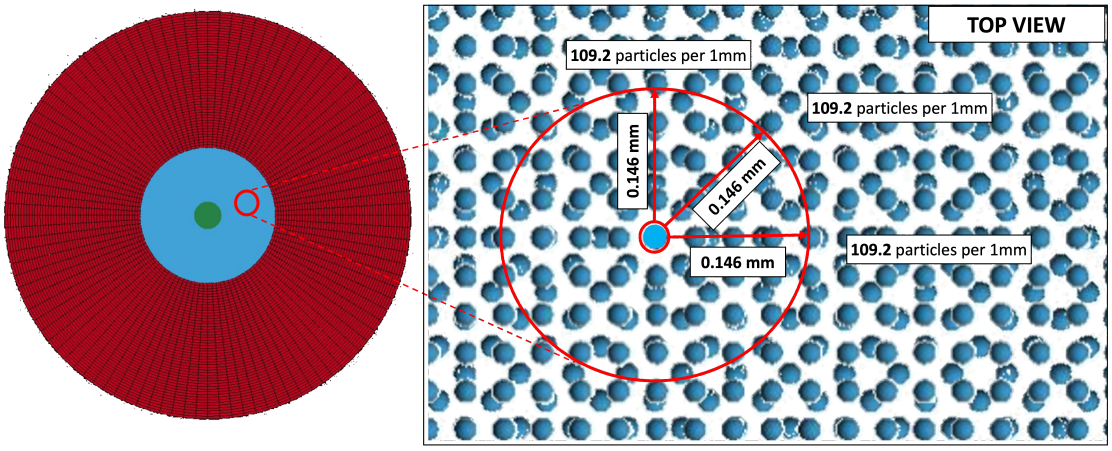

Figure 3.34: SPH lattice configuration in the quasi-isotropic model (top view).

Through this configuration, the particle density remains consistent both along the x and y axes and across the oblique direction. This uniformity is confirmed by the calculation of the average in-plane inter-particle distance along each of these directions. Since the number of layers rotated by 45° is equal to the number of layers in the standard configuration, the resulting average in-plane interparticle distance is simply the average of the values in the rotated and standard layers, resulting in 0.146 mm. Additionally, it is important to note that the average number of particles per millimeter remains consistent with this setup, with an average of 109.2 particles per 1 mm.

$$n_{x_{or}y_{or}45^\circ} = \frac{1mm}{0.146p/mm} \times 16 = 109.2\,p \tag{3.8}$$

3.7.4. Results

Figure 3.35 shows how stress waves propagate from the impact site to the entire plate in a tied contact configuration, with the SPH domain lattice arranged in a quasi-isotropic manner. Similar to the previous section, the results of stress wave propagation simulations conducted on the SPH quasi-isotropic lattice full model were compared with those conducted on the standard quarter model, shown in a red square in the upper right corner, to evaluate the influence of

the SPH lattice modification. Two subsequent time points, namely 10.5 and 12 microseconds post-impact, have been reported.

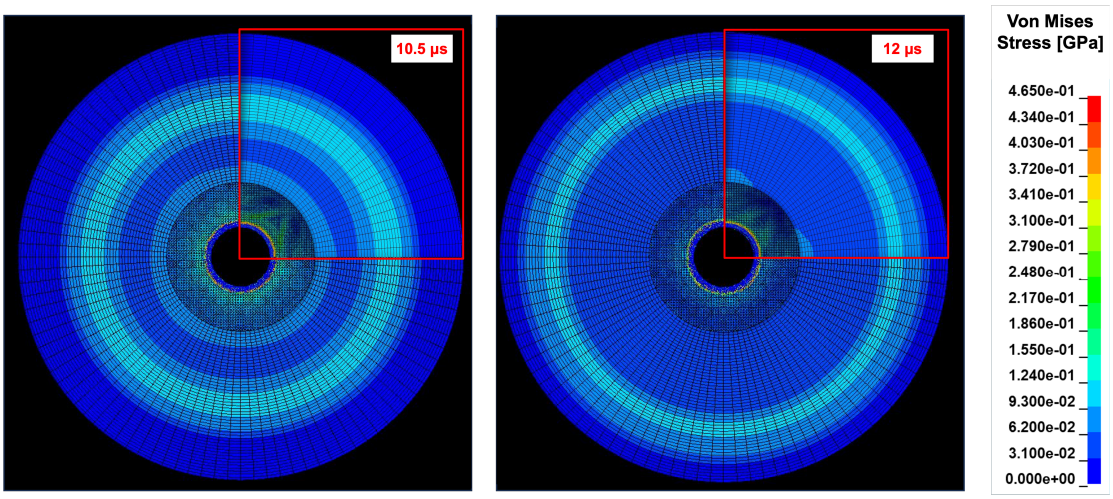

Figure 3.35: Stress wave propagation comparison between the full tilted model and the quarter straight model (in the right upper corner) in simulation with tied SPH/FEM contact interface and circular SPH domain at 10.5 and 12 µs after the impact. Red dashed lines highlighting the mismatched stress features (pictures from LS-DYNA Pre-Post V4.8).

The results indicate excellent axially symmetric stress propagation in the quasi-isotropic model. The propagation of stress waves in the rest of the material appears to be unaffected by the spatial configuration of the SPH lattice. No directional phenomena in stress propagation were detected through this analysis.

To assess the efficacy of the SPH quasi-isotropic configuration, the same test as described in previous sections has been conducted. Von Mises stress data were gathered at three specific locations along the SPH/FEM interface and are presented in Fig. 3.36. Two of these data points are positioned along the x and y axes, while the third is situated at a 45° angle. It is important to note that the collected data pertain to the FEM domain.

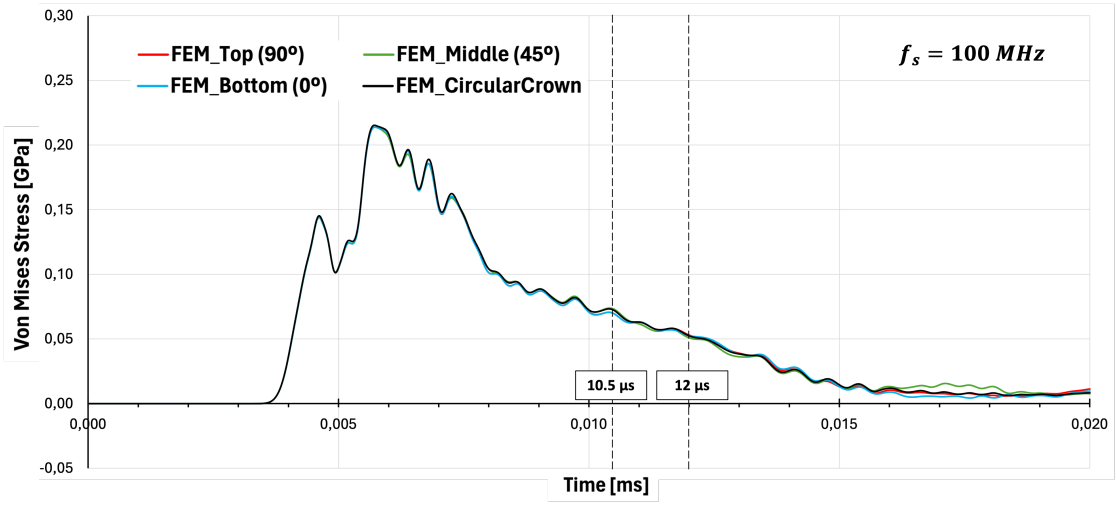

Figure 3.36: Von Mises stress data comparison in circular tied domain in FEM domain (quasi-isotropic SPH lattice configuration).

The graph confirms the findings of the previous analysis regarding the effect of SPH quasi-isotropic configuration on stress propagation. The plotted curves reflect the behavior observed in Fig. 3.31. The stress curves for the points located at a 45-degree angle, along the x- and y-axes, are very similar, overlapping each other and showing only minor discrepancies.

Although this strategy has only been implemented and verified for a plate with a circular external geometry, in the next chapter this methodology is implemented for a plate with a square external geometry. The reader can expect similar results of uniformity of stress wave propagation for the latter approach as well.

3.8. Summary

Chapter '*Simulation Methodology for Single-Plate Hyper-Velocity Impacts*' explains the methodological framework for the simulation of hyper-velocity impact within a single plate configuration. The analysis covers factors such as the shape of the SPH domain, the choice of the SPH/FEM coupling algorithm, and the initial spatial lattice configuration of the SPH particles, which influence the realism and accuracy of the simulation. The optimal configuration for successful simulation has been identified through the analysis of multiple aspects such as the continuity of stresses in the plate, the axially symmetric behavior of the stress wave propagation, and the evaluation of the internal reflection of the stress wave. Specifically, a full model with an adaptive SPH/FEM contact and a quasi-isotropic SPH lattice configuration emerges as the most effective approach.

The implemented models are initially validated and compared using experimental data from Sibeaud et al. This benchmarking process ensures the fidelity and reliability of the simulation methods in use. Subsequently, future simulations within a Whipple shield configuration will be performed using the identified optimal configuration. The purpose of these future simulations is to validate the model against experimental data.

In addition, the results of these experiments will provide broad insights that can be applied to various scenarios, thereby increasing the understanding within the field of HVI simulations. The methodology outlined serves as a solid foundation for subsequent research efforts, facilitating advances in both the theoretical understanding and practical applications of HVI simulations.

4

Simulation Methodology for Whipple Shield Hyper-Velocity Impacts

In this chapter, the model implemented for the simulation of HVI in a double-plate configuration, also known as a Whipple shield, is outlined. The model proposed in the following sections benefits from the comparative studies conducted on the single-plate scenario in Chapter 3. Specifically, the configuration with a circular-shaped SPH domain, adaptive SPH/FEM contact algorithm, and quasi-isotropic SPH initial lattice has been shown to provide high degree of realism and simulation accuracy.

To validate the proposed model, the simulation replicates one of the experimental Light Gas Gun (LGG) hyper-velocity impact tests conducted at the Ernst Mach Institute (EMI) in Freiburg, Germany [18]. The experimental data were obtained in the frame of an activity of Airbus Defence and Space under an ESA contract, and are courtesy of Airbus Defence and Space. Although the parameters that can be used for comparison are limited to crater diameters in the first and second plates, they are sufficient for the purposes of validating the implemented model.

The simulation has been performed using LS-DYNA R13.0.1 MPP Single Precision version and executed in parallel using 32 MPP processors from the High Performance Computing cluster of the Delft University of Technology Aerospace Faculty (HPC12). The computational burden was significant, with a CPU time of 100140 seconds (27 h, 49 min, 0 sec).

The following sections describe the test to be replicated (Section 4.1) and discuss the parameters that are critical to the proposed model (Section 4.2). Section 4.3.1 compares the experimental data with simulation results and explains the impact characteristics. Then, the energetic aspects of the simulation are analyzed in section 4.3.2. Finally, the study concludes with a comprehensive analysis of stress propagation induced by HVI in both the first and second plates (Section 4.3.3), along with observations regarding the vibration field (Section 4.3.4).

4.1. Whipple Shield HVI Experimental Test

In order to validate the methodology developed in the single-plate scenario also for a double-plate configuration, among the tests whose data were available, it was chosen to reproduce the test whose impact velocity was the highest (7.1 km/s) as it was considered to be the probable cause of the greatest damage to satellites.

In the replicated experiment, a 5 mm diameter spherical projectile made of Al 2007 is shot at 7.1 km/s using a LGG against a Whipple shield. The plates of the shield are made of Al 2024-T3 with a thickness of 0.8 mm and are fixed at the edge along the entire perimeter. The plates are assumed to be square, although their dimensions in the other two directions are not specified. To retrieve the stress level induced by HVI in both plates minimizing the boundary conditions interference, both plates were modeled with 300mm long external edges. The distance between the two plates is 60 mm. A schematic illustration of the test set-up is shown in Fig. 4.1 (a), while a real HVI Whipple shield testing set-up is displayed in Fig. 4.1 (b).

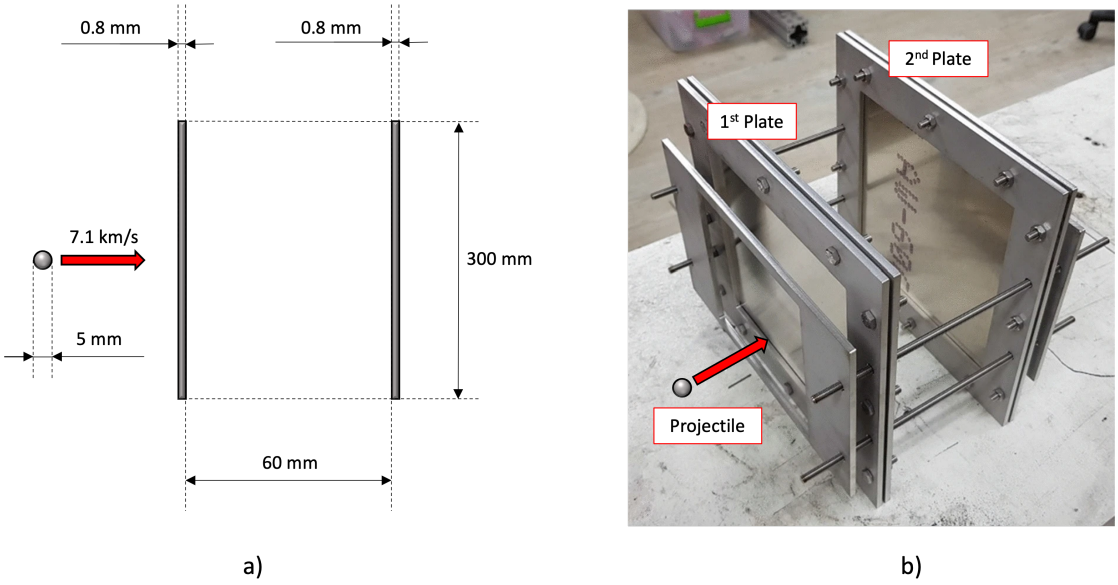

Figure 4.1: Target Geometry (a); Experimental set-up for HVI (adapted from [78]) (b).

Since the test campaign aimed to develop the ballistic curve of the analyzed shield and validate an early hydrocode used to model HVIs, the recorded results only indicate whether the target was penetrated and the relative diameter of the craters. In the experiment, both plates were perforated, and a 9.3 mm diameter crater was recorded on the first plate. A 58 mm diameter crater was reported on the second plate, caused by the debris cloud generated from the impact of the projectile with the first bumper. These data will be used for simulation validation in the following paragraphs.

4.2. Methodology

In this section, the methodological approach employed in simulating Whipple shield HVI is discussed. The methodology draws upon the comparative analysis conducted on the single-plate scenario, as well as a preliminary investigation outlined in Harazim's Master's thesis [38]. While

Harazim's thesis primarily pays attention to the mesh convergence study and material model approach for simulating HVI, thereby enriching the foundation of our investigation, the present study specifically focuses on analyzing stress propagation within the first and second plate after HVIs.

In Section 4.2.1, the primary geometrical parameters relevant to the simulation are presented. Special attention is given to the level of discretization used in the SPH parts. In Section 4.2.3, the main keywords utilized in LS-DYNA are described, with a specific focus on the contact definition between the FEM and the SPH domains, the implemented boundary conditions and material model.

4.2.1. Model Geometry

To replicate the tests conducted at EMI and validate the proposed methodological approach, the geometry was configured to closely resemble the experimental context outlined in Section 4.1. The simulation was designed to reproduce the behavior of a spherical projectile with a diameter of 5 mm and an initial velocity of 7.1 km/s. To optimize computational resources and minimize simulation time, the projectile was positioned just 1 mm away from the first plate, without physical contact. The target structure comprises two square plates arranged orthogonally to the projectile's initial trajectory, each with a thickness of 0.8 mm and a length of 300 mm.

The length of the plates was not specified in the experimental campaign reports. It was chosen to ensure unrestricted propagation of the stress waves in the first microseconds after impact, allowing a study unaffected by edge conditions and artificial reflections. The two plates were arranged at a distance of 60 mm from each other. Figure 4.2 presents a comprehensive view of the simulated system. The SPH modeled impact zone is shown in blue and the outer area of the plates modeled with finite elements in red.

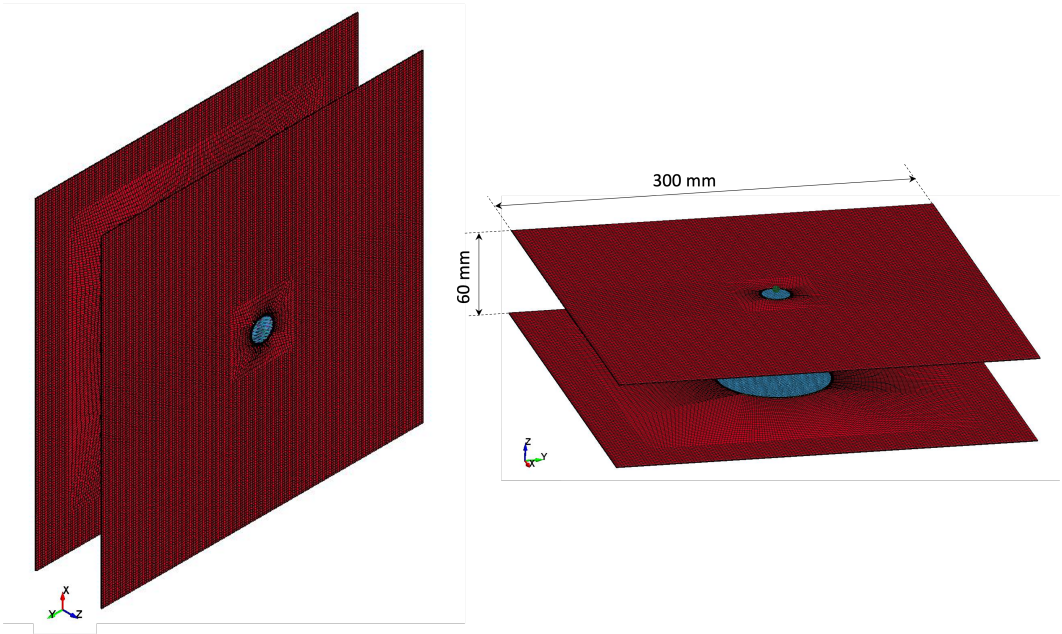

Figure 4.2: Whipple shield simulation geometry (pictures from LS-DYNA Pre-Post V4.8).

As in the single plate configuration described in Section 3.2, the projectile was modeled through the use of SPH particles, while the two plates were treated through finite elements, except for the impact areas, which were also modeled through SPH. To optimize computational efficiency, the size of the SPH domain related to the first plate was reduced compared to that related to the second plate.

This decision was based on the logic of a Whipple shield, which allows for a larger impact area on the second plate. Indeed, the fragmentation of the projectile, which occurred on the impact with the first bumper, generates a debris cloud characterized by a dispersion angle with respect to the initial direction of travel and a reduced velocity. This results in the kinetic energy being distributed over a larger area when it hits the second plate.

The SPH domain size was determined by analyzing experimental data regarding the diameter of the crater formed on the second plate, allowing sufficient room for discrepancies between simulated and experimentally observed results. Figure 4.3 highlights this modelling aspect by showing a bottom view of the simulated system. In the picture, both the SPH impact domains have been hidden.

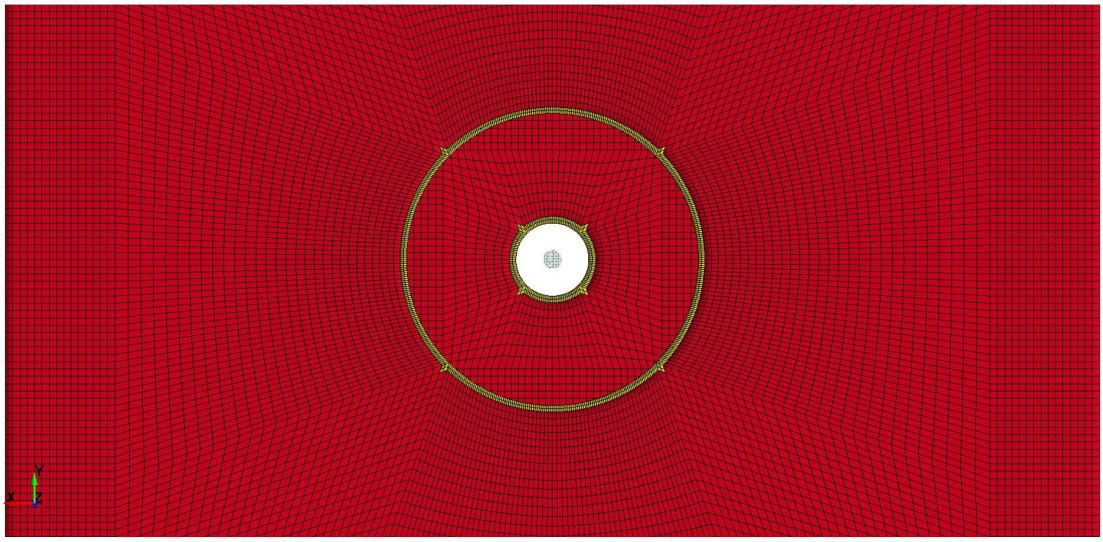

Figure 4.3: Detail of the Whipple shield simulation geometry (Bottom View - pictures from LS-DYNA Pre-Post V4.8).

Both SPH domains on the first and second plate were configured with a circular shape. This allows for a more uniform propagation of the stress waves from the SPH domain to the FEM domain, as shown in Sections 3.3 and 3.5.2. The diameter of the SPH domain of the first plate is 20 mm, while regarding the second plate, it was increased to 80 mm, consistently with the extension of the impact zone.

To guarantee a smooth transmission of stress waves from the SPH domain to the FEM domain in both plates, an adaptive contact was used. This is implemented through a transition zone, approximately 1.8 mm thick, comprising FEM-SPH hybrid elements (shown in yellow in Fig. 4.3).

4.2.2. Mesh Characteristics and Parameters

The SPH domain within the first plate consists of 241,246 particles. Within this domain, the in-plane interparticle distance is set at 0.125 mm, while 12 particles are utilized through the thickness to model 0.8 mm (resulting in an out-of-plane interparticle distance of 0.067 mm).

Despite recommendations to maintain a constant SPH interparticle distance [36], achieving this is challenging when maximizing particle count through the thickness. While the SPH mesh density in the first bumper determines the accuracy of the debris cloud, studies have shown that the number of particles through the thickness significantly influences crater diameter accuracy [59]. Therefore, it is crucial to maintain a fine mesh in the thickness direction, balancing it with the computational cost associated with SPH simulations.

Additionally, the first bumper consists of 45,559 finite elements and 544 hybrid FEM/SPH elements. A tailored FE meshing strategy has been implemented to ensure seamless transition from the circular internal interface to the square external edges. Figure 4.4 illustrates the first plate, highlighting the impact zone modeled by SPH (in blue) and the hybrid transition zone (in yellow).

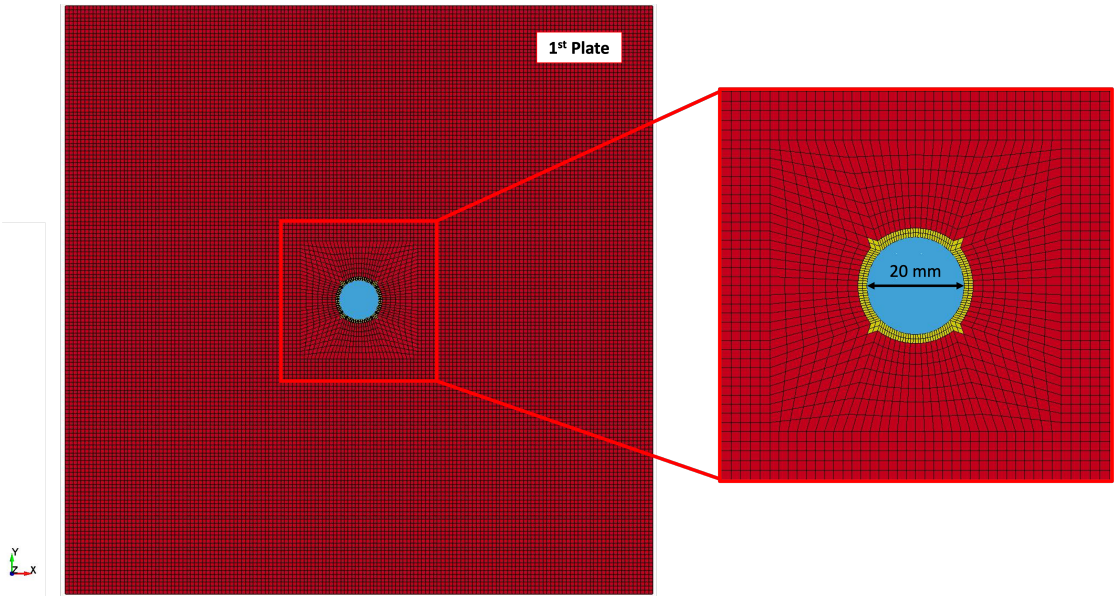

Figure 4.4: Geometry of the first plate in Whipple shield simulation (Top View - pictures from LS-DYNA Pre-Post V4.8).

The second plate's SPH domain encompasses 965,424 particles. Unlike the first plate, the interparticle distance in the plane is set at 0.250 mm, which is double the value compared to the first plate. Similarly, through the thickness, 12 particles are employed to model 0.8 mm, resulting in an out-of-plane interparticle distance of 0.067 mm.

Complementing the SPH domain, the second bumper incorporates 37,312 finite elements and 1,952 hybrid FEM/SPH elements. Once again, a tailored meshing approach has been adopted to ensure seamless transition from the circular internal interface to the square external edges. Figure 4.5 provides a visual representation of the second plate, highlighting the SPH-modeled impact zone (depicted in blue) and the hybrid transition zone (depicted in yellow) with detailed

focus.

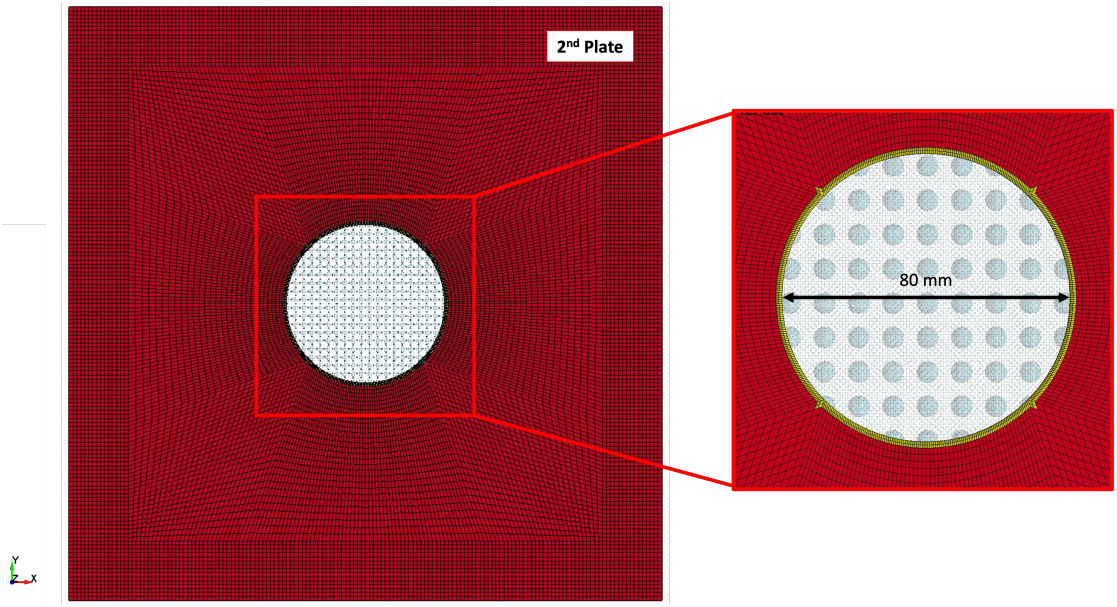

Figure 4.5: Geometry of the second plate in Whipple shield simulation (Top View - pictures from LS-DYNA Pre-Post V4.8).

Hence, across both plates, the SPH region contains 12 particles throughout the plate thickness, while the FEM region has only 2 elements. The simulated scenario uses a projectile consisting of 33,552 particles, with an interparticle distance of 0.125 mm along the x, y, and z axes.

The mesh parameters are tabulated in Table 4.1.

	1st Plate	2nd Plate	Projectile
Domain dimensions	Ø 20 x 0.8 mm	Ø 80 x 0.8 mm	Ø 5 mm (sphere)
Particles in prin. direction	160 x 160 x 12	320 x 320 x 12	40 x 40 x 40
Ratio [mm/particles]	0.125 x 0.125 x 0.067	0.250 x 0.250 x 0.067	0.125 x 0.125 x 0.125
Total number of particles	241,246	965,424	33,552

Table 4.1: SPH Mesh parameters in Whipple shield HVI simulation.

As discussed in Section 3.7, to ensure uniformity in SPH behavior, particularly concerning the propagation of stress waves generated by the HVI, a quasi-isotropic lattice was also proposed in this scenario. This approach has been implemented for both the first and second plates. Both SPH zones use 12 particles to discretize the plate thickness. In order to achieve a quasi-isotropic lattice, as both the SPH zones use 12 particles to discretize the plate thickness, the lay-up strategy depicted in Fig. 4.6 has been implemented.

By ensuring symmetry with respect to the mid-plane of the plate and balance of the lattice, this approach allows for greater uniformity of stress propagation within the plane.

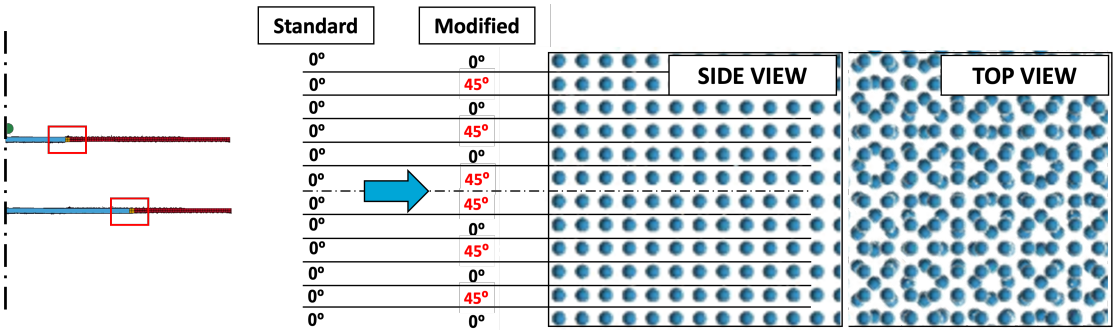

Figure 4.6: Lay-up strategy of the quasi-isotropic SPH lattice in the Whipple shield (side and top view).

4.2.3. Model Simulation Parameters

The present model leverages the previous results obtained from the single-plate simulation. Consequently, many of the modeling parameters and simulation characteristics have been determined through a comparative analysis of the results obtained from previous simulations. While this section aims to provide the reader with a comprehensive overview of the most important LS-DYNA keywords related to the Whipple shield HVI simulation, in order to avoid unnecessary repetitions, it will often refer back to the single-plate model described in Section 3.2, highlighting similarities and differences. For further details, please refer to Appendix B.

For the proposed simulation, a clamping boundary condition was applied along the outer edges of both plates using the ***BOUNDARY_SPC_SET** card. This choice was made because no symmetry plane of the model was exploited. Although this does not fully replicate the experimental conditions, it does not significantly stiffen the plates or affect the size of the generated craters, given the distance of the edges from the impact area. There have been no changes to the simulation control parameters for either the SPH or FEM domains. However, to prevent software crashes, the initial number of neighbors per particle was increased to 850.

To fully observe the HVI phenomenon on a Whipple shield, the termination time, defined by the ***CONTROL_TERMINATION** card, had to be extended. Based on simulations conducted on a single plate, the estimated value for the time required to travel the stand-off distance relative to the analyzed Whipple shield, and the average shock wave propagation velocity within the plates was conservatively set at 100 µs. No other simulation termination parameters were used. Furthermore, the initial velocity of the projectile, defined by the ***INITIAL_VELOCITY_GENERATION** card, was adjusted accordingly, allowing the projectile to impact the bumper at a velocity of 7.1 km/s.

Considering the material model employed in this simulation, given the favorable performance reported in single plate tests and its widespread utilization in literature, the Johnson-Cook material model and Grüneisen EOS were adopted. As outlined in Section 4.1, the original experimental test envisaged the use of two different aluminum alloys for the plates and the projectile, Al 2024-T3 and Al 2007, respectively. Due to a lack of values in scientific literature for the Johnson-Cook material model and Grüneisen EOS parameters for Al 2007, it was decided to model all three components using Al 2024-T3 aluminium alloy.

This choice has been taken, considering the fact that in HVIs the material's strength properties become negligible due to the immense pressures generated during impact, surpassing the material's strength limits, and the penetration capability is mostly ruled by the density of the projectile material [17]. Al 2024-T3 and Al 2007 not only have comparable densities but they also show overall similar material properties. For the aforementioned reason, the Johnson-Cook model for Al 2024-T3 to represent the projectile instead of the Al 2007 model has been considered valid. It is also noteworthy that in this simulation, the Johnson-Cook damage model was not employed due to its tendency to overly estimate crater formation on the second plate [38].

Detailed input parameters for the LS-DYNA ***MAT_JOHNSON_COOK** and ***EOS_GRUNEISEN** keywords are provided in Tables 4.2, 4.3, and 4.4.

Material Property	Symbol	Value
Density	ρ	$2.785 \quad g/cm^3$
Elastic Modulus	E	$73.1 \quad GPa$
Shear Modulus	G	$28.6 \quad GPa$
Poisson's Ratio	ν	0.33
Melting Temperature	T_m	$775 \quad K$
Reference Temperature	T_0	$294 \quad K$
Specific heat	c_p	$875 \quad J/kgK$

Table 4.2: Material properties of Al 2024-T3 aluminum alloy [11].

Johnson-Cook parameters	Symbol	Value
Yield Stress	A	$369 \quad MPa$
Strain Hardening parameter	B	$684 \quad MPa$
Strain Hardening exponent	n	0.73
Strain Rate parameter	C	0.0083
Thermal Softening exponent	m	1.7
Pressure Cut-off	σ_p	$-1200 \quad MPa$
Spall type	$SPALL$	2.0
Damage Constant 1	D_1	0.13
Damage Constant 2	D_2	0.13
Damage Constant 3	D_3	-1.5
Damage Constant 4	D_4	0.011
Damage Constant 5	D_5	0

Table 4.3: Johnson-Cook material model parameters for Al 2024-T3 aluminum alloy [11].

Grüneisen parameters	Symbol	Value
EOS Constant 0	C	$5240 \quad m/s$
EOS Constant 1	S_1	1.338
EOS Constant 2	S_2	0
EOS Constant 3	S_3	0
Grüneisen parameter	Γ_0	2.00
A factor	A	0.48

Table 4.4: Grüneisen EOS parameters for Al 2024-T3 aluminum alloy [11].

Finally, as previously mentioned, an adaptive contact using hybrid SPH/FEM elements has been

implemented in both plates to ensure a smooth connectivity between the SPH and FEM domains. This contact method, as explained in Sections 4.2.1 and 3.2.3, requires the creation of a transition domain consisting of hybrid SPH/FEM elements, defined by the LS-DYNA keyword ***DEFINE_ADAPTIVE_SOLID_TO_SPH**.

The keyword DEFINE_ADAPTIVE_SOLID_TO_SPH allows users to specify the number of SPH particles generated per element. In the transition zone that bridges the SPH and FEM domains of the Whipple shield simulation, 27 SPH particles are generated for each hybrid hexahedral element (3 along each direction). This quantity represents a balanced compromise between computational efficiency and accuracy. It should be noted that the transition zone is located well away from the point of impact, which eliminates the need for a higher number of particles. However, to ensure optimal connectivity, it is recommended to aim for a SPH particle density in hybrid elements similar to that of the pure SPH zone that is intended to be interconnected.

Figures 4.7 and 4.8 show a detailed view and a top-down perspective of the SPH/FEM adaptive interface within the bumper and the second plate, respectively. The hybrid domain, consisting of solid elements and SPH particles, is rendered in yellow. For clarity, some elements have been blanked out to show the presence of brown SPH particles within. Once the number of particles per hybrid element along each direction is set in the adaptive elements control options, in order to ensure a similar SPH particle density both within the SPH impact domain and across the hybrid interface, the original mesh size of the finite elements within the bridging domain is halved.

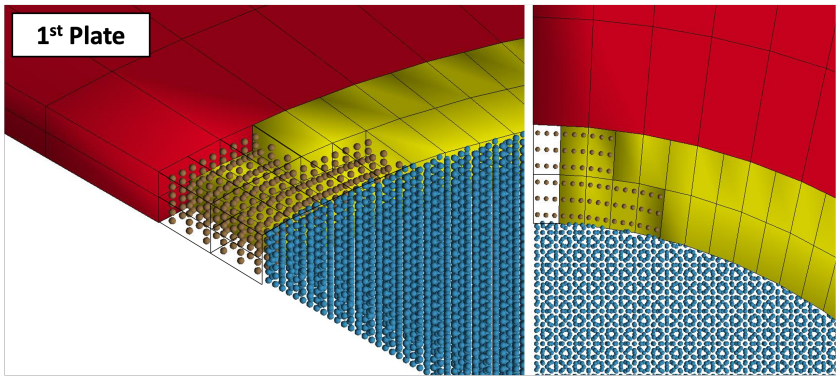

Figure 4.7: Detail of the SPH/FEM adaptive contact through hybrid elements in the 1^{st} plate.

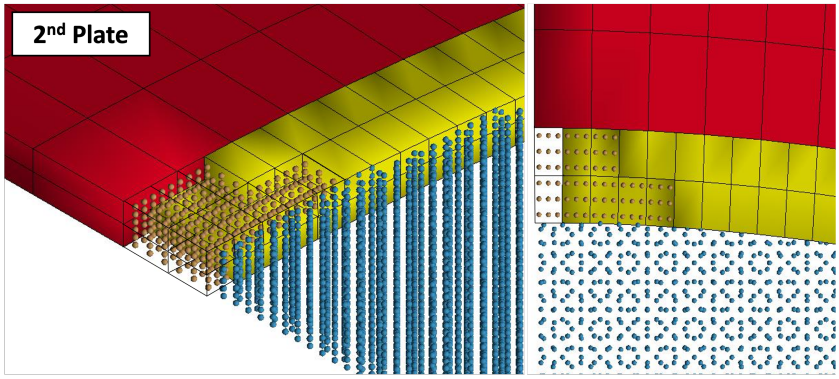

Figure 4.8: Detail of the SPH/FEM adaptive contact through hybrid elements in the 2^{nd} plate.

The transition domain is linked to the finite elements domain side utilizing the ***CONTACT_TIED_SURFACE_TO_SURFACE** keyword, whereas on the SPH domain side, the ***CONTACT_TIED_NODES_TO_SURFACE** keyword is employed.

4.3. Results

The results obtained from the Whipple shield HVI simulation are shown. Initially, in Section 4.3.1 the simulation outcomes will be compared with the post-impact experimental geometrical data of the crater dimensions on the first and second plate to validate the simulation methodology. To evaluate the effectiveness of the Whipple shield system in protecting space structures from HVI, this study analyzes the changes in the velocity profile of the impacting debris before and after passing through the second plate. By examining these velocity changes, we can assess the shield's ability to mitigate the kinetic energy and potential damage caused by the debris. As performed in the single plate scenario, the energy conservation is also monitored in Section 4.3.2.

Subsequently, in Section 4.3.3 stress propagation analysis is undertaken through a comparison of stress levels observed in the first and second plates. Additionally, insights concerning the vibration behavior induced by the impact are discussed in Section 4.3.4.

4.3.1. General Behaviour

In the context of the current simulation, validation of the methodology can only be achieved through comparison with experimental data. However, unlike the single plate test, the available data solely pertains to the post-impact crater dimensions, with no accompanying information regarding the velocity or geometry of the debris cloud following the impact.

Figure 4.9 shows the craters caused by the projectile and by the resulting debris cloud on the bumper and second plate, respectively.

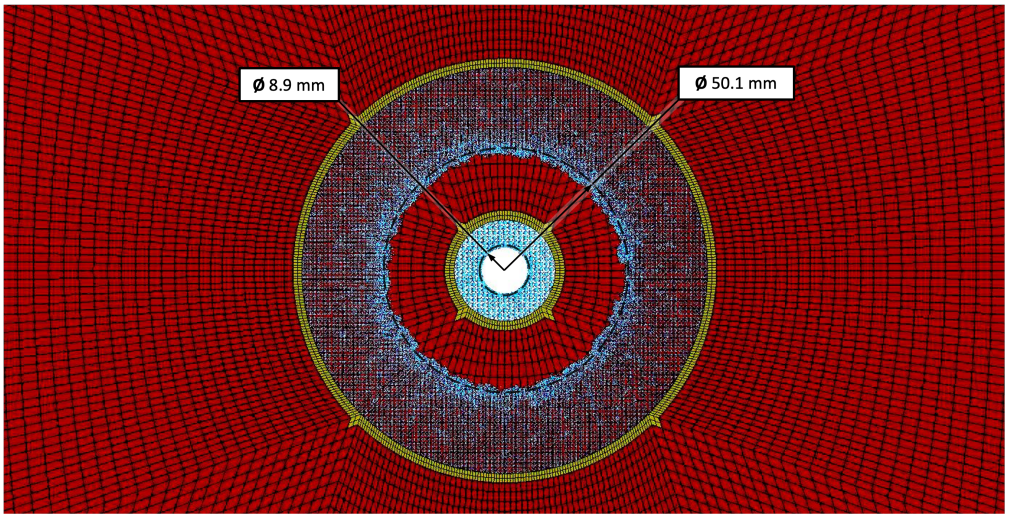

Figure 4.9: Craters detail in Whipple shield HVI simulation (Bottom View - pictures from LS-DYNA Pre-Post V4.8).

In accordance with the simulation methodology, both craters display a circular shape, with their edges located far away from the hybrid coupling domain. Table 4.5 presents a comparative

analysis of the diameter size of the craters and the corresponding relative errors.

	1st Plate	2nd Plate
Experimental data	9.3 mm	58 mm
Simulation data	8.9 mm	50.1 mm
Relative Error	4.49 %	15.77 %

Table 4.5: Crater diameter results and relative errors in the Whipple shield HVI simulation. Experimental data courtesy of Airbus Defence and Space [18].

By comparing the dimensions of the experimental and simulated craters and analyzing the relative errors, it is observed that the error in the first plate is consistent with the errors observed in the single plate simulations. Regarding the crater in the second plate, the 15% discrepancy may be due to several factors. One possibility is that the limited duration of 100 microseconds does not allow for the complete development of the crater, or it could be due to inaccuracies in the input and output data. Additionally, this discrepancy could be indicative of the inherent uncertainties and non-deterministic nature of HVI phenomena. It is also possible that a combination of these factors contributes to the observed error.

In addition to the aforementioned observations, the simulation confirmed the effectiveness of the Whipple shield system in protecting spacecraft from HVI. Although penetration occurred in both the first and second plates, the velocity decreased significantly, resulting in a substantial reduction in the associated kinetic energy of the impact.

The velocity profile at different time steps is displayed in Fig. 4.11. It can be observed that the first plate has a limited effect on reducing the velocity of the projectile. Although the projectile is fragmented after the initial impact, it still retains the majority of its initial kinetic energy. However, the subsequent impacts of the fragments within the debris cloud on the second plate result in a significant reduction in velocity. The trend is demonstrated by analyzing the average velocity of the debris cloud during the simulation, as shown in Fig. 4.10. The largest reduction in velocity occurs as a result of the impact with the second plate, accounting for an 87.7% reduction, whereas the impact with the first plate only contributes to a 14% reduction.

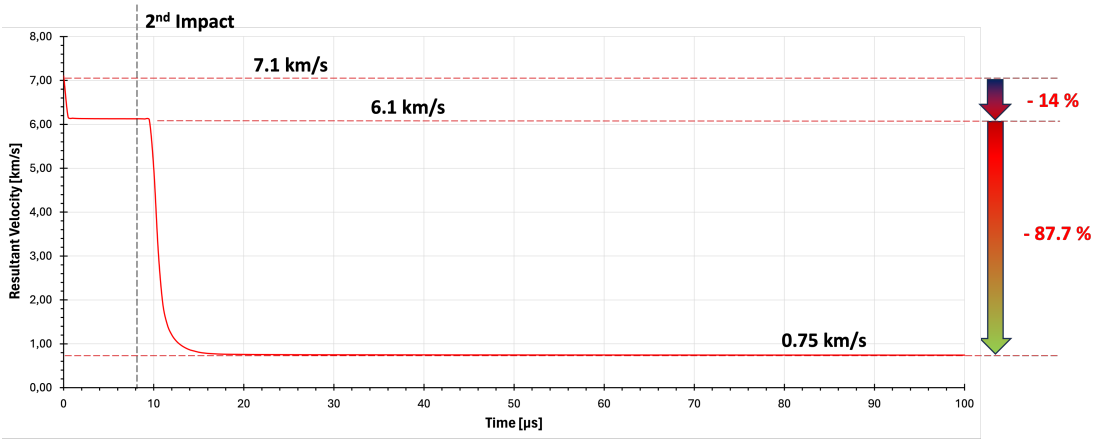

Figure 4.10: Average debris cloud velocity in Whipple shield HVI simulation.

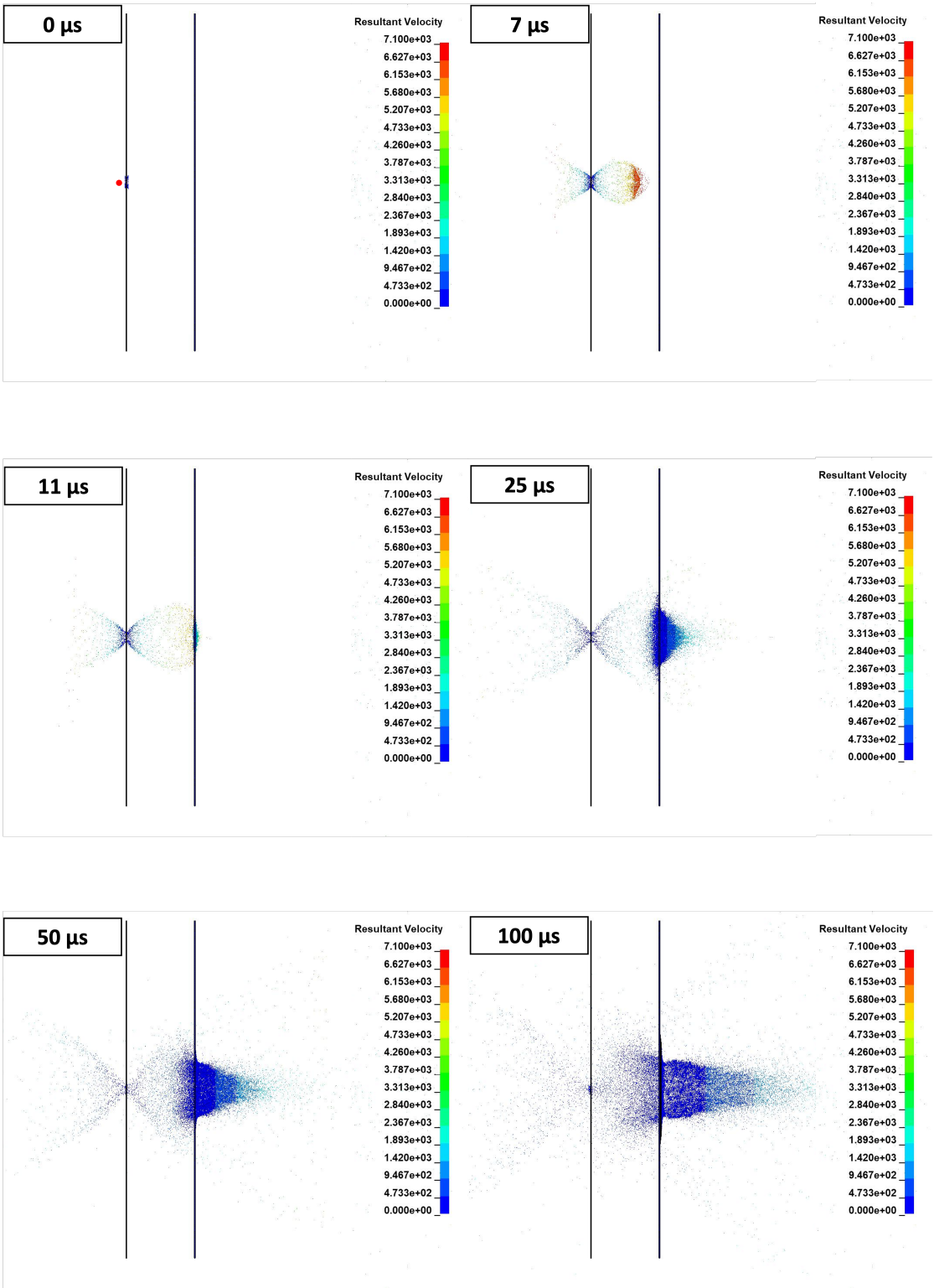

Figure 4.11: Resultant velocity [m/s] profile at different time steps in Whipple shield.

Similarly, plotting the variation of kinetic energy over time, as shown in Fig. 4.12, reveals that the impact with the second plate absorbs most of the kinetic energy (82.5% reduction). Therefore, the primary purpose of the bumper is to fragment the projectile and increase the following impact area.

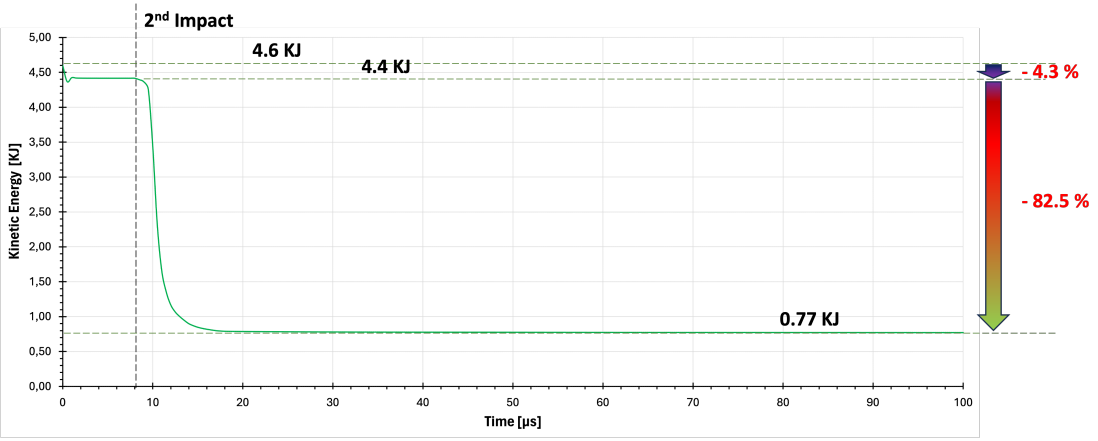

Figure 4.12: Kinetic Energy in Whipple shield HVI simulation.

While the pattern remains consistent for both kinetic energy and the average velocity of the debris cloud, with major significant reductions occurring during impacts with the plates — of which the second one far exceeds that of the first — it is important to justify why the overall reduction in the advancement velocity of the debris cloud (89.4%) is larger than that recorded for the kinetic energy (83.3%).

This difference can be explained by the fact that each impact sets a greater mass in motion. As a result, the velocity, which parabolically governs the value of the kinetic energy, sets the trend, and the mass, which is set in motion by subsequent impacts, defines the differences.

4.3.2. Energy consideration

As already discussed in the Section 3.4, LS-DYNA, being an explicit dynamic solver, prioritizes mass and momentum conservation over energy conservation when simulating short-time, high-intensity events. Therefore, it is crucial to monitor energy conservation throughout the simulation process to ensure the validity and accuracy of results.

Minimal total energy variation indicates effective error management and error minimization strategies. Energy fluctuations can be quantified using either *Energy Error* or *Energy Ratio*. Their formulations are given in Eqs. (3.1) and (3.2), respectively. However, an energy imbalance does not necessarily signify incorrect results. If the user comprehends the sources and sinks of energy within the system, and can account for these variations appropriately, the simulation can still be considered reliable. For example, during metal machining, if there is forced movement of the tool during the simulation that introduces additional energy into the system as external work. Understanding and accurately modeling this external energy input allows the resulting energy imbalance to be correctly interpreted, ensuring the validity of the simulation results.

In Fig. 4.13 the Total, Kinetic and Internal Energy evolution of the Whipple shield HVI simulation

is shown. Similarly, in Fig. 4.14 the Energy Ratio is displayed.

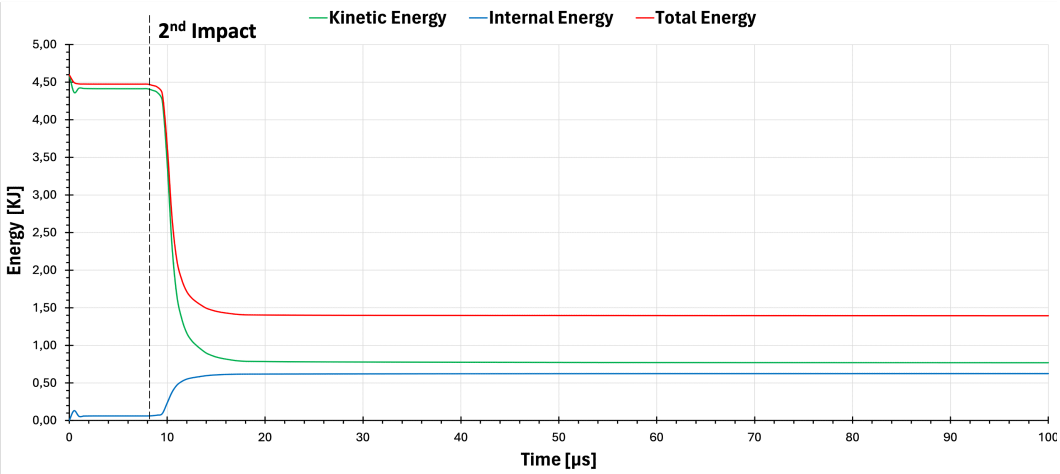

Figure 4.13: Total, Kinetic, and Internal Energy in Whipple shield HVI simulation.

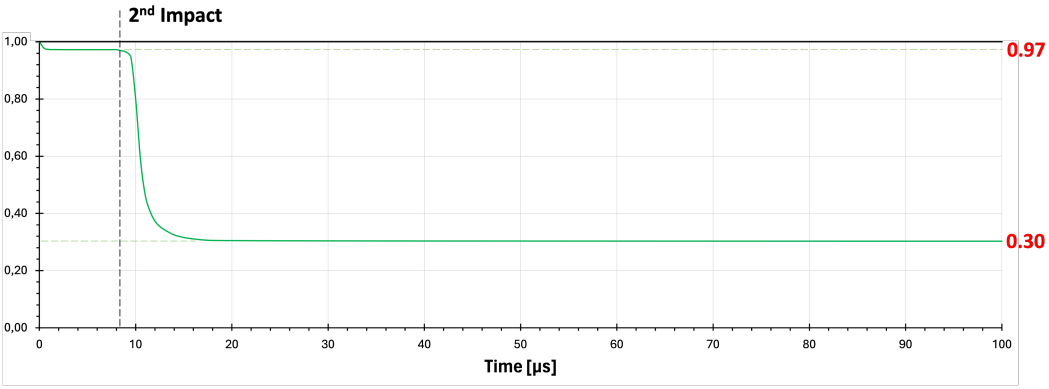

Figure 4.14: Energy Ratio in Whipple shield HVI simulation.

The simulation in this chapter shows that there is significant energy dissipation, especially during the impact of the debris cloud with the second panel, resulting in a total energy loss of about 70%. As expected, some of the kinetic energy is converted to internal energy during both impacts. However, most of it is dissipated. This behavior is similar to the observations made in Section 3.4 related to the single panel simulations, but it is more severe in the Whipple shield scenario. It should be noted that the hourglass energy is not displayed in Fig. 4.13, as it is deemed to be negligible. In fact, it does not exceed 0.15 J until the termination time set for the current simulation.

A previous study attributed the error to a flaw in the solver's energy calculation logic [38]. Specifically, instead of using a dedicated SPH methodology, the energy calculation was carried out using finite element logic. As we are utilizing the same software version (LS-DYNA R13.0.1), it is probable that the same underlying solver error is impacting our simulation. However, developers have observed that the introduced error primarily affects only the energy calculation and not the entire simulation results [38]. Despite previous efforts to mitigate this issue through interventions such as including thermal simulation and changing the artificial viscosity formulation, the primary cause remains related to interactions between SPH particles from different parts, and

thus no improvements have been achieved [38]. While single plate experiments remain within acceptable energy loss levels (as described in Section 3.4), double plate simulations highlight the magnitude of this issue.

4.3.3. Stress-Wave Analysis in the Plates

This section discusses the stress induced by hyper-velocity impact and its propagation from the impact region to the rest of the model. Both the first and second plates will be analyzed, considering their differences and similarities.

The analysis of HVI induced stress waves in satellites is critical to ensure continued structural integrity and operational reliability. As instruments become more sensitive, the need for stable platforms capable of withstanding external disturbances gains emphasis. The effects of micrometeoroids and space debris impacts should not be underestimated.

HVI stress waves can cause localized plastic deformation and structural damage that can degrade the performance of critical spacecraft equipment, especially when located near hinges, moving elements, optics, or electronic subsystems. The impact usually generates a single pulse in the direction of the projectile's trajectory into the spacecraft wall, with a peak velocity similar to that of the impacting projectile itself. The shock wave's amplitude decreases considerably as it moves away from the impact point and decays into an elastic wave as it propagates through the surrounding structure.

By conducting a thorough analysis of stress wave propagation after impact, researchers can identify vulnerable areas in spacecraft structures and develop targeted mitigation strategies to increase resilience against the increasing threat of HVIs. Simulations are crucial in bridging the gap between experimental analysis and real-life impacts, significantly reducing the costs associated with HVI testing while also improving reliability.

In Figs. 4.15 and 4.16, the von Mises stresses detected on both the first (left column) and second (right column) plates are depicted. The most significant instants of the initial phase of the HVI phenomenon have been selected for representation. The first and second plates have been juxtaposed to allow for comparison, enabling the appreciation of differences and similarities. For certain instants during which the region affected by the shock wave was still confined within the SPH domain, and thus less clear from the images, a zoom of the area of interest has been provided.

The debris cloud's impact with the second plate is observable. Indeed, the stress in the second plate is null for the initial two instants, followed by the shock caused by the impact that occurs at about 7 microseconds. This observation is consistent with the lateral view of the simulation evolution shown in Fig. 4.11. The final time step of the results shown in figure has been chosen to observe until the reflection, induced by the boundary conditions, of the first shock wave in the second plate. The maximum stress value shown in the figure (depicted in red) roughly corresponds to the ultimate tensile stress value of the material. A black background has been applied to enhance image clarity.

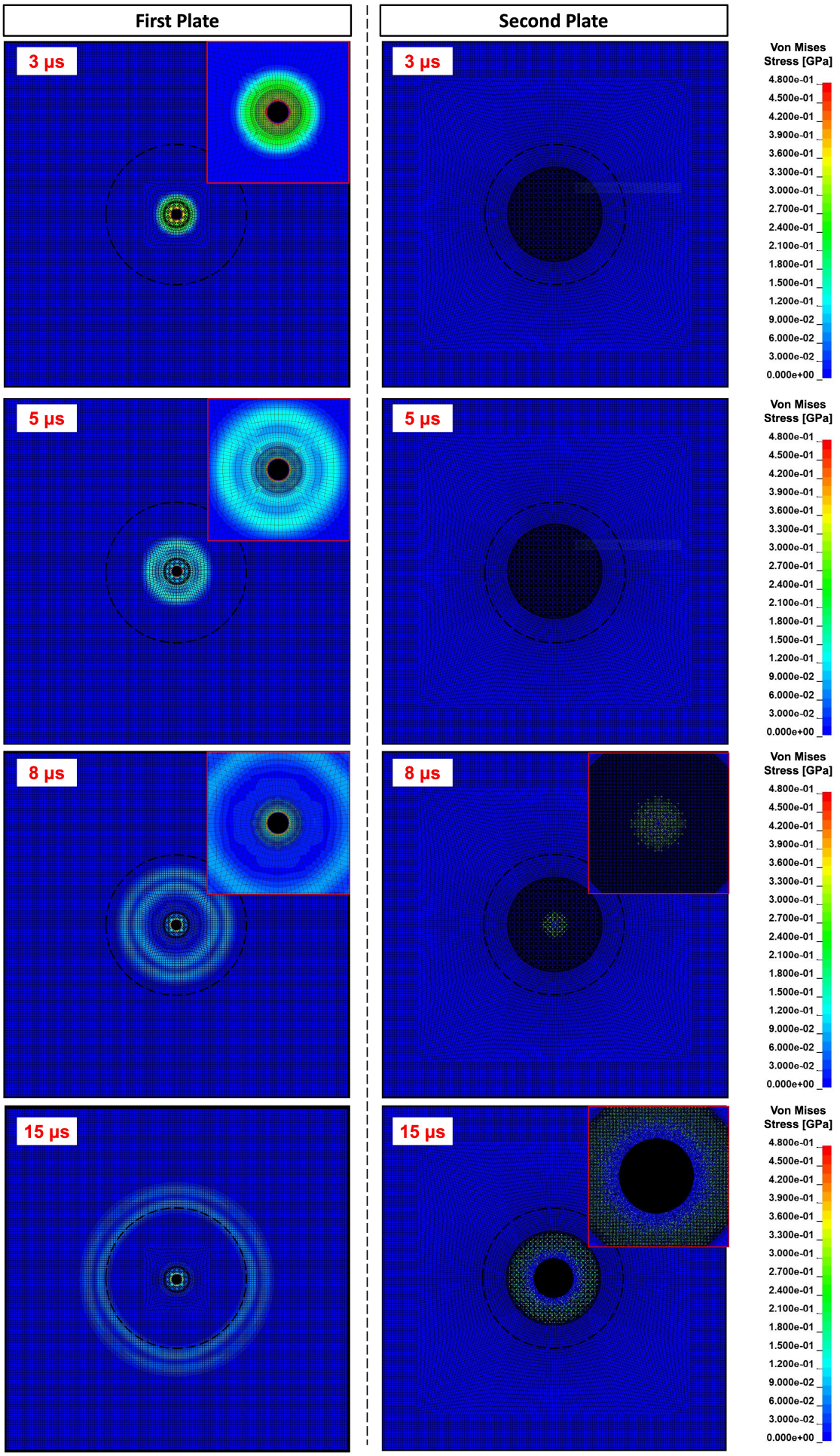

Figure 4.15: Von Mises Stress in Whipple shield HVI simulation (from 3 to 15 µs).

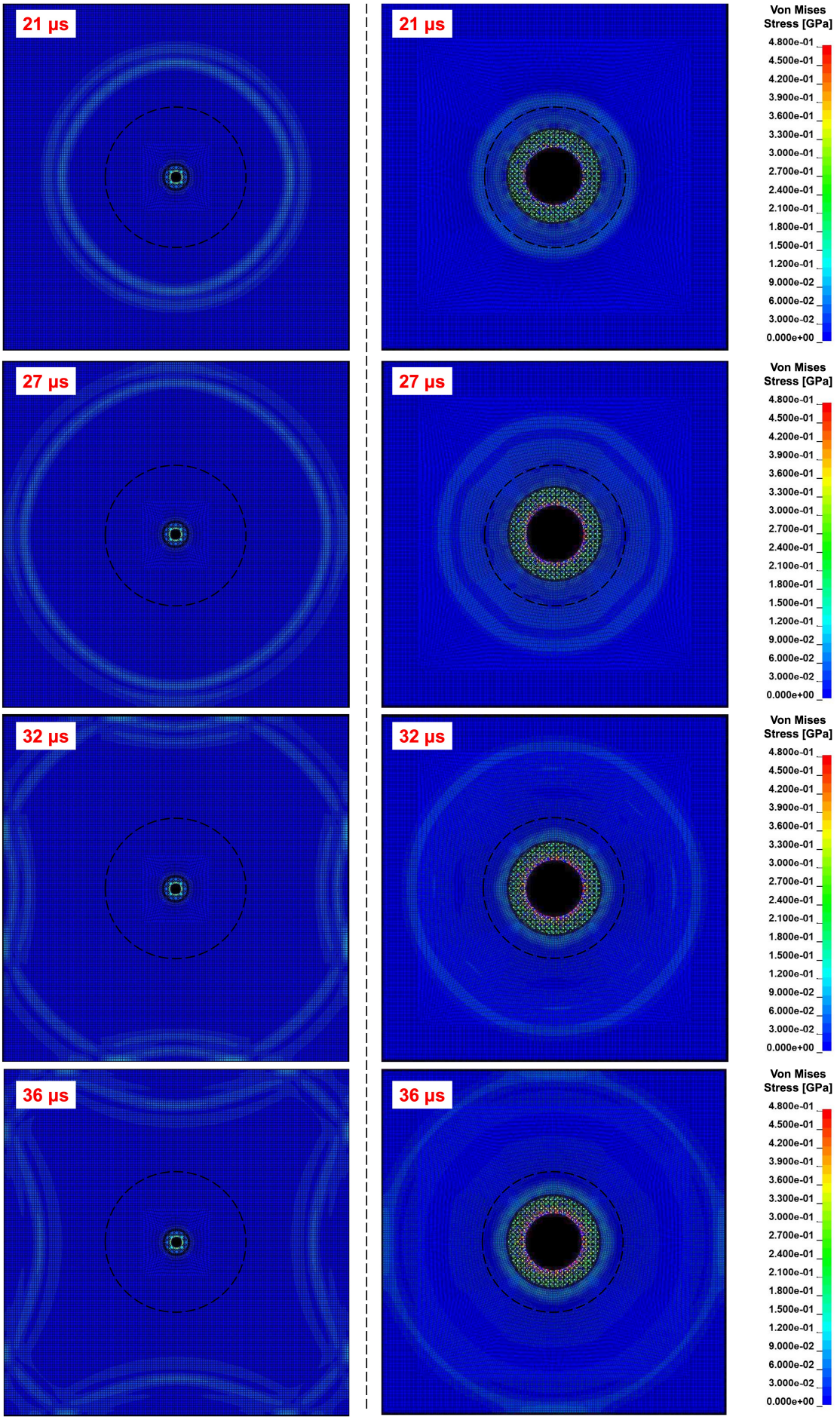

Figure 4.16: Von Mises Stress in Whipple shield HVI simulation (from 21 to 36 µs).

The findings suggest a distinct response of the two plates to the impact event, with the first plate exhibiting a more localized and transient stress distribution, whereas the second plate experiences a broader and lasting deformation. The images allow for the observation of stress level evolution, which is higher in the first plate immediately after the impact and in the vicinity of the perforation zone compared to the second plate. However, while in the first plate the stresses diminish as the shock wave propagates towards the outer regions of the structure, with a progressive decrease in intensity highlighted by the transition from green to light-blue color, in the second plate, the perforation caused by the debris cloud results in a more extensive local permanent plastic deformation, inwardly bending a wide domain of the plate (Fig. 4.17). Since the first plate was the first to be involved in the impact phenomenon, the stress induced in the top plate reaches the edges more quickly and are mirrored on them.

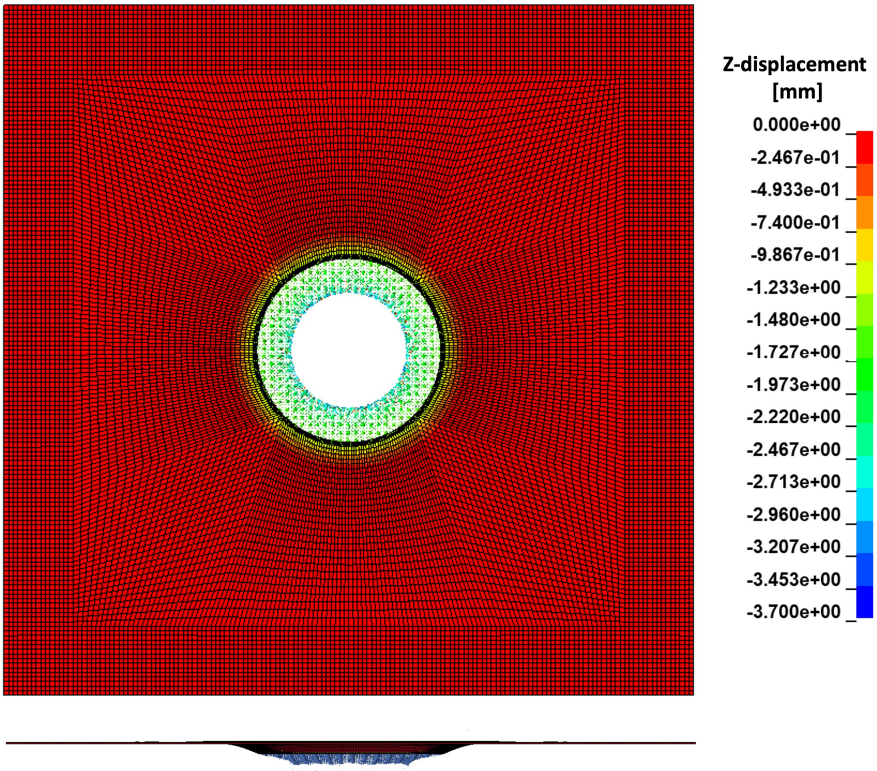

Figure 4.17: Post-impact geometry of the second plate. Representation of the displacement in x3 scale.

Further investigation into the temporal evolution and spatial distribution of stresses could yield profound insights into the behavior of the Whipple shield under HVIs. To conduct both qualitative and quantitative analyses of the induced stress propagation, the temporal variation of von Mises stress values throughout the simulation duration at specific points on both the first and second plates is studied. Indeed, by systematically examining the stress distribution over time and across different spatial points, a comprehensive understanding of the shield's response to high-velocity impact scenarios can be achieved.

Figures 4.18 and 4.19 present the von Mises stress values for the bumper and second plate, respectively. The stress values correspond to points located along a circumference with a radius of 60 mm, within the FEM domain. By comparing equidistant points, this analysis enables the

examination of stress wave directionality. This allows for the study of its axial symmetrical shape, especially during the initial phase of wave propagation and before reflection at the boundary. The analyzed plate is shown on the right side in both figures, along with a dashed circumference from which the data are gathered. The analyzed points are marked with stars whose colors correspond to the color of the curves. These points are located at 90°, 45°, and 0° angles relative to the x-axis, with positive angles measured counterclockwise. In addition, both figures include dashed vertical black lines that overlay the stress curves, corresponding to the temporal instants shown in Figs. 4.15 and 4.16. Furthermore, within those images, a dashed circumference with a diameter of 120 mm is discernible, which serves as a visual aid for comparing signals with the following graphs.

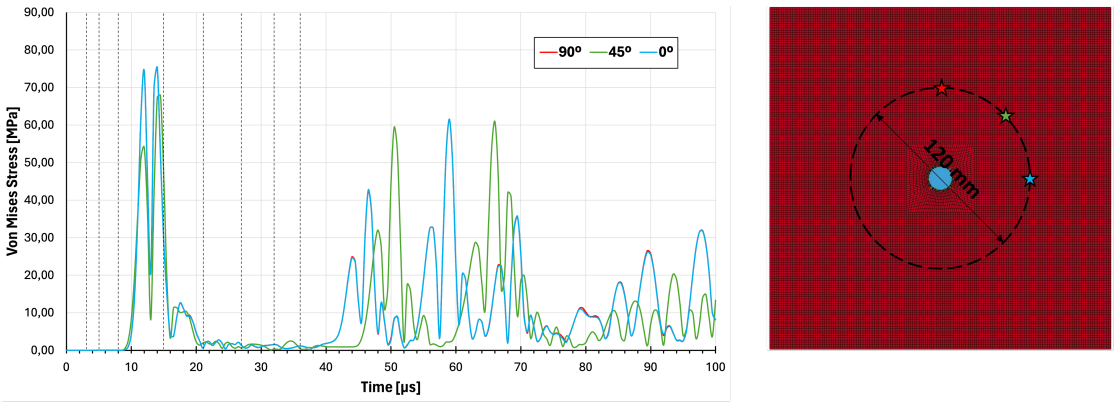

Figure 4.18: Comparison of von Mises stresses measured at points equidistant from the centre on the first plate.

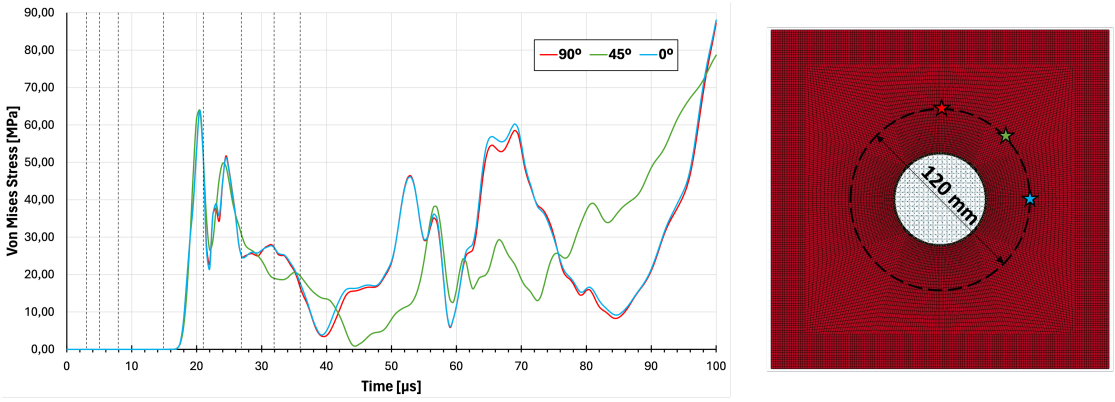

Figure 4.19: Comparison of von Mises stresses measured at points equidistant from the centre on the second plate.

Both the bumper and second plate exhibit a high degree of signal correspondence regardless of the direction of stress wave propagation, especially in the early stages of the phenomenon. The overlap between the points positioned at 0 and 90 degrees is almost 100%, but there is also a high level of correlation with the point at 45 degrees.

Concerning the first plate, the correspondence is excellent among the three signals. However, from 42µs onward, when the analyzed points are impacted by the waves reflected at the boundaries, this correlation diminishes. Reflection generates patterns that no longer adhere to the assumption of axial-symmetry. As the simulation progresses, the recorded stress levels exhibit

a decreasing trend, although they fail to reach zero level. It is probable that a longer simulation duration would have allowed for the observation of this result once the plate dynamics had terminated. Similar considerations can be made regarding the second plate. The initial correlation is strong, but it diminishes as the simulation progresses and reflections occur at the boundaries. However, as for the bumper, the correlation between the points at 0 and 90 degrees remains even after reflection. It is plausible to assume that the increase in stress value at the end of the simulation is consistent with plastic deformation in the vicinity of the formed hole.

Continuing the analysis, Figs. 4.20 and 4.21 depict the von Mises stress values corresponding to points located along a specific direction at various distances on both the first and second plates, respectively. These points are positioned at 60, 95, and 130 mm away from the plate center along the x-axis. This analysis allows the study of the propagation and attenuation of the stress wave by comparing points along the same direction. Again, each figure includes the plate relevant to the analysis on the right, with stars highlighting the examined points. The colors of the stars correspond to the colors of the curves. Additionally, a gray curve representing stress detected at a point 15 mm away from the crater's edge is included in the figure for comparative analysis of stress levels in areas adjacent to the crater. Similar to the previous analysis, vertical black lines are overlaid on the stress curves to indicate temporal instants corresponding to Figs. 4.15 and 4.16.

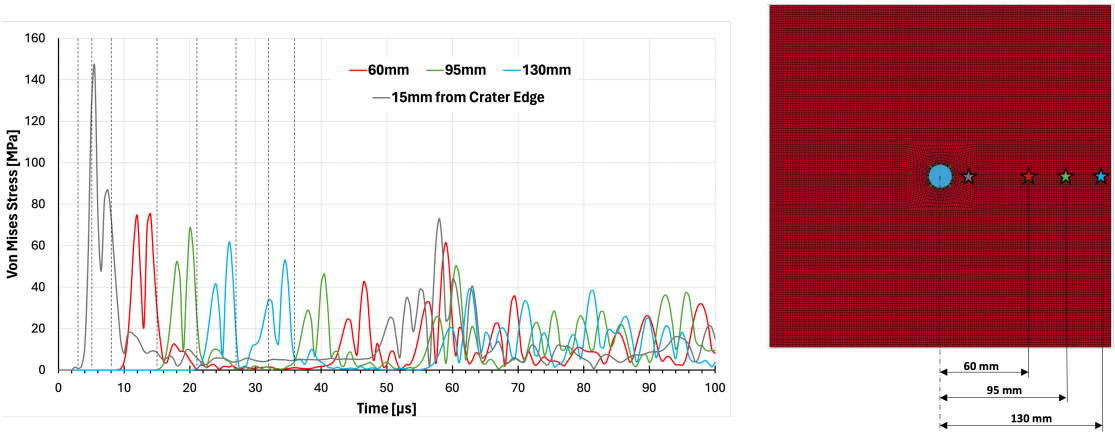

Figure 4.20: Comparison of von Mises stresses at increasing distances from the centre on the first plate.

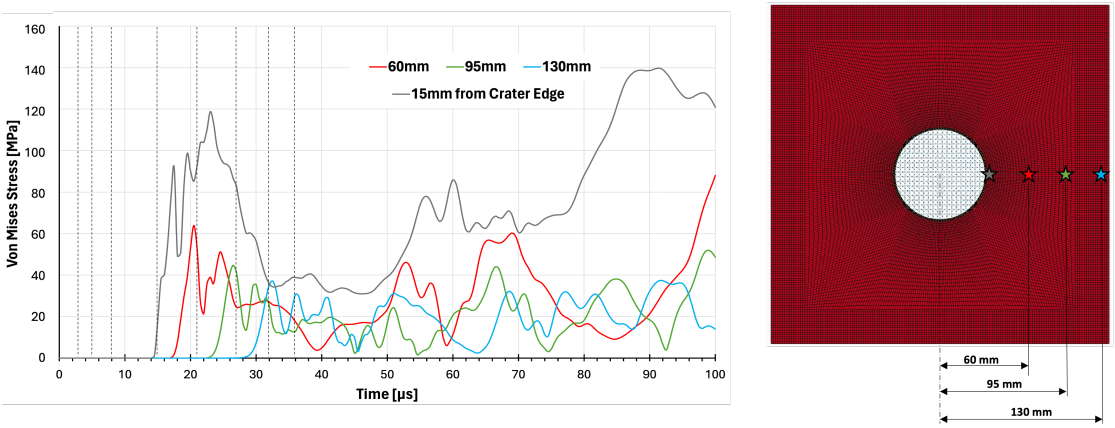

Figure 4.21: Comparison of Von Mises stresses at increasing distances from the centre on the second plate.

Analogous to the stress wave internal reflection analysis presented in Section 3.5, a similar behavior is observed when examining the Whipple shield. For both bumper and second plate, the curves follow a consistent pattern, but experience a temporal shift proportional to the distance between data points and a gradual attenuation of signal amplitude as the observation point moves away from the impact area. Interpreting these graphs can be challenging, especially for the bumper, due to the impact of boundary conditions. Such boundary conditions, by reflecting the stress waves, reverse their temporal order in the subsequent stress wave sequence.

The stress data collected from points adjacent to the crater in the first and second plate are significant. By analyzing these curves, it is possible to highlight the different types of phenomena that hit the two plates during HVI. In the first plate, the stress profile is consistent with an impulsive shock-type excitation, characterized by a sudden high-amplitude spike. In the second plate, the signal still exhibits a larger amplitude compared to the signal observed at other distances, but it seems to be caused by an excitation that is prolonged in time. In either case, the stress waves travel with equal velocity through the surrounding structure. To assess the speed of wave propagation, the time required for a stress wave peak to reach a subsequent data sampling point was measured and the distance between the two sites determined. The results indicated a propagation velocity of 5.83 mm/µs, which is consistent with values documented in the published literature on the topic [26, 11].

In the final comparative analysis aimed at assessing the structural behavior of the first plate in contrast to the second plate, stress signals gathered at various distances along the x-axis are juxtaposed in Fig. 4.22 in three different plots. Each plot presents stress signals from equidistant points relative to both plates. Maintaining continuity with the previous analysis, the red curves represent points located 60 mm from the center. Similarly, the green and blue curves correspond to points positioned at 95 mm and 130 mm from the center, respectively. The solid line pertains to the bumper, while the dashed line refers to the second plate.

Comparing stress patterns can be challenging. However, it is crucial to highlight that peak stress levels are significantly higher in the first plate, and stress attenuation over distance occurs at a slower rate compared to the second plate. This comparative analysis is further elucidated in the Table 4.6. In the first plate, the highest peak experiences a gradual reduction of 7.94% when comparing the maximum value recorded at a distance of 60 mm from the center with that recorded at 95 mm. Conversely, in the second plate, the highest peak undergoes a reduction of approximately 30%. Similarly, transitioning from 95 mm to 130 mm, a reduction of 9.5% is observed in the first plate, while in the second plate, a reduction of approximately 20% is evident.

	Max VM stress at 60 mm	**Max VM stress at 95 mm**	**Max VM stress at 130 mm**
1^{st} plate	74.3 MPa	68.4 MPa	61.9 MPa
% reduction	/	-7.94 %	-9.50 %
2^{nd} plate	63.9 MPa	44.7 MPa	37.2 MPa
% reduction	/	-30.0 %	-20.2 %

Table 4.6: Von Mises Stress Max Peak in the plates and percent reduction over two consecutive sampling points.

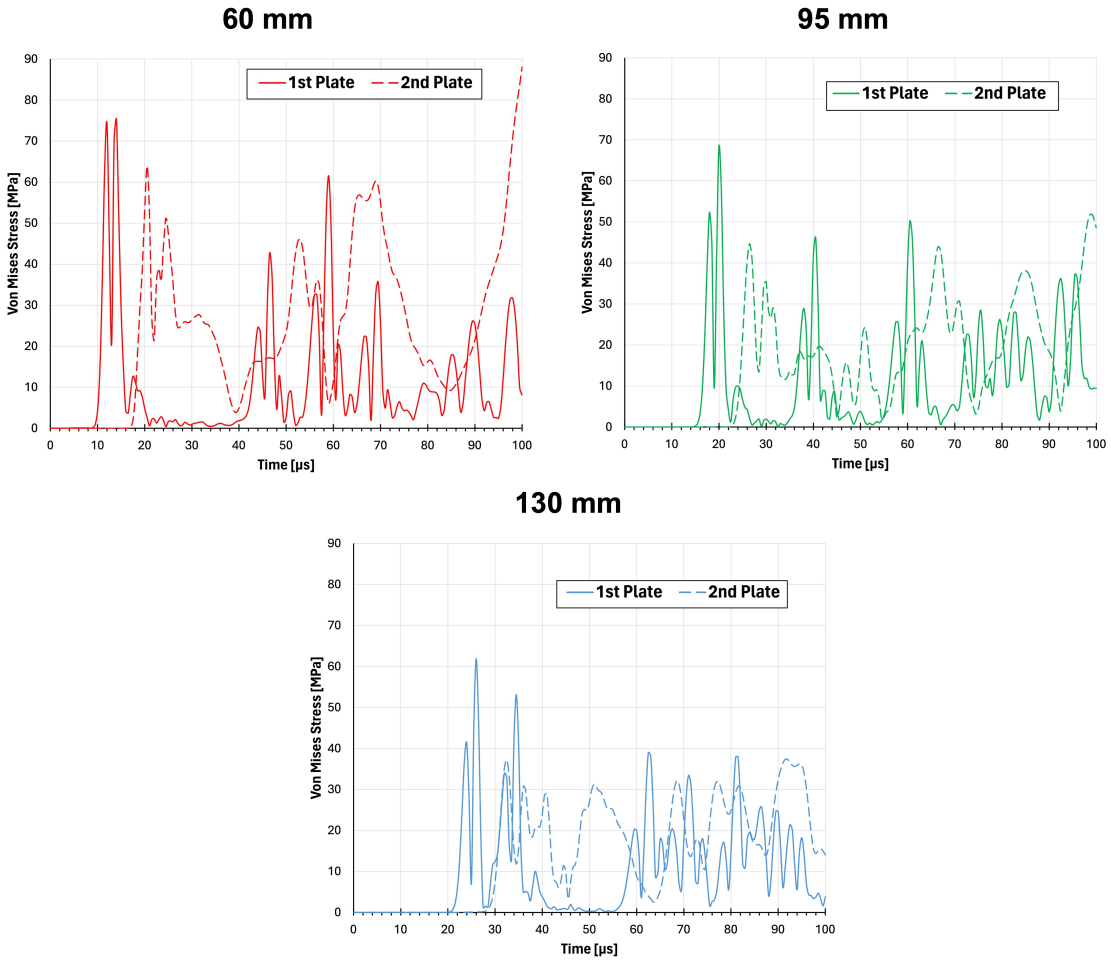

Figure 4.22: Von Mises Stress plot comparison in 1st and 2nd plate.

4.3.4. Induced Vibration

This section examines the phenomenon of vibrations induced by HVI and outlines the primary dynamic characteristics that emerge from such events. While a detailed analysis of the stresses caused by these impacts has been previously discussed, the focus now shifts to vibrations, which are equally significant in the design and structural safety assessment of space missions.

Understanding the field of vibrations induced by hyper-velocity impacts plays a crucial role, especially in designing and maintaining the structural integrity of next-generation satellites. This importance is heightened by the increasing sensitivity of space instruments, which require highly stable support platforms, and the dramatic increase in orbital debris.

In order to address this analysis, two distinct computational methodologies have been developed in the literature. The first methodology gathers information about the excitation signal through a simulation of the impact alone, and then allows the evaluation of the satellite's vibrational responses through finite element analysis using the previously obtained excitation signal [87]. In this approach, the initial impact is simulated to obtain the induced forces, which are subsequently applied to the FEM model of the satellite to analyze its global vibrational response. This methodology is advantageous because it separates the problem into two distinct phases, simplifying

the analysis and reducing the overall computational load. However, it may be less accurate in cases where the impactor shape and the satellite structure are complex.

The second method aims at modeling the entire system, including the complete satellite and the projectile, within a unified simulation procedure [32]. This approach uses the SPH technique to model the impact zone. At the same time, it uses finite element to represent the remaining part of the satellite. By integrating both techniques, using the methodology extensively studied in the previous sections, this approach does not distinguish between the study of the local effect and the overall vibrational response of the system, ensuring higher accuracy. However, it also entails a significantly higher computational burden due to the complexity of the integrated model and the need to solve both regions simultaneously with different techniques [32].

In the current case, although the FEM model surrounding the impact point is limited to a simple flat plate, we will focus on the second approach, demonstrating its potential implementation for more detailed future studies. Again, the analysis refers to the test case described in Section 4.1, which uses data courtesy Airbus Defence and Space. However, as in the case of stress analysis, there is a lack of experimental data to validate the simulation and the collected vibrations.

An analysis of the vibration signals along the z-axis (parallel to the plate normal) on the first and second plates was performed to obtain a detailed description of the vibration field induced by a hyper-velocity impact. As shown in Fig. 4.23, four points were chosen on each plate, located at varying distances and in different directions from the impact site. Specific points were identified and sequentially numbered from 1 to 4 on both plates at distances of 60, 85, 110, and 130 mm from the impact site. The measurement points were arranged in a spiral configuration, which is a common practice for similar experimental tests [66]. This allows for later experimental validation of the collected data.

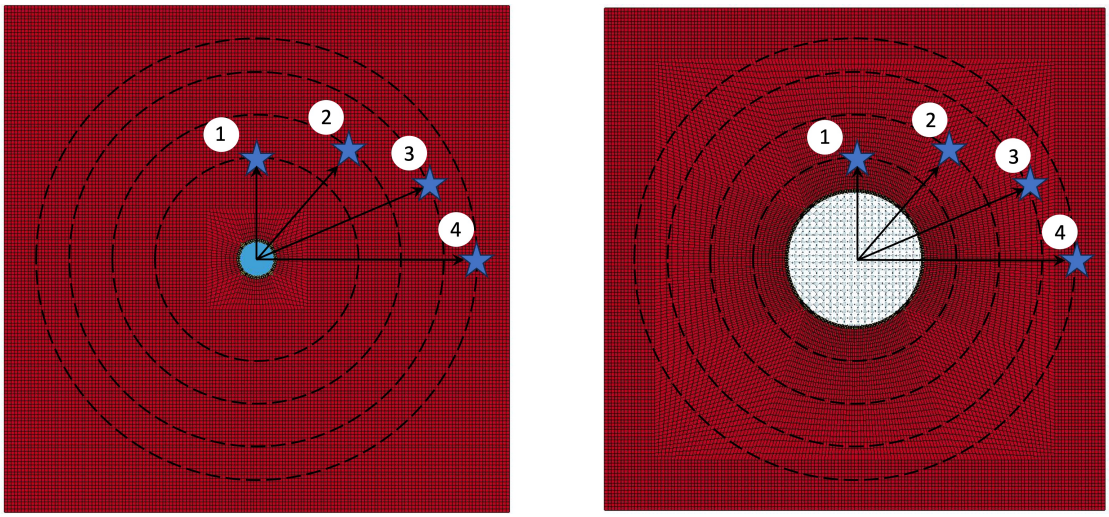

Figure 4.23: Analysed points in the Whipple shield HVI vibration study. Bumper on the left; second plate on the right.

In Fig. 4.24, the recorded signals are displayed through a matrix of graphs, allowing comparison of vibration levels both within the same plate and between different plates with respect to the same point.

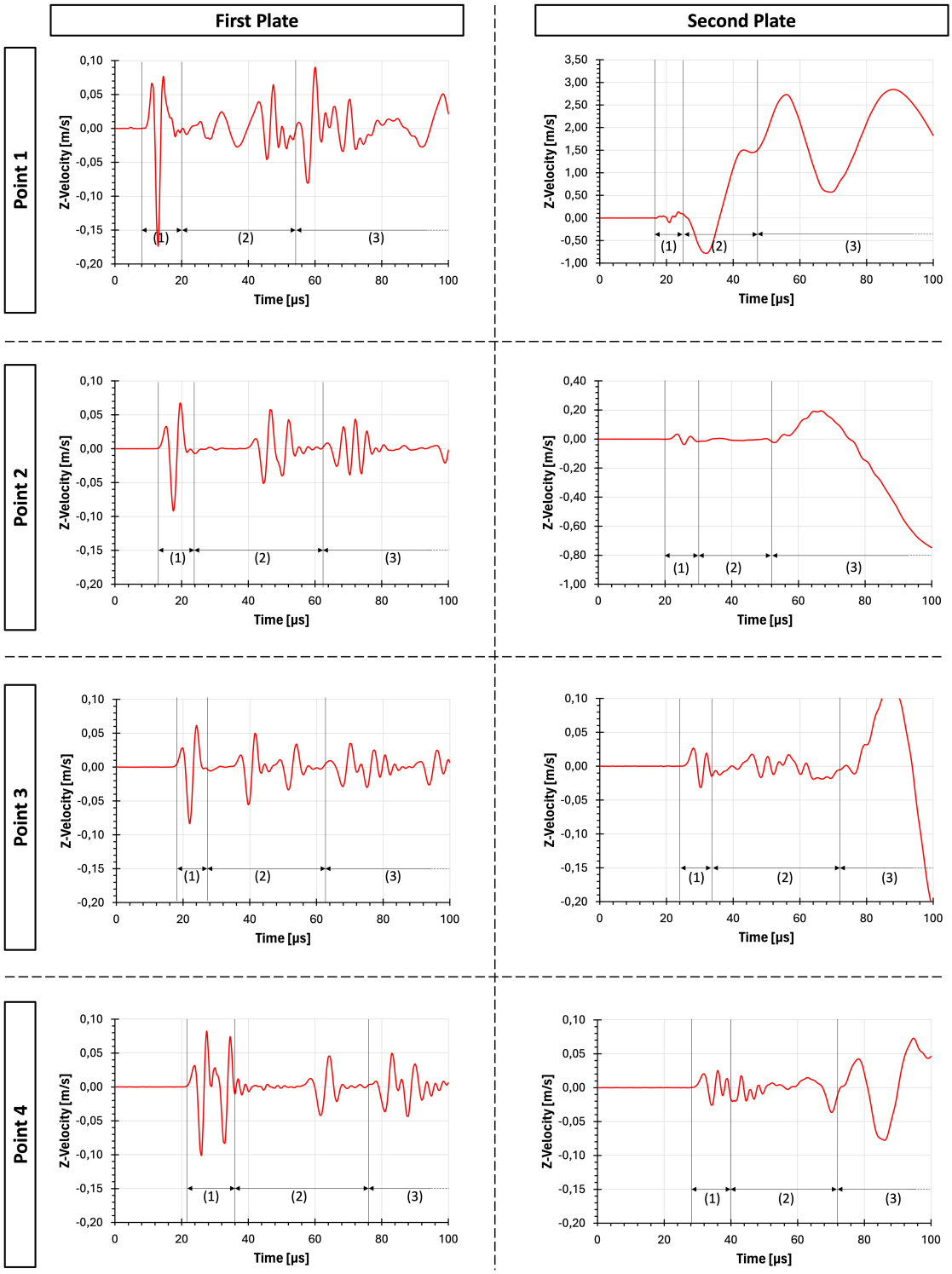

Figure 4.24: Vibration Signals retrieved at the analyzed point in the Whipple shield HVI study (z axis parallel to the plate normal and travelling speed for the satellite).

The analysis of the acquired signals reveals a significant difference in the clarity of the velocity data recorded for the first and second plates of the Whipple shield. Specifically, the data for the second plate, particularly at analysis points 1 and 2, are likely affected by their proximity to the perforation zone, where the impact caused large plastic deformation. This effect diminishes as the distance from the plate center increases, resulting in a vibration signal without anomalies

at analysis point 4. Notably, the signal amplitude scale remains constant across all analyzed points, except for points 1 and 2 of the second plate.

The analysis of the first plate shows comparable signal amplitudes at various distances, except for an initial peak at point 1. This trend aligns with findings from prior studies documented in Section 2.3 of the Literature Review chapter. Additionally, the analysis identifies three distinct waveform phases: longitudinal (1), shear (2), and flexural (3). Longitudinal waves, which are compressional waves, propagate faster through the medium and appear as an initial impulse in the vibration graph. Shear waves, which involve perpendicular motion to the direction of propagation, follow the longitudinal waves. Flexural waves, associated with the bending of the plate, have higher amplitudes, lower frequencies, and slower propagation velocities. However, in this particular case, the flexural waves on the bumper do not exhibit the largest amplitude. This phenomenon could be attributed to the sampling frequency used, the short duration of the simulation, or the boundary conditions affecting the plate's post-impact dynamics.

The second plate also exhibits initial high-frequency disturbances (longitudinal waves) followed by subsequent low-frequency oscillations (flexural waves). This phenomenon is particularly noticeable at analysis point 4 but is generalizable to other points closer to the impact site. In contrast to the first plate, as expected, the second plate's flexural waves exhibit larger amplitudes.

It is important to note that the data may be affected by the sampling frequency. Indeed, due to computational limitations, the sampling frequency was set to 2 MHz. The overall computation time depends on several factors, including the simulation termination time, time step, and the time required to calculate the solution at each step. Additionally, the duration of each computational cycle is influenced by the accuracy of the proposed model and the density of the mesh, particularly the SPH one. Increasing the number of SPH particles extends the computation time but enhances the accuracy of the solution until convergence. Therefore, conducting a trade-off study to determine the optimal combination of parameters is advisable. Despite executing the current simulation in parallel using 32 MPP processors due to the significant computational burden, the CPU time amounted to 100,140 seconds (27 hours and 49 minutes).

4.4. Summary

The chapter entitled "Simulation Methodology for Whipple Shield Hyper-Velocity Impacts" outlines a modeling approach for simulating hyper-velocity impacts within a Whipple shield configuration. The proposed model benefits from comparative studies conducted on the single-plate scenario. Specifically, it employs a circular SPH domain, an adaptive SPH/FEM contact algorithm, and a quasi-isotropic SPH initial lattice that has shown superior results in the single plate configuration.

The proposed model was validated using experimental data obtained in the frame of an hyper-velocity impact campaign test of Airbus Defence and Space under ESA contract, and are courtesy of Airbus Defence and Space. The comparison parameters were limited to the diameters of the craters in the first and second plates. These parameters were useful for validating the

simulation, but highlight the need for further experimental campaigns to obtain a more comprehensive understanding of the phenomenon.

The model accurately predicted the crater on the first plate with a relative error of approximately 4%. However, it was less accurate in predicting the crater on the second plate, with an estimated error of about 15%. Possible reasons for this discrepancy include the limited duration of the simulation, potential inaccuracies in material models, inaccuracies in input and output data such as impact velocity, or the inherent uncertainty and non-deterministic nature of HVI phenomena, or a combination of these factors.

An analysis of the simulation's energy revealed a loss of approximately 70% compared to the initial stage. The majority of this loss occurred during the second impact of the debris cloud with the second plate. Although concerning, this result is consistent with previous studies and should not compromise the validity of the current simulation. The software developers are currently investigating the issue.

A stress and vibration wave analysis induced by the impact of space debris against the Whipple shield was also performed. The study revealed both similarities and differences between the first and second plates. Regarding the stress, it reaches higher values and decays more slowly in the first plate than in the second plate. However, the velocity of propagation is comparable for both. While the impact effects in the bumper are local, in the second plate the absorbed energy contributes to the plastic deformation. This deformation extends over a relatively large area compared to the size of the projectile. In terms of vibration patterns, both plates have similar characteristics, but the amplitude of the flexural waves is significantly higher in the second plate. These waves have the potential to propagate through the satellite platform and cause deviations in the payload line of sight. Understanding these dynamics is essential for future modeling efforts to ensure satellite stability and reliability in the case of an impact.

Although not directly correlated with experimental data, the results seem to be consistent with those obtained from similar cases described in the literature. Although the FEM domain of the proposed model is limited to a flat plate with dimensions of 300 x 300 mm, the simulation carried out demonstrates the possibility of applying the proposed model to more complex geometries, ensuring a more accurate and detailed analysis of hyper-velocity impacts in space.

5

Conclusions and Recommendations

In the next chapter, the key findings are summarized and future research directions are suggested. Section 5.1 discusses the results of the hyper-velocity impact simulation analysis on single and double-plate systems, while Section 5.2 outlines proposed paths for further investigation based on the research outcomes.

5.1. Conclusions

The research for this thesis began with a comprehensive literature review to explore the multifaceted topics related to hyper-velocity impacts. Impacts were first examined by defining the speed range that characterises them as hyper-velocity and identifying a threshold value that is determined not only by the dynamic properties but also by the mechanical properties of the materials involved. Subsequently, constitutive models, failure criteria and equations of state commonly associated with materials subjected to hyper-velocity impacts were analysed, revealing extensive and satisfactory use in the literature of the Johnson-Cook model and the Mie-Grüneisen equation of state.

Having identified the limitations associated with experimental testing, including high cost, maximum achievable impact velocity and minimum projectile dimensions, the main numerical modelling techniques for HVIs, including the Finite Element Method (FEM) and Smoothed Particle Hydrodynamics (SPH), were then reviewed. The advantages and disadvantages of both techniques were highlighted, and the possibility of developing hybrid models that combine both methodologies was also considered. Such coupling could be achieved either by using hybrid SPH/FEM elements or by implementing an interface between a domain modelled by SPH and another modelled by finite elements. The literature review concludes with an analysis of numerical techniques for investigating vibrations and stresses induced by HVIs on satellites.

Subsequently, a study of the effects of a hyper-velocity impact on a single-plate system oriented perpendicular to the velocity direction of the projectile was carried out. A comparative analysis

was performed to identify the optimal settings for the contact methodology between FEM and SPH zones, the shape of the SPH domain, the implemented boundary conditions and the SPH particle lattice of the plate. The results were compared with experimental data for model validation. The study evaluated the mutual influence of these parameters not only on post-impact geometric parameters such as crater diameter, dimensions and debris cloud propagation velocity, but also on effects related to the homogeneity of the stress field induced by HVI. It was found that a configuration without symmetry planes, with a circular SPH domain and an initial spatial arrangement of particles in a quasi-isotropic lattice configuration, connected to the surrounding FEM zone by hybrid elements, yields the best results both in terms of post-impact geometric parameters (exhibiting the lowest absolute average error of 2.81%), and in terms of uniformity of stress propagation in the area surrounding the impact.

A comprehensive analysis of a hyper-velocity impact on a Whipple shield was then carried out, using data courtesy of Airbus Defence and Space for validation. The implemented model, based on the results of previous comparative analyses, achieved a high degree of accuracy, particularly with regard to the crater formed on the first impact plate. The study showed the effectiveness of the Whipple shield in fragmenting and slowing down the projectile, thus dissipating its kinetic energy. Despite limited frequency resolution, a detailed analysis of the propagation of stress and vibration waves induced by the HVI was carried out.

The study demonstrated that the higher stress levels are primarily transmitted through the bumper to the rest of the satellite structure. In contrast, the second plate is more involved in the transmission of higher amplitude vibrations. These higher amplitude vibrations, which occur at low frequencies, are considered to be the primary cause of the loss of stability in the impacted satellite. This distinction highlights the different roles each plate plays in the overall effectiveness of the Whipple shield. The bumper is primarily responsible for stress transfer, while the second plate is more involved in the transmission of vibratory effects. This observation can provide valuable insights for the design phase of satellites, potentially leading to improved structural integrity and resilience against hypervelocity impacts.

Although the stress and vibration wave propagation studies lack experimental correlation and validation, significant analogies with other studies published in the literature were observed. Despite the limitation of the size of the FEM domain surrounding the SPH impact zone, it is possible to extend the developed methodology to more complex geometries, allowing the assessment of the effects of a hyper-velocity impact on a real satellite and the development of vulnerability maps for the analysed space platform.

5.2. Recommendations

The thesis results indicate significant opportunities for developing a coupled SPH/FEM modeling methodology to analyze hyper-velocity impacts on satellites and space structures. However, challenges and areas of development still accompany the path towards a more comprehensive application of this methodology.

One of the main barriers identified is the need for experimental data to further validate the numer-

ical approach. Therefore, experimental test campaigns are recommended, which, in addition to the geometry during and after the impact of the plates and the debris cloud, should include the collection of data on induced stresses and vibrations using high-frequency acquisition sensors such as accelerometers, laser Doppler vibrometers or high-speed cameras for the implementation of digital image correlation techniques.

Another important area of development is monitoring the software's capabilities to ensure the conservation of total energy during calculation steps. This is crucial to ensure the validity of the results and requires careful analysis and control.

Furthermore, it is of paramount importance to develop a mathematical approach to investigate the effect of the SPH particle lattice on stress wave propagation. It is of significant consequence to understand how the distribution of SPH particles in simulations affects stress propagation through the modeled material. A mathematical approach could facilitate the implementation of a more efficient method of particle distribution, thereby ensuring more uniform and realistic stress propagation. This will allow for a deeper understanding of the mechanisms underlying the developed numerical models.

Finally, it is necessary to investigate the methodology's applicability to materials with more complex mechanical characteristics, such as composite materials, ceramics, fabrics, and metal foams, used in space subsystems like solar panels or deployable and inflatable structures. This study would improve our understanding of real structures' behavior and make it possible to adapt the methodology accordingly, further enhancing its applicability and effectiveness in the space context.

In summary, implementing these recommendations would refine the coupled SPH/FEM modeling methodology and advance the understanding and analysis of hyper-velocity impacts on satellites and space structures.

References

[1] Abraham, Broughton, Bernstein, and Kaxiras. “Spanning the length scales in dynamic simulation”. In: *Computers in Physics* 12.6 (1998), pp. 538–546.

[2] Addessio, Baumgardner, Dukowicz, Johnson, Kashiwa, Rauenzahn, and Zemach. *”CAVEAT: A computer code for fluid dynamics problems with large distortion and internal slip”*. Tech. rep. Los Alamos National Lab. (LANL), Los Alamos, NM (United States), 1992.

[3] Aglietti. “Current Challenges and Opportunities for Space Technologies”. In: *Frontiers in Space Technologies* 1 (2020).

[4] Akram, Jaffery, Khan, Fahad, Mubashar, and Ali. “Numerical and experimental investigation of Johnson–Cook material models for aluminum (Al 6061-T6) alloy using orthogonal machining approach”. In: *Advances in Mechanical Engineering* 10.9 (2018), p. 1687814018797794.

[5] Aktay and Johnson. “FEM/SPH coupling technique for high velocity impact simulations”. In: *Advances in Meshfree Techniques*. Springer. 2007, pp. 147–167.

[6] Attaway, Heinstein, and Swegle. “Coupling of smooth particle hydrodynamics with the finite element method”. In: *Nuclear engineering and design* 150.2-3 (1994), pp. 199–205.

[7] Belytschko, Liu, Moran, and Elkhodary. *Nonlinear finite elements for continua and structures*. John wiley & sons, 2014.

[8] Belytschko, Organ, and Krongauz. “A coupled finite element-element-free Galerkin method”. In: *Computational Mechanics* 17.3 (1995), pp. 186–195.

[9] Belytschko and Xiao. “A bridging domain method for coupling continua with molecular dynamics”. In: *Computer methods in applied mechanics and engineering* 193.17-20 (2004), pp. 1645–1669.

[10] Buslov, Komarov, Selivanov, Titov, Tovarnova, and Feldstein. “Protection of inflatable modules of orbital stations against impacts of particles of space debris”. In: *Acta Astronautica* 163 (2019), pp. 54–61.

[11] Buyuk, Kan, and Loikkanen. “Explicit finite-element analysis of 2024-T3/T351 aluminum material under impact loading for airplane engine containment and fragment shielding”. In: *Journal of Aerospace Engineering* 22.3 (2009), pp. 287–295.

[12] Chakraborty and Shaw. “A pseudo-spring based fracture model for SPH simulation of impact dynamics”. In: *International Journal of Impact Engineering* 58 (2013), pp. 84–95.

[13] Chen, Beraun, and Jih. “An improvement for tensile instability in smoothed particle hydrodynamics”. In: *Computational Mechanics* 23.4 (1999), pp. 279–287.

[14] Chen, Hillman, and Chi. “Meshfree methods: progress made after 20 years”. In: *Journal of Engineering Mechanics* 143.4 (2017), p. 04017001.

[15] Cherniaev and Telichev. “Weight-efficiency of conventional shielding systems in protecting unmanned spacecraft from orbital debris”. In: *Journal of Spacecraft and Rockets* 54.1 (2017), pp. 75–89.

[16] Chhabildas, Davison, and Horie. *High-pressure shock compression of solids VIII: The science and technology of high-velocity impact*. Springer Science & Business Media, 2004.

[17] Clough, Lieblein, and McMillan. *Crater characteristics of 11 metal alloys under hypervelocity impact including effects of projectile density and target temperature*. National Aeronautics and Space Administration, 1969.

[18] *Columbus Meteoroid and Debris Protection Shield (MOPS), Phase II Study Extension, Work Package 1440 "Impact Test Performance", ESTEC Contract 8732190, Final Report.* Tech. rep.

[19] Cowper and Symonds. "Strain-hardening and strain-rate effects in the impact loading of cantilever beams". In: (1957).

[20] Dai, Wang, Huang, Song, and Iio. "SPH-based numerical modeling for the post-failure behavior of the landslides triggered by the 2016 Kumamoto earthquake". In: *Geoenvironmental Disasters* 3.1 (2016), pp. 1–14.

[21] Das and Holm. "On the improvement of computational efficiency of smoothed particle hydrodynamics to simulate flexural failure of ice". In: *Journal of Ocean Engineering and Marine Energy* 4 (2018), pp. 153–169.

[22] Dilts. "Moving-least-squares-particle hydrodynamics—I. Consistency and stability". In: *International Journal for Numerical Methods in Engineering* 44.8 (1999), pp. 1115–1155.

[23] "Energy Conservation as a Measure of Simulation Accuracy". In: *bioRxiv* (2016). DOI: 10.1101/083055. URL: https://www.biorxiv.org/content/early/2016/10/24/083055.

[24] European Space Agency ESA. *"Annual Space Environment REPORT", (code: GEN-DB-LOG-00288-OPS-SD), 2023*. URL: https://www.sdo.esoc.esa.int/environment_report/Space_Environment_Report_latest.pdf (visited on 10/16/2023).

[25] European Space Agency ESA. *"ESA commissions world's first space debris removal", 2019*. URL: https://www.esa.int/Newsroom/Press_Releases/ESA_commissions_world_s_first_space_debris_removal (visited on 10/16/2023).

[26] Mohammadi Esfarjani. "Evaluation of effect changing temperature on lamb-wave based structural health monitoring". In: *Journal of Mechanical and Energy Engineering* 3.4 (2019), pp. 329–336.

[27] Evans, Harvey Harlow, and Bromberg. "The particle-in-cell method for hydrodynamic calculations". In: (1957).

[28] Fahrenthold and Horban. "An improved hybrid particle-element method for hypervelocity impact simulation". In: *International Journal of Impact Engineering* 26.1-10 (2001), pp. 169–178.

[29] Flegel, Wiedemann, Stabroth, Alwes, Bendisch, and Vörsmann. "Satellite failure risk due to hypervelocity impacts". In: *Proceedings, 19th International Astronautical Congress*. 2008.

[30] Francesconi, Giacomuzzo, Olivieri, Sarego, Duzzi, Feltrin, Valmorbida, Bunte, Deshmukh, and Farahvashi. "CST: A new semi-empirical tool for simulating spacecraft collisions in orbit". In: *Acta Astronautica* 160 (2019), pp. 195–205.

[31] Gehring. "Engineering considerations in hypervelocity impact". In: *High-Velocity Impact Phenomena* 463 (1970), p. 514.

[32] Giacomuzzo, Pavarin, Francesconi, Lambert, and Angrilli. "SPH evaluation of out-of-plane peak force transmitted during a hypervelocity impact". In: *International Journal of Impact Engineering* 35.12 (2008), pp. 1534–1540.

[33] Gingold and Monaghan. "Smoothed particle hydrodynamics: theory and application to non-spherical stars". In: *Monthly notices of the royal astronomical society* 181.3 (1977), pp. 375–389.

[34] Gray, Monaghan, and Swift. "SPH elastic dynamics". In: *Computer methods in applied mechanics and engineering* 190.49-50 (2001), pp. 6641–6662.

[35] Grüneisen. "Theorie des festen Zustandes einatomiger Elemente". In: *Annalen der Physik* 344.12 (1912), pp. 257–306.

[36] Hallquist. *LS-DYNA Theory Manual*. Livermore Software Technology Corporation (LSTC), Livermore. 2006.

[37] Han, Wagner, and Liu. “Convergence analysis of a hierarchical enrichment of Dirichlet boundary conditions in a mesh-free method”. In: *International Journal for Numerical Methods in Engineering* 53.6 (2002), pp. 1323–1336.

[38] Harazim. *Master Thesis: Hypervelocity Impact Simulation using Smoothed-Particle Hydrodynamics*. Delft University of Technology, 2023.

[39] He, Chen, and Chen. “Finite element-smoothed particle hydrodynamics adaptive method in simulating debris cloud”. In: *Acta Astronautica* 175 (2020), pp. 99–117.

[40] Hirt, Amsden, and Cook. “An arbitrary Lagrangian-Eulerian computing method for all flow speeds”. In: *Journal of computational physics* 14.3 (1974), pp. 227–253.

[41] Horner. “A comparison of ballistic limit with adaptive-mesh Eulerian hydrocode predictions of one-and two-plate aluminum shielding protection against millimeter-sized Fe–Ni space debris”. In: *International Journal of Impact Engineering* 35.12 (2008), pp. 1602–1605.

[42] Hrennikoff. “Solution of problems of elasticity by the framework method”. In: (1941).

[43] Huebner, Dewhirst, Smith, and Byrom. *The finite element method for engineers*. John Wiley & Sons, 2001.

[44] Huerta and Fernández-Méndez. “Enrichment and coupling of the finite element and meshless methods”. In: *International Journal for Numerical Methods in Engineering* 48.11 (2000), pp. 1615–1636.

[45] Inutsuka. “Reformulation of smoothed particle hydrodynamics with Riemann solver”. In: *Journal of Computational Physics* 179.1 (2002), pp. 238–267.

[46] Johnson. “A Constitutive Model and Date for Metals Subject to Large Strains, High Strain Rate and High Temperatures”. In: *Proceedings: 7th Int. Symp. on Ballistics, The Hague*. 1983.

[47] Johnson. *EPIC-3, a computer program for elastic-plastic impact calculations in 3 dimensions*. Tech. rep. Contract Report, Hopkins, MN, 1977.

[48] Johnson. “Impact strength of materials”. In: (1972).

[49] Johnson. “Linking of Lagrangian particle methods to standard finite element methods for high velocity impact computations”. In: *Nuclear Engineering and Design* 150.2-3 (1994), pp. 265–274.

[50] Johnson. “Materials Characterization for computations involving severe dynamic loading”. In: *Proceedings: Army Symp. Of Solid Mechanics*. Cape Cod, Mass. 1980, pp. 62–67.

[51] Johnson, Beissel, and Gerlach. “A combined particle-element method for high-velocity impact computations”. In: *Procedia Engineering* 58 (2013), pp. 269–278.

[52] Johnson, Beissel, and Gerlach. “Another approach to a hybrid particle-finite element algorithm for high-velocity impact”. In: *International journal of impact engineering* 38.5 (2011), pp. 397–405.

[53] Johnson and Anderson Jr. “History and application of hydrocodes in hypervelocity impact”. In: *International Journal of Impact Engineering* 5.1-4 (1987), pp. 423–439.

[54] Johnson, Krisko, Liou, and Anz-Meador. “NASA’s new breakup model of EVOLVE 4.0”. In: *Advances in Space Research* 28.9 (2001), pp. 1377–1384.

[55] Jonas and Zukas. “Mechanics of penetration: analysis and experiment”. In: *International Journal of Engineering Science* 16.11 (1978), pp. 879–903.

[56] El Kadmiri, Belaasilia, Timesli, and Kadiri. “A hybrid algorithm using the FEM-MESHLESS method to solve nonlinear structural problems”. In: *Engineering Analysis with Boundary Elements* 140 (2022), pp. 531–543.

[57] Kessler and Cour-Palais. “Collision frequency of artificial satellites: The creation of a debris belt”. In: *Journal of Geophysical Research: Space Physics* 83.A6 (1978), pp. 2637–2646.

[58] Lanz, Odermatt, and Weihrauch. “Kinetic energy projectiles: Development history, state of the art, trends”. In: *Proceedings: 19th International Symposium of Ballistics, Interlaken, Switzerland*. 2001, pp. 7–11.

[59] Legaud, Le Garrec, Van Dorsselaer, and Lapoujadet. “Improvement of satellites shielding under high velocity impact using advanced SPH method”. In: *Proc., 12th European LS-DYNA Conf. Stuttgart, Germany: DYNAmore GmbH*. 2019.

[60] Li and Liu. *Meshfree particle methods*. Springer Science & Business Media, 2007.

[61] Li, Perotti, Adams, Mihaly, Rosakis, Stalzer, and Ortiz. “Large scale optimal transportation meshfree (OTM) simulations of hypervelocity impact”. In: *Procedia Engineering* 58 (2013), pp. 320–327.

[62] Limido, Trabia, Roy, O’Toole, Jennings, Mindle, Pena, Daykin, Hixson, and Matthes. “Modeling of Hypervelocity Impact Experiments Using Gamma-SPH Technique”. In: *Pressure Vessels and Piping Conference*. Vol. 57977. American Society of Mechanical Engineers. 2017.

[63] Liu and Chen. “Wavelet and multiple scale reproducing kernel methods”. In: *International Journal for Numerical Methods in Fluids* 21.10 (1995), pp. 901–931.

[64] Liu, Li, and Park. “Eighty years of the finite element method: Birth, evolution, and future”. In: *Archives of Computational Methods in Engineering* 29.6 (2022), pp. 4431–4453.

[65] Liu and Liu. “Smoothed particle hydrodynamics (SPH): an overview and recent developments”. In: *Archives of computational methods in engineering* 17 (2010), pp. 25–76.

[66] Liu, Wang, Zhang, Long, Cui, and Su. “Hypervelocity impact induced shock acoustic emission waves for quantitative damage evaluation using in situ miniaturized piezoelectric sensor network”. In: *Chinese Journal of Aeronautics* 32.5 (2019), pp. 1059–1070. ISSN: 1000-9361.

[67] Logan. *A first course in the finite element method*. Vol. 4. Thomson, 2002.

[68] Lucy. “A numerical approach to the testing of the fission hypothesis”. In: *Astronomical Journal, vol. 82, Dec. 1977, p. 1013-1024.* 82 (1977), pp. 1013–1024.

[69] Lyon. *Sesame: the Los Alamos National Laboratory equation of state database*. Tech. rep. Los Alamos National Lab. (LANL), Los Alamos, NM (United States), 1978.

[70] Ma, Zhang, and Qiu. “Comparison study of MPM and SPH in modeling hypervelocity impact problems”. In: *International journal of impact engineering* 36.2 (2009), pp. 272–282.

[71] McKnight, Maher, and Nagl. “Refined algorithms for structural breakup due to hypervelocity impact”. In: *International journal of impact engineering* 17.4-6 (1995), pp. 547–558.

[72] Meng, Taddei, Lebaal, and Roth. “Advances in ballistic penetrating impact simulations on thin structures using Smooth Particles Hydrodynamics: A state of the art”. In: *Thin-Walled Structures* 159 (2021).

[73] Molteni and Colagrossi. “A simple procedure to improve the pressure evaluation in hydrodynamic context using the SPH”. In: *Computer Physics Communications* 180.6 (2009), pp. 861–872.

[74] Monaghan. “SPH without a tensile instability”. In: *Journal of computational physics* 159.2 (2000), pp. 290–311.

[75] Monaghan. “Theory and applications of smoothed particle hydrodynamics”. In: *Frontiers of Numerical Analysis*. Springer, 2005, pp. 143–194.

[76] United Nations. *”Guidelines for the long-term sustainability of outer space activities”, 2019*. URL: `https://www.unoosa.org/res/oosadoc/data/documents/2019/aac_105c_1l/aac_105c_1l_366_0_html/V1805022.pdf` (visited on 10/16/2023).

[77] Opik. “Researches on the Physical Theory of Meteor Phenomena. I. Theory of the Formation of Meteor Craters.” In: *Publications of the Tartu Astrofizica Observatory* 28 (1936), pp. 1–12.

[78] Park, Kim, Shin, and Kim. “A Comparative Study of Hypervelocity Impact Characteristics in Aluminum Whipple Shielding Through 3D Measurement and Numerical Analysis”. In: *International Journal of Aeronautical and Space Sciences* 22 (2021), pp. 1356–1364.

[79] Pavarin, Francesconi, Destefanis, Lambert, Bettella, Debei, De Cecco, Faraud, Giacomuzzo, and Marucchi-Chierro. “Acceleration fields induced by hypervelocity impacts on spacecraft structures”. In: *International journal of impact engineering* 33.1-12 (2006), pp. 580–591.

[80] Perrot. *A to Z of Thermodynamics*. Oxford University Press Oxford, UK, 1998.

[81] Plassard, Mespoulet, and Hereil. “Hypervelocity impact of aluminium sphere against aluminium plate: experiment and LS-DYNA correlation”. In: *Proceedings of the 8th European LS-DYNA users conference*. 2011, pp. 1–11.

[82] Rabczuk, Belytschko, and Xiao. “Stable particle methods based on Lagrangian kernels”. In: *Computer methods in applied mechanics and engineering* 193.12-14 (2004), pp. 1035–1063.

[83] Rabczuk, Xiao, and Sauer. “Coupling of mesh-free methods with finite elements: basic concepts and test results”. In: *Communications in numerical methods in engineering* 22.10 (2006), pp. 1031–1065.

[84] Reveles. “Development of a total Lagrangian SPH code for the simulation of solids under dynamioc loading”. In: (2007).

[85] Ruoff. “Linear shock-velocity-particle-velocity relationship”. In: *Journal of Applied Physics* 38.13 (1967), pp. 4976–4980.

[86] Ryan. “Numerical simulation in micrometeoroid and orbital debris risk assessment”. In: *Predictive Modeling of Dynamic Processes: A Tribute to Professor Klaus Thoma*. Springer, 2009, pp. 417–446.

[87] Ryan, Schäfer, Guyot, Hiermaier, and Lambert. “Characterizing the transient response of CFRP/Al HC spacecraft structures induced by space debris impact at hypervelocity”. In: *International Journal of Impact Engineering* 35.12 (2008), pp. 1756–1763.

[88] Sibeaud, Héreil, and Albouys. “Hypervelocity impact on spaced target structures: Experimental and ouranos simulation achievements”. In: *International journal of impact engineering* 29.1-10 (2003), pp. 647–658.

[89] Signetti and Heine. “Transition regime between high-velocity and hypervelocity impact in metals–a review of the relevant phenomena for material modeling in ballistic impact studies”. In: *International Journal of Impact Engineering* 167 (2022), p. 104213.

[90] Silnikov, Guk, Nechunaev, and Smirnov. “Numerical simulation of hypervelocity impact problem for spacecraft shielding elements”. In: *Acta Astronautica* 150 (2018), pp. 56–62.

[91] Spear, Palazotto, and Kemnitz. “Modeling and simulation techniques used in high strain rate projectile impact”. In: *Mathematics* 9.3 (2021), p. 274.

[92] Steinberg, Cochran, and Guinan. “A constitutive model for metals applicable at high-strain rate”. In: *Journal of applied physics* 51.3 (1980), pp. 1498–1504.

[93] Sugiura and Inutsuka. “An extension of Godunov SPH: application to negative pressure media”. In: *Journal of Computational Physics* 308 (2016), pp. 171–197.

[94] Swaddiwudhipong, Islam, and Liu. “High velocity penetration/perforation using coupled smooth particle hydrodynamics-finite element method”. In: *International Journal of Protective Structures* 1.4 (2010), pp. 489–506.

[95] Thompson. “CSQ–A Two Dimensional Hydrodynamic Program with Energy Flow and Material Strength”. In: *Sandia Laboratories, N. SAND74-0122* (1975).

[96] Tillotson. *Metallic equations of state for hypervelocity impact*. General Dynamics Falls Church, VA, 1962.

[97] Vergniaud, Guyot, Lambert, Schafer, Ryan, Hiermaier, and Taylor. “Structural vibrations induced by HVI–application to the GAIA spacecraft”. In: *International journal of impact engineering* 35.12 (2008), pp. 1836–1843.

[98] Wagner and Liu. “Coupling of atomistic and continuum simulations using a bridging scale decomposition”. In: *Journal of Computational Physics* 190.1 (2003), pp. 249–274.

[99] Watson, Gulde, Kortmann, Higashide, Schaefer, and Hiermaier. “Optical fragment tracking in hypervelocity impact experiments”. In: *Acta Astronautica* 155 (2019), pp. 111–117.

[100] Wen, Chen, and Lu. “Research and development on hypervelocity impact protection using Whipple shield: An overview”. In: *Defence Technology* 17.6 (2021), pp. 1864–1886.

[101] Whipple. “Meteorites and space travel.” In: *The Astronomical Journal* 52 (1947), p. 131.

[102] Wicklein, Ryan, White, and Clegg. “Hypervelocity impact on CFRP: Testing, material modelling, and numerical simulation”. In: *International Journal of Impact Engineering* 35.12 (2008), pp. 1861–1869.

[103] Williamsen, Pechkis, Balakrishnan, and Ouellette. “Improving Orbital Debris Environment Predictions Through Examining Satellite Movement Data”. In: *Journal of Spacecraft and Rockets* 58.3 (2021), pp. 779–785.

[104] Xu and Belytschko. “Conservation properties of the bridging domain method for coupled molecular/continuum dynamics”. In: *International Journal for Numerical Methods in Engineering* 76.3 (2008), pp. 278–294.

[105] Jingxiao Xu and Jason Wang. “Interaction methods for the SPH parts (multiphase flows, solid bodies) in LS-DYNA”. In: *Proceedings of the 13th International LS-DYNA Users Conference, Detroit, MI, USA*. 2014, pp. 8–10.

[106] Yang, Ye, Ren, and Tian. “Antipenetration Performance of Multilayer Protective Structure by the Coupled SPH-FEM Numerical Method”. In: *Shock and Vibration* (2023).

[107] Zhang, Khare, Lu, and Belytschko. “A bridging domain and strain computation method for coupled atomistic–continuum modelling of solids”. In: *International Journal for Numerical Methods in Engineering* 70.8 (2007), pp. 913–933.

[108] Zhang, Lu, Yang, Zhang, Sun, and Liu. “Numerical Study on the Breaking Process of the Seafloor Massive Sulfide Based on the FEM-SPH Adaptive Coupling Algorithm”. In: *Journal of Marine Science and Engineering* 11.4 (2023), p. 698.

[109] Zhang, Wang, Silberschmidt, and Wang. “SPH-FEM simulation of shaped-charge jet penetration into double hull: A comparison study for steel and SPS”. In: *Composite Structures* 155 (2016), pp. 135–144.

[110] Zukas. *Introduction to hydrocodes*. Elsevier, 2004.

A

LS-DYNA keywords: Single-Plate HVI

In this appendix, additional supporting material relevant to the main text is provided for further reference. The screenshots below show the keyword configuration used in the simulations described in Chapter 3 using LS-DYNA Pre-Post V4.8.

Dimensional consistency is critical for correct simulation. The simulation uses the following dimensional set: [mm, kg, ms, KN, GPa, J, Kelvin].

Boundary Conditions

Figures A.1, A.2 and A.3 show the screenshots from LS-DYNA Pre-Post V4.8 concerning the keyword configuration used in the simulation discussed in Chapter 3 to implement the model boundary conditions. Regarding the symmetry planes, only the keyword for the plane with normal X is shown, while the one with normal Y can be easily implemented. The SPH symmetry plane should stand at half the interparticle distance (0.125 mm).

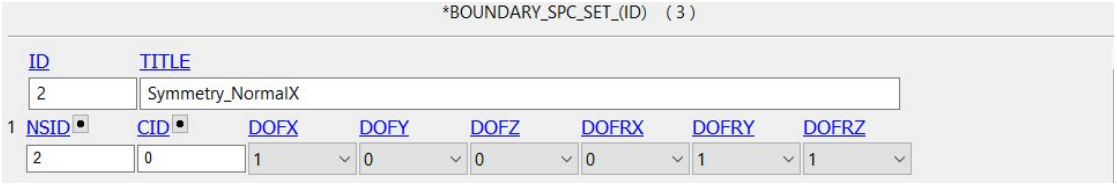

Figure A.1: LS-DYNA Pre-Post V4.8 screenshot of the keyword for the X-normal symmetry plane for solid elements (***BOUNDARY_SPC_SET**).

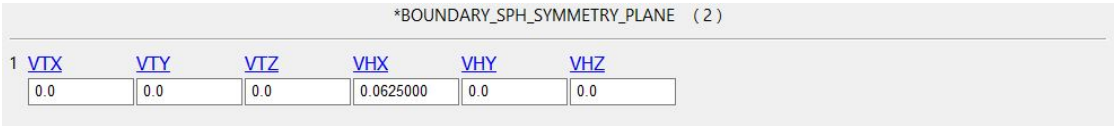

Figure A.2: LS-DYNA Pre-Post V4.8 screenshot of the keyword for the X-normal symmetry plane for SPH particles (***BOUNDARY_SPH_SYMMETRY_PLANE**).

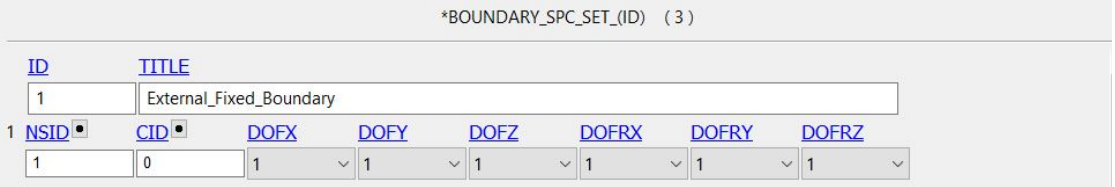

Figure A.3: LS-DYNA Pre-Post V4.8 screenshot of the keyword for the external clamped edges (***BOUNDARY_SPC_SET**).

Control setting

Figures from A.4 to A.8 show the screenshots from LS-DYNA Pre-Post V4.8 concerning the keyword configuration used in the simulation discussed in Chapter 3 to implement the model control setting.

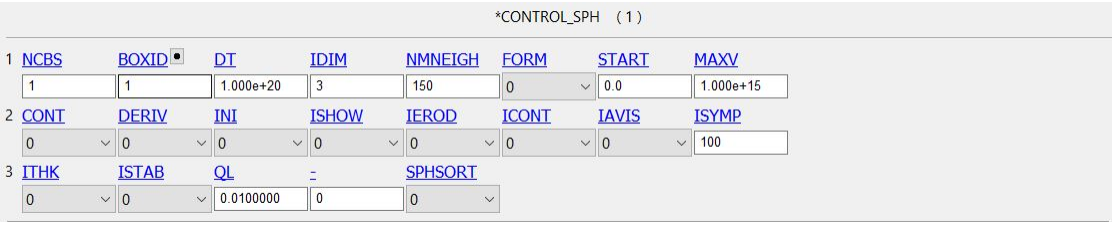

Figure A.4: LS-DYNA Pre-Post V4.8 screenshot of the keyword for the control setting for SPH (***CONTROL_SPH**).

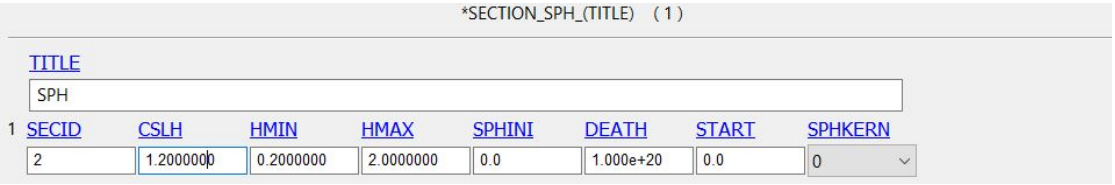

Figure A.5: LS-DYNA Pre-Post V4.8 screenshot of the keyword for the control setting for SPH (***SECTION_SPH**).

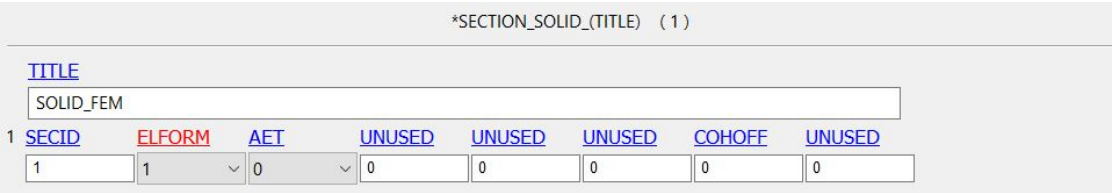

Figure A.6: LS-DYNA Pre-Post V4.8 screenshot of the keyword for the control setting for FEM (***SECTION_SOLID**).

Figure A.7: LS-DYNA Pre-Post V4.8 screenshot of the keyword for the hourglass control setting for FEM (***CONTROL_HOURGLASS**).

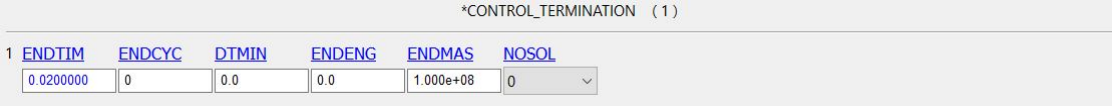

Figure A.8: LS-DYNA Pre-Post V4.8 screenshot of the keyword for the termination time control (***CONTROL_TERMINATION**).

Initial setting

Figure A.9 displays the LS-DYNA Pre-Post V4.8 screenshot concerning the keyword configuration used in the simulation discussed in Chapter 3 to set the model initial setting.

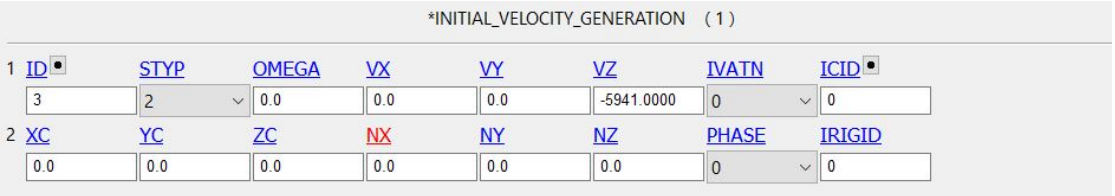

Figure A.9: LS-DYNA Pre-Post V4.8 screenshot of the keyword for the projectile initial velocity (***INITIAL_VELOCITY_GENERATION**).

Material Properties

Figures A.10 and A.11 show the LS-DYNA Pre-Post V4.8 screenshots related to the configuration of the keywords used in the simulation discussed in Chapter 3 to set the material model and its equation of state, respectively.

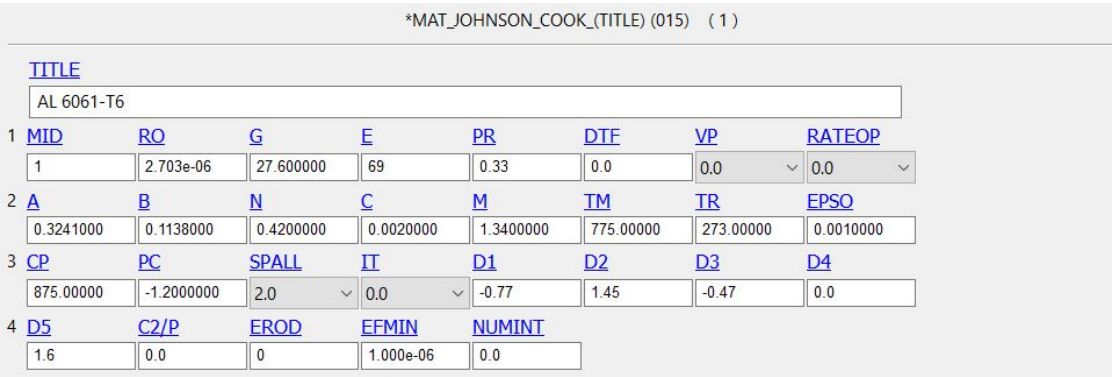

Figure A.10: LS-DYNA Pre-Post V4.8 screenshot of the keyword for the implemented material model (***MAT_JOHNSON_COOK**).

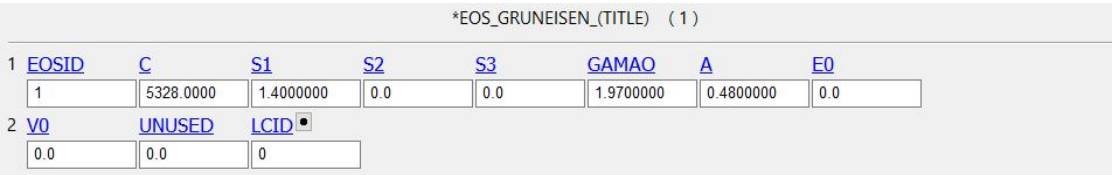

Figure A.11: LS-DYNA Pre-Post V4.8 screenshot of the keyword for the implemented material equation of state (***EOS_GRUNEISEN**).

Output Setting

Figures A.12 and A.13 show the LS-DYNA Pre-Post V4.8 screenshots related to the configuration of the keyword used in the simulation discussed in Chapter 3 to set the model output.

In the Fig. A.13, only the default time interval between outputs and the instruction for storing information are displayed. The output data to be selected depends on the purpose of the simulation. However, those generally selected and used for analyzing the results of similar simulations are: BNDOUT, ELOUT, GLSTAT, MATSUM, NCFORC, NODFOR, NODOUT, RCFORC, SECFORC, SPCFORC and SPHOUT.

The time interval between outputs shown has been used for most of the analysis in this thesis. However, to fully capture the behavior of certain wave propagation phenomena, it was necessary to increase the output frequency to 100MHz (or DT = 1.000e-05 in LS-DYNA keyword according to the dimensional set used in the simulation).

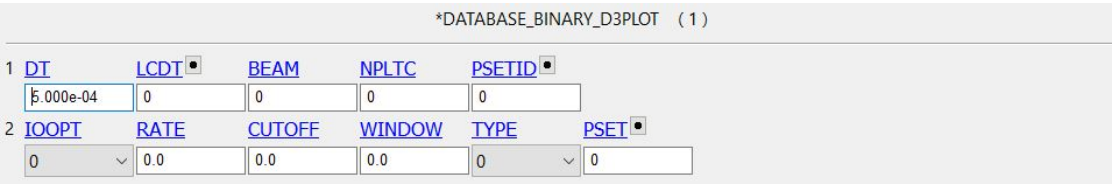

Figure A.12: LS-DYNA Pre-Post V4.8 screenshot of the keyword for the D3PLOT output setting (***DATABASE_BINARY_D3PLOT**).

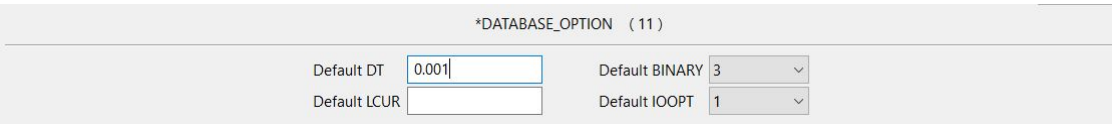

Figure A.13: LS-DYNA Pre-Post V4.8 screenshot of the keyword for the ASCII output setting (***DATABASE_ASCII_OPTION**).

Contact Setting

In Chapter 3, two contact settings between SPH and FE plate parts have been implemented: SPH/FEM tied contact, and transition zone made up of hybrid adaptive solid to SPH elements tiedly connected with the SPH plate part (internally) and with the FE plate part (externally).

The following figures show the LS-DYNA Pre-Post V4.8 screenshot related to the configuration of the keyword used to set the tied contact. In particular, keywords in Figs. A.14 and A.15 respectively connect nodes to solid elements or solid elements to solid elements.

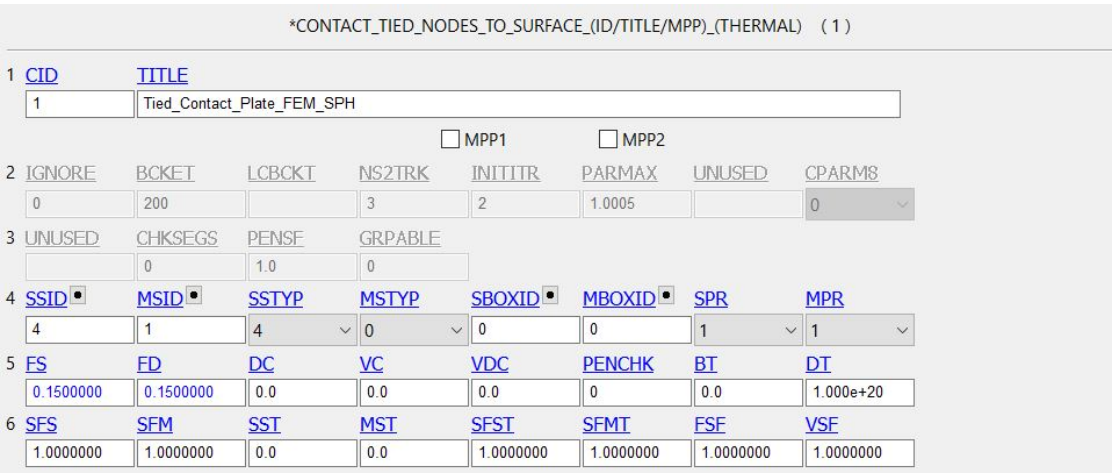

Figure A.14: LS-DYNA Pre-Post V4.8 screenshot of the keyword for the tied contact setting (***CONTACT_TIED_NODES_TO_SURFACE**).

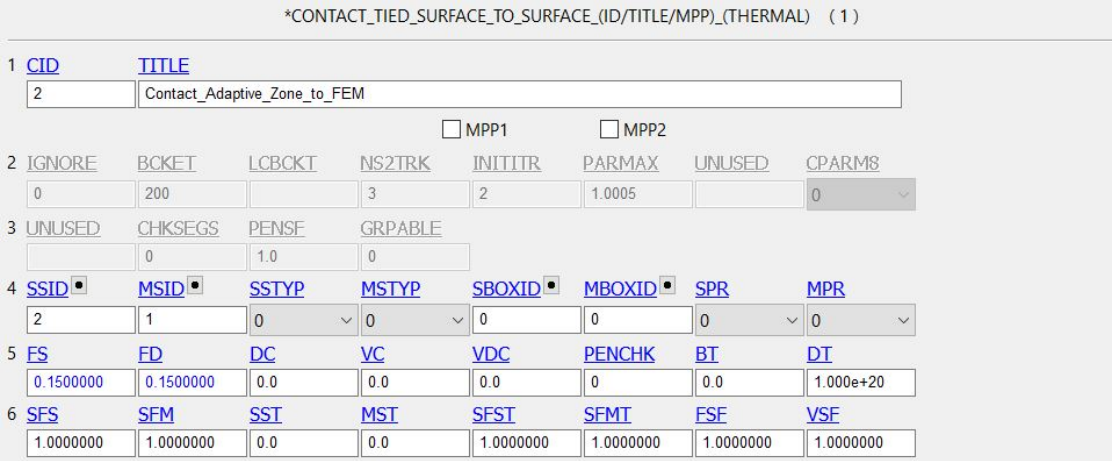

Figure A.15: LS-DYNA Pre-Post V4.8 screenshot of the keyword for the tied contact setting (***CONTACT_TIED_SURFACE_TO_SURFACE**).

Figure A.16 show the LS-DYNA Pre-Post V4.8 screenshots related to the configuration of the keyword used in the simulation discussed in Chapter 3 to define the characteristic of the hybrid adaptive solid to SPH elements. In the hybrid transition contact scenario, it is related only to the transition part.

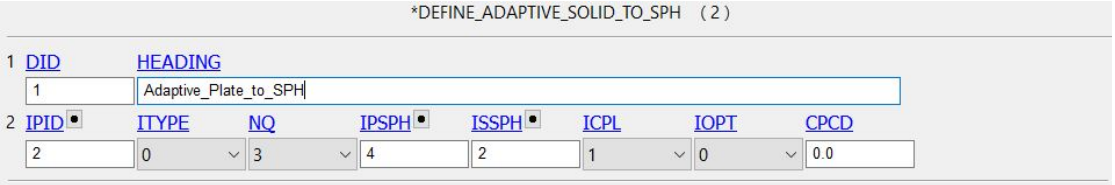

Figure A.16: LS-DYNA Pre-Post V4.8 screenshot of the keyword for the adaptive solid elements to SPH particles setting (***DEFINE_ADAPTIVE_SOLID_TO_SPH**).

B

LS-DYNA keywords: Whipple Shield HVI

In this appendix, additional supporting material relevant to the main text is provided for further reference. Below is the screenshot from LS-DYNA Pre-Post V4.8 illustrating the keyword configuration used in the simulation described in Chapter 4.

Dimensional consistency is critical for correct simulation. The simulation uses the following dimensional set: [mm, kg, ms, KN, GPa, J, Kelvin].

Boundary Conditions

In the HVI Whipple shield simulation, the external edges of the two plates are clamped in the same way as for the external edges of the single plate simulations in Chapter 3. Please refer to Fig. A.3 in the previous Appendix.

Control setting

The control settings for the Whipple Shield simulation are mostly the same as those for the single-plate simulation. Therefore, the settings displayed in Figs. A.4, A.5, A.6, and A.7 remain valid.

However, to investigate the impact of a hyper-velocity impact on both the first and second plates, the termination time was extended to 100 microseconds, as illustrated in Fig. B.1.

Figure B.1: LS-DYNA Pre-Post V4.8 screenshot of the keyword for the termination time control (***CONTROL_TERMINATION**).

Initial setting

Figure B.2 displays the LS-DYNA Pre-Post V4.8 screenshot concerning the keyword configuration used in the Whipple shield simulation to set the projectile initial velocity.

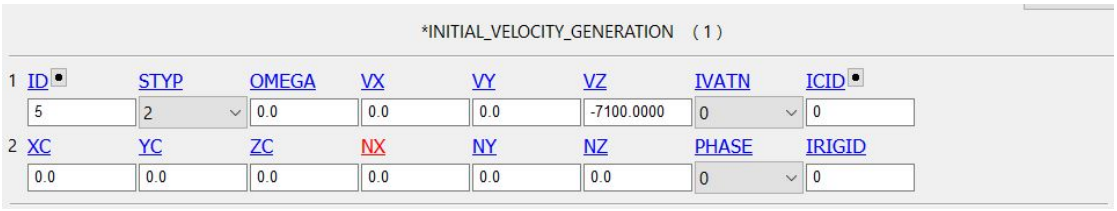

Figure B.2: LS-DYNA Pre-Post V4.8 screenshot of the keyword for the projectile initial velocity (***INITIAL_VELOCITY_GENERATION**).

Material Properties

Figures B.3 and B.4 show the LS-DYNA Pre-Post V4.8 screenshots related to the keywords used in the simulation discussed in Chapter 4 to set the material model and the equation of state.

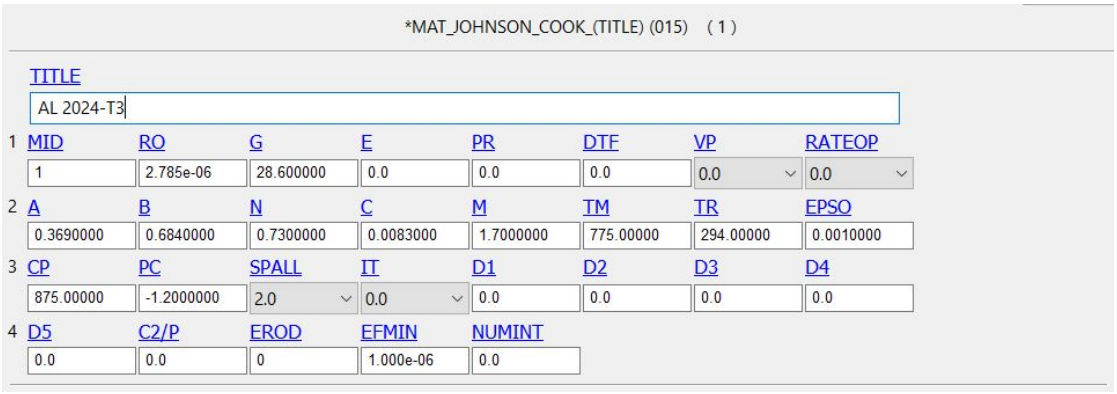

Figure B.3: LS-DYNA Pre-Post V4.8 screenshot of the keyword for the implemented material model (***MAT_JOHNSON_COOK**).

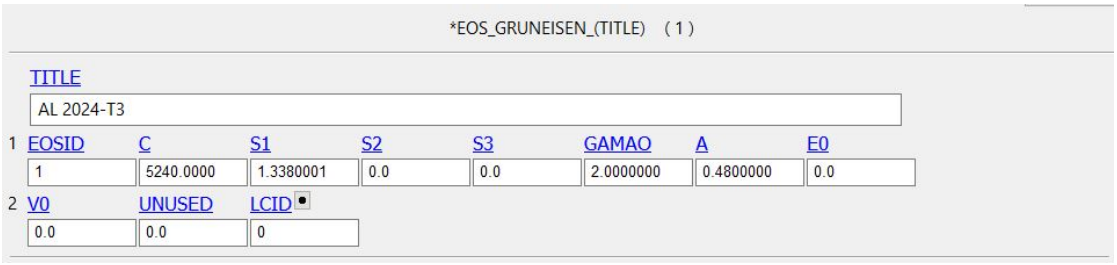

Figure B.4: LS-DYNA Pre-Post V4.8 screenshot of the keyword for the implemented material equation of state (***EOS_GRUNEISEN**).

Output Setting

The output settings remain the same as those defined in Appendix A, specifically in Figs. A.12 and A.13.

Contact Setting

A hybrid SPH-FEM zone, which links the SPH and FEM zones, is implemented in the simulation described in Chapter 4. Figure B.5 shows the settings for this zone. It is connected to the SPH domain through the ***CONTACT_TIED_NODES_TO_SURFACE** card, and to the FEM domain through the ***CONTACT_TIED_SURFACE_TO_SURFACE** card. Please refer to Figs. A.14 and A.15.

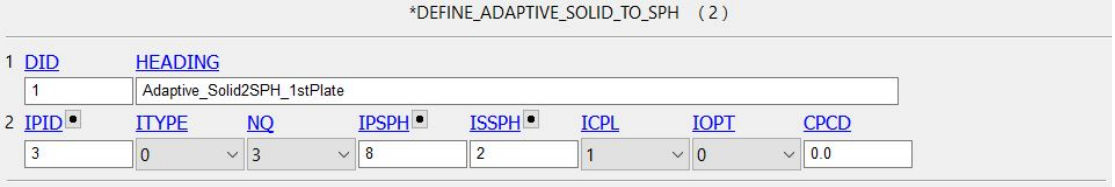

Figure B.5: LS-DYNA Pre-Post V4.8 screenshot of the keyword for the adaptive solid elements to SPH particles setting (***DEFINE_ADAPTIVE_SOLID_TO_SPH**).